10-13-2017 11:00 AM

# Modeling of Force and Motion Transmission in Tendon-Driven Surgical Robots

Farshad Anooshahpour, *The University of Western Ontario*

Supervisor: Ilia G. Polushin, *The University of Western Ontario*
Joint Supervisor: Rajni V. Patel, *The University of Western Ontario*
A thesis submitted in partial fulfillment of the requirements for the Doctor of Philosophy degree in Electrical and Computer Engineering

### Recommended Citation

# Abstract

Tendon-based transmission is a common approach for transferring motion and forces in surgical robots. In spite of design simplicity and compactness that comes with the tendon drives, there exists a number of issues associated with the tendon-based transmission. In particular, the elasticity of the tendons and the frictional interaction between the tendon and the routing result in substantially nonlinear behavior. Also, in surgical applications, the distal joints of the robot and instruments can not be sensorized in most cases due to technical limitations. Therefore, direct measurement of forces and use of feedback motion/force control for compensation of uncertainties in tendon-based motion and force transmission are not possible. However, force/motion estimation and control in tendon-based robots are important in view of the need for haptic feedback in robotic surgery and growing interest in automatizing common surgical tasks.

One possible solution to the above described problem is development of mathematical models for tendon-based force and motion transmission that can be used for estimation and control purposes. This thesis provides analysis of force and motion transmission in tendon-pulley based surgical robots and addresses various aspects of the transmission modeling problem. Due to similarities between the quasi-static hysteretic behavior of a tendon-pulley based da Vinci® instrument and that of a typical tendon-sheath mechanism, a distributed friction approach for modeling the force transmission in the instrument is developed. The approach is extended to derive a formula for the apparent stiffness of the instrument. Consequently, a method is developed that uses the formula for apparent stiffness of the instrument to determine the stiffness distribution of the tissue palpated. The force transmission hysteresis is further investigated from a phenomenological point of view. It is shown that a classic Preisach hysteresis model can accurately describe the quasi-static input-output force transmission behavior of the da Vinci® instrument.

Also, in order to describe the distributed friction effect in tendon-pulley mechanisms, the creep theory from belt mechanics is adopted for the robotic applications. As a result, a novel motion transmission model is suggested for tendon-pulley mechanisms. The developed model is of pseudo-kinematic type as it relates the output displacement to both the input displacement and the input force. The model is subsequently used for position control of the tip of the instrument. Furthermore, the proposed pseudo-kinematic model is extended to compensate for the coupled-hysteresis effect in a multi-DOF motion. A dynamic transmission model is also suggested that describes system's response to high fre-

quency inputs. Finally, the proposed motion transmission model was used for modeling of the backlash-like hysteresis in RAVEN II surgical robot.

## Co-Authorship Statement

The thesis presented here has been written by Farshad Anooshahpour under supervision of Dr. Ilia G. Polushin and Dr. Rajni V. Patel. Part of the materials in this thesis have been published in peer-reviewed journal papers and refereed conference proceedings, or are under review for publication. The research published in each paper has been conducted by the principal author, and guided and supported by the co-authors who are the research supervisors and Dr. Peyman Yademellat (in some publications) as listed below,

- *F. Anooshahpour*, P. Yadmellat, I. Polushin, R. V. Patel, "A Motion Transmission Model for a Class of Tendon-Based Mechanisms with Application to Position Tracking of the da Vinci® Instrument," IEEE Transaction of Mechatronics, (accepted subject to minor revisions).

- *F. Anooshahpour*, P. Yadmellat, I. Polushin, R. V. Patel, "A Motion Transmission Model for Multi-DOF Tendon-Driven Mechanisms with Hysteresis and Coupling: Application to a da Vinci Instrument," IEEE/RSJ International Conference on Intelligent Robots and Systems, Vancouver, BC, IEEE, 2017 (accepted).

- *F. Anooshahpour*, P. Yadmellat, I. G. Polushin, R. V. Patel, "Modeling of Tendon-Pulley Transmission Systems with Application to Surgical Robots: A Preliminary Experimental Validation," IEEE International Conference on Advanced Intelligent Mechatronics (AIM), Munich, Germany, pp. 761-766, IEEE, 2017.

- *F. Anooshahpour*, I. Polushin, R. V. Patel, "Classical Preisach Model of Hysteretic Behavior in a da Vinci Instrument," IEEE International Conference on Advanced Intelligent Mechatronics (AIM), Banff, AB, pp. 1392-1397, IEEE, 2016.

- *F. Anooshahpour*, I. Polushin, R. V. Patel, "Tissue Compliance Determination Using a da Vinci Instrument," IEEE International Conference on Robotics and Automation (ICRA), Seattle, WA, pp. 5344-5349, IEEE, 2015.

- *F. Anooshahpour*, I. Polushin, R. V. Patel, "A Quasi-Static Modelling of the da Vinci Laparoscopic Instrument," IEEE/RSJ International Conference on Intelligent Robots and Systems (IROS), Chicago, IL, pp. 1308-131, IEEE, 2014.

*Dedicated to:*
*my parents, Hamid and Pooran, for their faith in me,*
*&*
*my brothers, Farid and Mahdi for their support.*

# Acknowledgement

I would like to express my sincere appreciation and gratitude to my professors Dr. Ilia G. Polushin and Dr. Rajni V. Patel for supervising my research during my PhD studies. I would like also to thank Dr. Peyman Yadmellat for his collaboration and interest in this topic. I would also thank my lab-mates, the people of CSTAR, for sharing their knowledge and experience with me.

## Funding

# Table of Contents

# List of Tables

# List of Figures

# Nomenclature

## Chapter 1: Symbols

$\Gamma \geq 0$ denotes the wrapping angle.

$\Phi \in [0, \Gamma]$ is the slip zone within the wrapping angle.

$ds$ is the length of an infinitesimal control volume in the slip zone.

$r$ is the radius of the pulley.

$\theta \in [0, \Phi]$ is the angular location of the control volume.

$G = \frac{dm}{dt}$ denotes the mass flow rate or the mass of a substance which passes the control volume's boundary per unit of time.

$\rho$ is the density of the belt.

$A(s)$ is the cross section area of the belt at point $s$.

$V(s)$ is the speed of the belt at point $s$.

$\vec{P} \in \mathbb{R}^2$ denotes the linear momentum.

$\vec{F} \in \mathbb{R}^2$ is the net force applied to the surface of the control volume.

$m$ is mass.

$T(s) > 0$ is the belt's tension at point $s$.

$\vec{f} \in \mathbb{R}^2$ is Coulomb friction per unit length of the control volume.

$\vec{n} \in \mathbb{R}^2$ is normal force per unit length of the control volume.

$T_t > 0$ is the belt's tension in the tighter span of the belt-drive.

$T_s > 0$ is the belt's tension in the looser span of the belt-drive.

$\tau_{in}$ is the torque applied to the input pulley of a multi-pulley system.

$\tau_{out}$ is the torque applied to environment by the output pulley of a multi-pulley system.

$r_1 > 0$ is the radius of the input pulley of a two-pulley belt drive.

$r_2 > 0$ is the radius of the output pulley of a two-pulley belt drive.

$V_t$ is the speed of the belt in the tighter span of a two-pulley belt drive.

$V_s$ is the speed of the belt in the looser span of a of a two-pulley belt drive.

$q_1$ is the angular displacement of the input pulley.

$q_2$ is the angular displacement of the output pulley.

$\epsilon(s)$ is the belt's strain at point $s$.

$E$ is the belt's modulus of elasticity.

$ref$ is a subscript corresponding to the belt's reference condition.

$dl(s)$ is the length of a material segment of the belt centering at point $s$.

# Chapter 2: Symbols

$L$ is the length of the curved surface.

$R$ is the radius of the curved surface.

$x \in [0, L]$ denotes the position along the curved surface.

$T^0(x) > 0$ denotes the pretension distribution along the curved surface.

$T(x) > 0$ denotes the tension distribution along the curved surface.

$T_{in}$ is the input force applied to the free end of the tendon.

$x_w = \min\{x \in [0, L] \colon T_{in} e^{\frac{\mu}{R} x sgn(v)} = T^0(x)\}$ is the farthest point of the acitve/slip length from the point of application of $T_{in}$.

$F$ denotes Coulomb friction force applied to an infinitesimal segment of the tendon within the slip/active length.

$N$ denotes the normal force applied to the infinitesimal segment of the tendon within the slip/active length.

$d\theta$ is the bending angle of an infinitesimal element of the tendon.

$sgn(v)$ determines the direction of the impending motion of an infinitesimal element of the tendon.

$\mu$ is the coefficient of Coulomb friction.

$d\Delta$ denotes the elongation of an infinitesimal element of the tendon.

$E$ is the tendon's modulus of elasticity.

$A$ is the cross section area of the tendon.

$\Delta$ is the total elongation of the tendon as a result of applying $T_{in}$ to its free end.

$\varphi \in [0, 1]$ denotes the normalized position along the curved surface.

$K_t$ is the natural stiffness of the tendon.

$\tau_{in}$ is the torque applied to the input pulley of a multi-pulley system.

$\tau_{out}$ is the torque which the output pulley of a multi-pulley system applies to environment.

$\eta > 0$  is a dimensionless parameter which represents the effect of both the friction and the bending of the curved surface.

$\Delta q$  is the change of pulley rotational displacement $q$ after change in the direction of rotation of the input pulley.

$I$  is a constraint in dual-tendon systems that represents the pretension effect.

# Chapter 3: Symbols

$T_{in}$ is the input force applied to the free end of the tendon.

$x \in [0, L]$ denotes the position along the curved surface.

$L$ is the length of the curved surface.

$R$ is the radius of the curved surface.

$\varphi \in [0, 1]$ denotes the normalized position along the curved surface.

$T(\varphi)$ denotes the tension distribution along the curved surface.

$\Delta$ is the total elongation of the tendon as a result of applying the input force $T_{in}$ to its free end.

$\eta > 0$ is a dimensionless parameter which represents the effect of both the friction and the bending of the curved surface.

$sgn(v)$ determines the direction of the impending motion in the active length of the tendon.

$T^0(\varphi)$ is the initial tension distribution within the tendon and along the curved surface.

$\varphi_w \in [0, 1]$ is the normalized position of the farthest point of the acitve/slip length from the point of application of $T_{in}$.

$K_n$ is the natural stiffness of tendon

$E$ is tendon's modulus of elasticity.

$A$ is the cross section area of tendon.

$K_{app}$ is the apparent stiffness of the tendon.

$d\Delta$ denotes an infinitesimal change in the total length of the tendon.

$dT_{in}$ is an infinitesimal change of the input force.

$k_{app}^{min-pull}$ is the tendon's minimum apparent stiffness resulting from a pulling input force.

$k_{app}^{min-push}$ is the tendon's minimum apparent stiffness resulting from a pushing input force.

$r_1$ is the radius of the input pulley.

$r_2$ is the radius of the output pulley.

$\tau_{in}$  is the torque applied to the input pulley of a dual-tendon system.

$\tau_{out}$  is the torque which the output pulley of a dual-tendon system applies to environment.

$q$  is the rotational displacement of the pulley.

$\Delta q$  is the change of pulley rotational displacement $q$ after change in the direction of rotation of the input pulley.

$K_{app}^{Dual}$  denotes the apparent stiffness of a dual-tendon system.

$K_{env}$  is the environmental stiffness.

$q_1^{J1}$  is the rotation of the input pulley of the upper jaw in a gripping palpation.

$q_1^{J2}$  is the rotation of the input pulley of the lower jaw in a gripping palpation.

$k_{app}^{Dual-min}$  denotes the minimum apparent stiffness of a dual-tendon system.

# Chapter 4: Symbols

$\hat{\gamma}_{\alpha\beta}(\cdot)$ is the relay operator with upper threshold $\alpha$ and lower threshold $\beta$.

$u(t)$ is the input signal to the relay operators or the Preisach model.

$\mu(\alpha, \beta)$ denotes the weighting function that scales the output of the relay operator $\hat{\gamma}_{\alpha\beta}(\cdot)$.

$f(t)$ is the output signal of the Preisach model.

$\alpha_0$ is the largest of the upper thresholds $\alpha_i$ between all the relay operators $\hat{\gamma}_{\alpha_i\beta_j}(\cdot)$.

$S^+$ denotes the set of relay operators switched positive.

$S^-$ denotes the set of relay operators switched negative.

$L(t)$ is the stair-like interface link (or border polygon) which separates $S^+$ and $S^-$ on the limiting triangle.

$f_{\alpha\beta}$ denotes the first order reversal or the output of the system as a result of monotonically increasing the input from below $u(t) = \beta_0$ to $u(t) = \alpha$ then decreasing to $u(t) = \beta$.

$\hat{L}(t)$ is the matrix of vertices of the interface link $L(t)$.

$F_x$ is the output force measured with the force sensor.

# Chapter 5: Symbols

$T_1 > 0$ is the belt span tension before the slip zone.

$T_2 > 0$ is the belt span tension after the slip zone.

$\mu_s > 0$ is the coefficient of the Coulomb surface friction.

$\Gamma \in [0, \pi]$ is the wrapping angle.

$\Phi \in [0, \Gamma]$ is the angular length of the slip zone.

$F_R \in \mathbb{R}^2$ is the joint normal force.

$\dot{m} = \frac{dm}{dt}$ denotes the mass flow rate or the mass of a substance which passes the control volume's boundary per unit of time.

$V_1$ is the speed of tendon that enters the control volume.

$V_2$ is the speed of tendon that leaves the control volume.

$\tau_f$ is the Coulomb frictional torque at joint axis.

$\mu_J > 0$ is the coefficient of Coulomb friction at the joint axis.

$r'$ is the inner radius of the pulley.

$r$ is the outer radius of the pulley.

$\tau_{load}$ is the external loading torque.

$l_i$ is the length of tendon at i-th span in a multi-pulley tendon drive.

$L_s$ is the total length of the tendon in a multi-pulley tendon drive.

$T_s > 0$ is the initial preset tension along the tendon in a multi-pulley tendon drive.

$L$ is the length of the curved surface.

$R$ is the radius of the curved surface.

$x \in [0, L]$ denotes the position along the curved surface.

$T_{in}$ is the input force applied to the free end of the tendon.

$T^0(x) > 0$ denotes the pretension distribution along the curved surface.

$T(x) > 0$ denotes the tension distribution along the curved surface.

$\mu > 0$ is the coefficient of Coulomb friction at the surface.

$sgn(v)$ determines the direction of the impending motion in the active length of the tendon.

$x_w = \min\{x \in [0, L]\colon T_{in}e^{-\frac{\mu}{R}xsgn(v)} = T^0(x)\}$ is the farthest point of the acitve/slip length from the point of application of $T_{in}$.

$\eta > 0$ is a dimensionless parameter which represents the effect of both the friction and the bending of the curved surface.

$\Delta$ is the total elongation of the tendon as a result of applying $T_{in}$ to its free end.

$K_n$ is the natural stiffness of the tendon.

$q$ is the pulley's rotational displacement.

$\varphi \in [0, 1]$ denotes the normalized position along the curved surface.

$r_1$ is the radius of the input pulley.

$r_2$ is the radius of the output pulley.

$\tau_{in}$ is the torque applied to the input pulley of a dual-tendon system.

$\tau_{out}$ is the torque which the output pulley of a dual-tendon system applies to environment.

$\Delta q$ is the change of pulley rotational displacement $q$ after change in the direction of rotation of the input pulley.

$J(x(t))$ denotes a switching function.

$\alpha_1$ is a parameter of motion transmission model that represents the effect of friction and elasticity of the forward tendon-run.

$\alpha_2$ is a parameter of motion transmission model that represents the effect of friction and elasticity of the return tendon-run.

$\beta$ is a parameter of motion transmission model that represents the of geometry of the transmission.

$\Lambda$ is a constraint in dual-tendon systems that represents the pretension effect

$k_p$ denotes the proportional gain of the PID controller.

$k_d$ denotes the derivative gain of the PID controller.

$k_I$ denotes the integral gain of the PID controller.

# Chapter 6: Symbols

$L$ is the length of the curved surface.

$R$ is the radius of the curved surface.

$\mu$ is the coefficient of Coulomb friction.

$x \in [0, L]$ denotes the position along the curved surface.

$F$ is the input force applied to the free end of the tendon.

$T(x) > 0$ denotes the tension distribution along the curved surface.

$T^0(x) > 0$ denotes the pretension distribution along the curved surface.

$sgn(v)$ determines the direction of the impending motion in the active/slip length of the tendon.

$d\Delta$ denotes the elongation of an infinitesimal element of the tendon.

$E$ is the tendon's modulus of elasticity.

$A$ is the cross section area of the tendon.

$\Delta$ is the total elongation of the tendon as a result of applying $F$ to its free end.

$K_n$ is the natural stiffness of the tendon.

$\eta > 0$ is a dimensionless parameter which represents the effect of both the friction and the bending of the curved surface.

$T_{il} > 0$ is the tension in the left-end side of the i-th tendon.

$q$ is the angular position of the input pulley.

$\Delta q$ is the relative change in the angular displacement of the input pulley after change in the direction of rotation.

$\Delta\theta = \theta(t) - \theta_0$ is the relative change in the angular displacement of the output pulley after change in the direction of rotation of the input pulley.

$r_1$ is the radius of the input pulley.

$r_2$ is the radius of the output pulley.

$S(x(t))$ denotes a switching function.

$\boldsymbol{\Theta} \in \mathbb{R}^{n \times 1}$ is the vector of output angular displacements.

$\boldsymbol{B} \in \mathbb{R}^{n \times n}$ is the rigid transmission matrix.

$\boldsymbol{Q} \in \mathbb{R}^{n \times 1}$ is the vector of input-pulley/motor displacements.

$\boldsymbol{A} \in \mathbb{R}^{n \times n}$ is the matrix of hysteretic transmission.

$\boldsymbol{\tau_{in}} \in \mathbb{R}^{n \times 1}$ is the vector of input torques applied on the input pulleys of a multi-DOF system.

$\beta_{cij}$ is a an element of $\boldsymbol{B}$ that represents the rigid coupling effect of i-th DOF on j-th DOF of a multi-DOF system.

$(\alpha_{tcij}, \alpha_{bcij})$ is a pair of elements of $\boldsymbol{A}$ that represents the hysteretic coupling effect of i-th DOF on j-th DOF of a multi-DOF system.

$\theta_p$ denotes the wrist's pitch angle.

$\theta_{gr}$ denotes the wrist's right grasp angle.

$\theta_{gl}$ denotes the wrist's left grasp angle.

$q_p$ is the displacement of the input pulley of pitch DOF of the da Vinci instrument.

$q_{gr}$ is the displacement of the input pulley of the right-grasp DOF of the da Vinci instrument.

$q_{gl}$ is the displacement of the input pulley of the left-grasp DOF of the da Vinci instrument.

$l_1$ is the length of common normal between $z_1$ and $z_2$.

$l_{2l}$ is the distance of frame $\{l\}$ from the rotation axis of the left and right jaws.

$d_l$ is the offset along $z_{2l}$ from plan $xy$ of frame $\{l\}$.

${}^j R_i \in \mathbb{R}^{3 \times 3}$ is the orientation of frame $\{i\}$ relative to frame $\{j\}$.

$r_{mi}$ is the radius of the input/motor pulley of i-th DOF of the da Vinci instrument.

$r_p$ is the radius of the pulley-like groove on the pitch link of the wrist mechanism.

$r_{int}$ is the radius of the intermediate pulley of the wrist mechanism.

$r_{gr}$ is the radius of pulley-like groove on the right jaw of the wrist mechanism.

$r_{gl}$ is the radius of pulley-like groove on the left jaw of the wrist mechanism.

$N$ is the total number of the experiments.

$GOF_i$ is the goodness-of-fit associated with the i-th experiment.

$M_i$ is the total number of samples for the i-th experiment.

$\hat{\theta}_i$ is the estimated wrist angle using the proposed model for the i-th experiment.

$b$ is the coefficient of viscous friction.

$v(x)$ is the speed of tendon at point $x$.

$\gamma_t$ is a parameter representing the dynamic effect of the forward tendon-run.

$\gamma_b$ is a parameter representing the dynamic effect of the return tendon-run.

# Chapter 7: Symbols

$\tau_{in}$ is the torque applied to the input pulley of a dual-tendon system.

$\Delta$ is the total elongation of a tendon which has a frictional interaction with a curved surface.

$q$ is the angular position of a pulley.

$\Delta q$ is the relative change in the angular displacement of the input/ouput pulley after change in the direction of rotation of the input pulley.

$r_1$ is the radius of the input pulley.

$r_2$ is the radius of the output pulley.

$\varphi \in [0, 1]$ denotes the normalized position along the curved surface.

$\varphi_w \in [0, 1]$ is the normalized position of the farthest point of the acitve/slip length of the tendon from the point of application of the input force.

$S(x(t))$ is a switching function.

$\alpha_t$ is a parameter of motion transmission model that represents the effect of friction and elasticity of the forward tendon-run.

$\alpha_b$ is a parameter of motion transmission model that represents the effect of friction and elasticity of the return tendon-run.

$\beta$ is a parameter of motion transmission model represents the effect of geometry of the pulleys.

$\Lambda$ is a constraint in dual-tendon systems that represents the pretension effect.

$\gamma_t$ is a parameter of motion transmission model that is related to the pretension effect of the forward tendon-run.

$\gamma_b$ is a parameter of motion transmission model that is related to the pretension effect of the return tendon-run.

$RMSE$ denotes the root mean square error.

$GOF$ denotes the goodness of fit.

# Chapter 1

# Introduction

## 1.1 Motivation

**T**endon driven surgical robots are currently the state of the art technology of modern robotic surgery. Designed for Minimally Invasive Surgery (MIS), these robots require few keyhole incisions on the patient's body that allow for insertion of surgical instruments and an endoscope through a trocar in order to execute surgical tasks. MIS procedures result in faster recovery, lesser pain and trauma, shorter hospital stays, and considerably lesser expenses in comparison with traditional surgery. As a result, there exists a growing demand for this new technology which is driven by both patients' and healthcare system's satisfaction.

Minimally invasive robotic surgical systems, however, also present some substantial challenges, which need to be addressed in the future generations of these robots. One limitation of the current tendon-driven surgical robots is that they do not provide haptic feedback. In particular, placement of force sensors at the tip of an MIS instrument is difficult with the current sensor technology. As a result, when interacting with the tissue, surgeons are deprived of the sense of touch which normally plays an important role in many surgical tasks. On the other hand, as the modern operating rooms are evolving towards implementation of autonomous robotic technologies, there is a growing interest in autonomous supervised execution of some routine surgical tasks. In particular, tasks such as tissue palpation and

suturing can be executed by a robot under supervision of a surgeon. Joints of a typical surgical robot, however, are frequently difficult to sensorize due to technical limitations such as size restrictions and sterilization requirements. As a result, feedback control algorithms cannot be implemented directly.

One potential solution to the issues described above lies in the development of precise mathematical models of tendon-driven mechanisms. Such a model can be used for estimation of the interaction forces as well as for implementation of high precision position tracking control algorithms. Development of precise models for tendon-driven surgical robots and instruments, however, is a difficult task. In fact, they exhibit substantially nonlinear behavior, typically in the form of a static hysteresis, which in some cases is accompanied by tendon coupling effects. Modelling such a complex behavior represents a significant challenge for researchers working in the area of tendon-based robotics.

This thesis aims at providing fundamental analysis and mathematical models for force and motion transmission in *tendon-pulley* based mechanisms, which is currently a common method of power transmission in surgical robotic systems. The proposed models and control algorithms are implemented and tested on various da Vinci® instruments as well as the RAVEN II® surgical robot.

In the remaining part of this chapter, a brief historical overview of the emergence of Robot Assisted Minimally Invasive Surgery (RAMIS) is presented, which is followed by a literature review on the existing mathematical models for tendon-driven transmission in industrial and robotic applications. At the end of this chapter, the structure of the Thesis is discussed, and a brief description of the content of each subsequent chapter is presented.

## 1.2 Background

In the conventional open surgery, most of the pain, discomfort, and post-surgery morbidities are side effects of the process of opening way to the area of surgery rather than the surgical procedure itself [4]. To address this issue, the Minimally Invasive Surgery (MIS) (also called laparoscopic surgery) was developed over the last two decades of the twentieth century. MIS is a result of integration of medical imaging technologies and advanced instrumentation. It allowed for the first time in history of medicine to perform surgery inside

Figure 1.1: A minimally invasive lobectomy-brachythrapy surgery at London Health Sciences Center (LHSC) in 2009 [1].

a patient's body through just a few tiny ports [5]. Compared to the open surgery, the limited invasion of MIS results in less skin and soft tissue trauma, fewer infections and hernias, less post operative pain, faster recovery and, consequently, shorter hospital stays [6].

In spite of the advantages described above, conventional MIS also suffers from a number of restrictions. For example, fixed entry ports effectively remove two translational degrees of freedom from each instrument, thus severely decreasing dexterity. Restriction of the instrument's motion at the entry port also results in an undesirable fulcrum effect which, in particular, makes hand-eye coordination difficult. In addition, an MIS surgeon is required to maintain a non-ergonomic uncomfortable upright posture, and has to look at the monitor in a direction away from the surgical site. The 2D picture on the monitor deprives the surgeon of depth cues [7]. Last but not least, since the surgeons' hands are no longer in direct contact with the organs and tissues, important haptic cues are no longer available. There is only a limited and deteriorated sense of touch through instruments' handles [8].

Robot Assisted Minimally Invasive Surgery (RAMIS), also known as robot assisted laparoscopic surgery, is a sophisticated answer to the challenges of manual MIS. Due to their inherent versatility, robots can potentially overcome most of the shortcomings of the MIS mentioned above. The advantages of RAMIS can be appreciated by reviewing different aspects of the da Vinci® Surgical system (Intuitive Surgical Inc.). At present time, da Vinci®
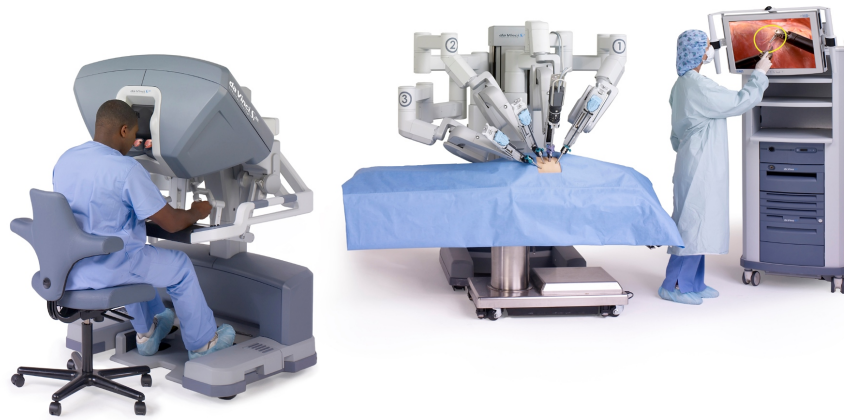
Figure 1.2: The da Vinci® surgical system by Intuitive Surgical (©Intuitive Surgical Inc. [2])

is the most well-known RAMIS system in existence[1]. This is a tendon-driven (specifically, tendon-pulley based) robot which has a structure of a teleoperator, as shown in Figure 1.2. The surgeon controls the master robot by holding the two control handles and looking at a magnified 3D high-definition display while also maintaining a proper body posture and hand-eye coordination. The slave robot, on the other hand, consists of up to four serial manipulators each holding either an MIS instrument or a surgical endoscope. The motion of the surgeon's hands is captured and filtered by the master robot, and subsequently scaled and translated into the motion of the slave robot. Each da Vinci tool (otherwise known as the da Vinci EndoWrist® instrument) is a set of up to four tendon-pulley mechanisms tightly packed into a casing with a narrow shaft. The tip has 4-DOF (degrees-of-freedom) motion capability similar to the one of the human hand [10], [11].

Many issues typical for the manual MIS are solved in the da Vinci surgical system. In particular, the fulcrum effect is compensated by an appropriately designed computer algorithm. The missing degrees of freedom are restored by a new design of the instruments which provides 4 DOF of the tip in addition to the 3 positioning DOFs of the manipulator (Figure 1.3). The stereoscopic display at the master side provides 3D view of the surgical field using two independent cameras located at the tip of the surgical endoscope. The hand-eye coordination is restored by a proper ergonomic design of the master console (see

---

[1]Four generations of the da Vinci Surgical System have been introduced so far. In 2015 alone, the total number of procedures performed worldwide by the da Vinci Surgical system was around 650,000 operations, of which 20% correspond to urology surgery, 48% to gynecology surgery, and 28% to general surgery [9].

Figure 1.3: The EndoWrist® instrument as the end-effector of da Vinci surgical system ( ©Intuitive Surgical Inc.) [2].
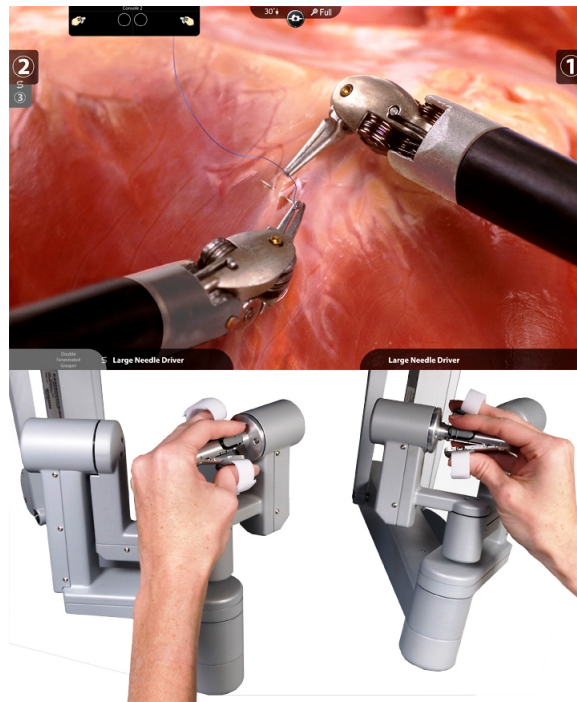


Figure 1.4: The hands' position and the view of the operation field available to the surgeon while working with the da Vinci® surgical system (©Intuitive Surgical Inc.) [2].
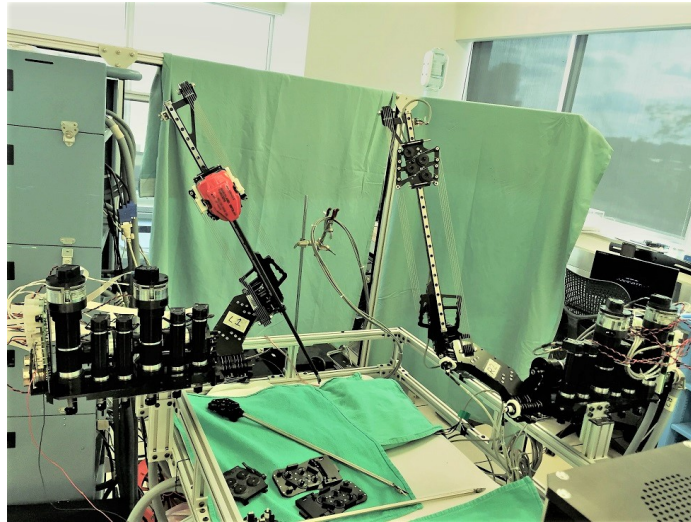
Figure 1.5: The RAVEN II surgical robotic system installed in CSTAR, London, ON, Canada

Figure 1.4). The advantages of RAMIS over conventional manual MIS is validated in several studies such as [12], [13] and [14]. A similar RAMIS system which is mostly used in academic and research environments is the RAVEN II surgical robot [15]. RAVEN II, shown in Figure 1.5, is also a tendon-pulley based robot which is designed as an open platform in order to boost research on surgical robotics and to provide a testbed for preoperative and intra-operative data integration. Similarly to the da Vinci surgical robot, RAVEN II has seven DOFs, which include three DOFs for positioning of the remote center of motion and insertion and the four remaining DOFs for driving the surgical instrument. Although RAVEN II is originally designed as a standalone robot, it however can be combined with a haptic device to form a surgical teleoperator system.

In spite of all the advantages of the present day RAMIS systems, these robots do not provide haptic feedback. The mechanically separated master and slave robots result in the laparoscopic tools be removed away from the surgeon's hand, depriving the surgeons of the sense of touch when interacting with the surgical task. The benefits of haptic feedback in MIS, however, have been documented in many studies [16–18]. Lack of haptic feedback may lead to poor force regulation resulting in application of excessive forces to healthy tissues and/or insufficient forces while grasping and suturing. Also, without force feedback, surgeons are not able to make use of the haptic cues which can be obtained in manual operations and partly in MIS by palpating the tissue [6].

To address this problem, some researchers attempted to design laparoscopic instruments with embedded force sensors. In [19], a pressure/tactile sensor was placed at the tip of an experimental RAMIS instrument and the measured data was presented as a visual feedback to the user. In [20], a sensorized prob was used as a robot's end-effector in a master-slave teleoperator system. The pressure sensed by the probe was integrated with the forces measured at the manipulator joints in order to improve estimation of the tool-tissue interaction forces. Other researchers modified the commercial RAMIS instruments and equipped them with some sensory devices. In [21], a piezoresistive sensor array on a da Vinci instrument as well as a balloon-based tactile display on the master console of the da Vinci system were implemented to form a closed-loop haptic force feedback system. At Canadian Surgical Technologies and Advanced Robotics (CSTAR), a da Vinci instrument was sensorized using strain gauges attached to the tendons [22]; the forces at the tip were then estimated assuming proportionality between the forces at the tip and the measured tendon strains. In [23], this sensorized instrument was used in a master-slave telerobotic system, enabling the operator to receive visual or haptic force feedback while performing surgery. In majority of the existing sensor-based solutions, however, only one DOF (typically the grasping) is equipped with force sensors. Among a few exceptions is a 6-DOF force-torque sensor in the form of a Stewart platform mechanism developed by the German Aerospace Center (DLR) [24]. The sensor is mounted close to the tip of the instrument and allows for measurement of forces and moments in all DOFs.

Despite all the advancements in sensorized instruments, none of these technologies has made its way into the market. In general, there is a number of obstacles for successful sensorizing of surgical devices like a da Vinci instrument. Most of the existing force sensors are too large to be mounted directly at the tip of the instrument, and they typically do not tolerate the harsh chemical environment of the sterilization processes. Also, due to safety considerations, the laparoscopic instruments are usually allowed for a limited number of uses, typically around ten [25]. Force sensors, on the other hand, are expensive; as a result, it is simply not economically feasible to use them in applications where they need to be discarded after a few operations.

An alternative solution, which is pursued in this thesis, is based on estimation of the interaction forces using an accurate mathematical model of a RAMIS instrument. The estimation algorithm in this case would use the measurement of real-time data such as the input torque

and displacement of the motors for estimating the output force and/or motion at the tip of the instrument. For instruments with rigid linkage, such as those used in manual laparoscopic surgery, force estimation can be done relatively easily as the kinematic model of such mechanisms are fairly accurate (for example, see [26]). However, for surgical robots, implementation of flexible tendon-based transmissions may have substantial advantages over rigid alternatives [27]. In the case of robots with tendon-based transmission mechanisms, the problem of force estimation becomes much more challenging. In particular, compliance of the tendons and the frictions between the tendons and their routings (*e.g.*, sheath or guiding pulleys) result in substantially nonlinear behavior.

Aside from force estimation, a sufficiently precise model of a laparoscopic instrument can be used for the design of control algorithms that guarantee accurate trajectory tracking. Even though currently existing surgical robotic systems have human-in-the-loop structure, it appears that, in the future, substantial number of typical surgical tasks will be performed using supervised automation. In [28], researchers from the University of California, Berkeley introduced a vision based method for supervised automation of multi-throw suturing in a da Vinci surgical system. The same group also investigated automated tumor resection [29], debridement and pattern cutting [30], and palpation for locating subcutaneous blood [31]. Automated suturing was also addressed in [32] and [33]. In [34] and [35], two distinct semi-autonomous palpation techniques were developed that use Mitsubishi PA10 robot and a da Vinci instrument, respectively.

There is also a number of studies performed in the University of Washington's BioRobotics lab (*e.g.* [36]) mainly on motion control of RAVEN II. These works will be discussed later in this chapter in greater detail, as RAVEN II has been one of the testbeds for the models proposed in this thesis. This thesis is focused on development of force and motion transmission models in tendon-pulley based robots and instruments.

## 1.3 Problem Statement

The present day surgical instruments and robots employ tendon-pulley transmission mechanisms to remotely actuate their distal joints. Tendons' compliance and their frictional interactions with the pulleys and/or with the routings result in a highly nonlinear trans-

mission behavior which, in particular, includes input-output hysteresis. The major goal of the research presented in this thesis is to develop a closed-form model(s) for tendon-pulley transmission which can be successfully used in real-time force estimation and motion control algorithms.

A number of requirements can be formulated for such a model. First, since the joints and the tip of a typical tendon-driven surgical robot are not sensorized, the model's estimation must only be based on the available actuator data that is motor's current and position. Second, the model must allow for relatively fast computations so it can be implemented in real-time algorithms. Third, the model of interest must be able to explain all hysteretic behaviors in force and motion transmission, including the hysteresis due to the coupling between degrees-of-freedom.

Ideally, such a model should also provide an insight into the system's behavior so it can be helpful for the design of future robots. Finally, even though the motions that execute typical surgical task are very slow, the model of interest should also describe adequately the system's response to high-frequency components in the input signal.

The research presented in this thesis addresses the aforementioned research questions. Specifically, models for tendon-pulley transmission with the above described properties are developed, and their applications to surgical robotics are implemented and tested. The models developed in this thesis can potentially be applied to a wide range of robots and mechanisms with tendon-pulley transmissions for the purpose of accurate motion control and force estimation.

## 1.4 Literature Review

The idea of using belts (ropes, cables, tapes, or tendons) with pulleys to transmit power to remote mechanisms has a long history. The high power-to-weight ratio and the simple structure of the belt-pulley systems made it possible to transmit large amounts of power to several end-users in early industries. Belt-pulleys, otherwise called belt drives, had been widely in use until 1930's, when they were largely replaced by electric power transmission. However, due to their unique properties, belt-drives are still in use in a number of applications, such as in refrigerators, washing machines, and vehicle engines.

Osborne Reynolds, a prominent British-Irish engineer and mathematician, was the first to notice that in a steadily working belt-drive which consists of two identical pulleys the speed of rotation of the driving and the driven pulleys is not the same. Also, the speed of the belt in the tighter span is faster than that of the slacker span[2]. Thus, Reynolds concluded that the belt must slip somewhere on the surface of pulleys, which in particular results in unavoidable power loss [37]. The work of Reynolds, however, did not receive the attention it deserved as the efficiency of the transmission apparatus was not a major concern in those days [38]. In later years, the mechanics of belt drives was gradually developed to the point where it explained Reynolds' observations and provided more detailed analysis of belt-pulley power transmission systems. Figure 1.6 illustrates a typical schematic overview of a belt-drive system. A common approach for analysis of belt-drive mechanical systems
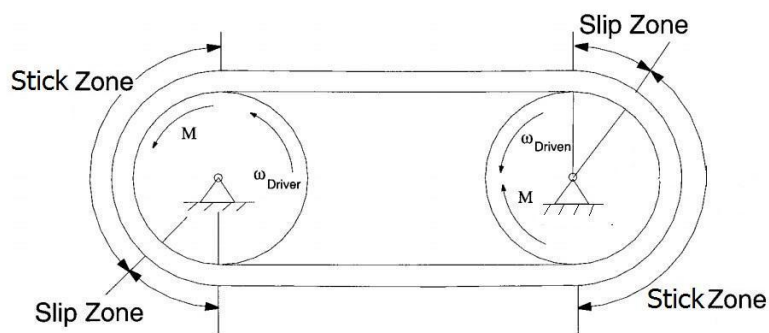


Figure 1.6: A representation of the slip and stick zones on the input/driving and output/driven pulleys in a typical belt derive. Adopted from [3].

is based on the classical creep theory [39]. According to the creep theory, two distinct zones are formed on the contact arcs of the pulleys in a belt-drive system in a steady state condition: the stick zone and the slip zone. In the stick zone, no interaction exists between the pulley and the belt, thus no moment is transferred. As a result, a constant tension is maintained in this zone. In the slip zone, the Coulomb friction starts to develop which stretch (or compress) the belt [40].

One of the goals of the belt-drive mechanics is to identify and estimate factors which shorten the life-span of the belt in a steadily power transmitting application. Some of these factors include belt fatigue due to cyclic tension change, belt wearing due to sliding

---

[2]The velocity of the belt in the tighter span is equal to the velocity of the surface of the driving pulley. Similarly, velocity of the belt in the slacker span is equal to that of the driven pulley.

on the pulleys, and belt's transverse vibrations. The belt-drive mechanics also addresses the design aspects such as the efficiency of transmission and the maximum transmissible momentum [3, 41]. For mechanical applications, numerical solutions are frequently employed to calculate for the aforementioned factors. The belt-drive mechanics is discussed in the next section, as it lays a foundation for understanding the notions and terminology used in this thesis. A review of the belt-drive mechanics which utilizes the classical creep theory can be found in [42].

In robotic applications, tendon-based transmission has been characterized either in the form of tendon-sheath or tendon-pulley architectures. Compactness, design flexibility, low stiffness, and light weight are some key features of the tendon drives that make them popular in robotics. The application of this type of power transmission can be found mostly in robotic hands and fingers, as well as in surgical robots. Examples of tendon-sheath transmission in robotics include robotic hands [43], continuum robots [44], flexible NOTES robots [45] and RAMIS robots [46]; examples of tendon-pulley transmission are robotic hands [47, 48] and surgical robots such as da Vinci® and Raven II as mentioned before.

A tendon which is guided by a sheath (or canals, or tubes) provides more flexibility for designers to easily route it over and around the links and obstacles in order to deliver power to distal joints. Tendon-pulley, on the contrary, requires idler pulley(s) to change direction which itself necessitates more design effort. On the other hand, a tendon in a sheath typically experiences larger frictions due to the long contact arc so exhibit a harder nonlinearity as compared to tendon-pulley [49, 50].

The dominant nonlinearity in tendon-sheath transmission is known as *backlash-like hysteresis* [49], which is a backlash with curves merging smoothly to the ascending and descending branches of the hysteresis. This is different from the pure backlash as seen for example in gear drives. In a series of studies performed during 1990's, Kaneko and co-authors presented a detailed static analysis of tendons sliding through a sheath in a single and a dual-tendon arrangements. In [51] and [52], mathematical description of the distributed friction and the elongation of the tendons for a single tendon-sheath transmission was given. Different from some previous studies, compliance of the tendons was taken into account in these works. A numerical model was also developed which was based on infinitesimal mass, spring, and friction elements. In [49], the authors studied behavior

of a one-DOF finger actuated by a dual tendon-sheath mechanism. They provided a phenomenological model of the backlash-like behavior, and showed experimentally that the backlash-like behavior and stability of the closed loop control system are highly affected by the magnitude of the input. This is known as direction dependency feature of the tendon drives. The work [49] was followed in [53], where a partial differential equation model was derived for dual tendon-sheath transmissions. A numerical simulation model was also presented with a similar assumption of infinitesimal lumped parameters. In general, work [53] gives a detailed insight into the phases of transmission in a dual tendon-sheath mechanism.

Aside from numerical solutions, a few closed-form models have also been suggested in the literature for single and dual tendon-sheath transmissions. Most of these are phenomenological models. In [54], a piecewise linear model that describes the backlash-like behavior of a dual tendon-sheath mechanism is proposed, and a controller is subsequently designed based on the smooth inverse model of the backlash. In [55], a modified Bouc-Wen model and a Coleman-Hodgdon model were proposed for a single and a dual tendon-sheath mechanisms. In [56], a formula for estimating the width of the backlash in a pretension-free catheter is suggested, which relates geometrical features of the sheath and tendon, such as radius of curvature, bending angle, and the gap between sheath and tendon, to the width of hysteresis. A three-mass model that describes a single tendon-sheath transmission is suggested in [50].

On the other hand, nonlinear behavior of tendon-pulley mechanisms have received relatively scarce attention in the literature. Tendon-pulley drives can be categorized into three different configurations, namely $N$, $2N$ and $N + 1$, each representing the number of actuators used in an $N$-DOF robot of that family. These configurations are compared in [57]. Tendon-pulley transmission of surgical robots belongs to class $N$, that is each joint is empowered by a single motor using two opposing tendons, whereas in $2N$ and $N + 1$ type mechanisms, each tendon is actuated separately. In [58], the sensitivity of the design parameter of the $2N$ type transmission is discussed. In [59], the kinematic and control issue of an $N + 1$ robotic finger is presented, and the effect of location of the force/displacement sensor on the controller design and system stability is discussed. Prisco and co-authors [60] derived a dynamic model for a class $N$ robot manipulator based on the Lagrangian approach. The transmission configuration studied in [60] is similar to that of surgical robots; specifically, for each degree of freedom of the robot there is a number of idle pulleys (see
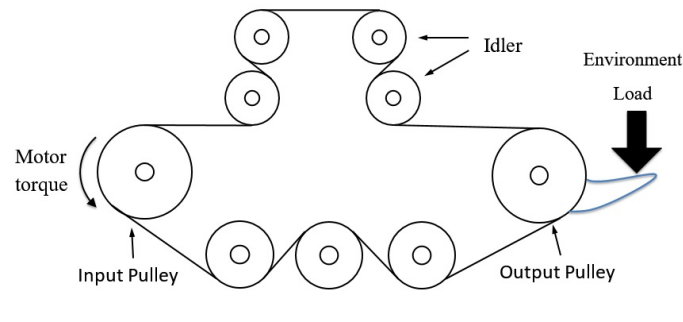
Figure 1.7: A typical tendon-pulley transmission in surgical robots consists of serval idlers.

Figure 1.7). In [60], each tendon is replaced with parallel spring and damper, positions of all pulleys are assumed to be known/measured, and zero friction is assumed between tendon and pulleys. However, friction at pulleys' axes is addressed. The common point of the above mentioned studies and many similar works in robotics is that they assume tendon tensions [58, 59, 61] and/or joint positions [60] known (measured). In reality, majority of the tendon-pulley based surgical robots are not fully sensorized; in other words, displacements of the joints and idle pulleys are typically unknown and tensions cannot be measured, while only motors' current and position are available. A review of the literature on surgical robots (*e.g.* in [23]) reveals that often tendon-pulley drives were treated as systems with rigid linkage, and a simple linear proportionality formula was conventionally used to model the transmission, while compliance of the tendons and the tendon-pulley frictions were not considered.

In a recent set of studies conducted by a group of researchers at the University of Washington, an approach similar to [60] was developed to model the dynamics of tendon-pulley transmission in a surgical application. Specifically, in [62], a one DOF dummy finger which was actuated through a network of idlers was analyzed. In this work, the idlers were ignored and tendons were replaced with parallel interconnections of two exponential springs and two linear dampers, while the frictions were considered point contact resistive forces at the pulleys' axes. The approach was adopted for position control of the RAVEN II surgical robot in [36], where an Unscented Kalman Filter (UKF) was used to estimate the system parameters when off-line and the states of the model when online. In [63], a stereo vision data was fed into the UKF to improve the accuracy of the motion control algorithm. In [64], the above described model was used to estimate the gripping force of the tendon-pulley

driven RAVEN II instrument. The suggested UKF algorithm uses the motor current and the motor encoder readings for estimation. The proposed method, however, shows inaccuracies for stiff transmissions [36], and does not explain the static input-output hysteretic behavior. In [65], the frictional effect of a network of idler pulleys on a single tendon was investigated. A formula was empirically derived which relates the network's resistance to the average wrap angles, average tension within the tendon, and the number of idlers.

There is also another set of studies in robotics which attributes the nonlinear behavior of the tendon-pulley mechanism to tendon and pulley frictional interaction similar to the creep theory for belt-drives. In [66], in order to estimate the transmission stiffness of a capstan-drive, two slip zones and one stick zone were assumed on the surface of the driven pulley. Similar approach was used in a number of studies such as [67] which is focused on the motion transmission error due to tendon slip in a capstan-drive.

In this thesis, new mathematical models based on distributed friction are proposed for use in surgical instrument and robots. In order to introduce the notions and terminology used throughout the rest of this thesis, the elastic creep theory from belt-drive mechanics is briefly outlined in the next section.

## 1.5 Belt-Drive Mechanics

At present time, it appears that the classical studies of belt-drive mechanics have made little effect on the research on tendon-based robotic systems. In this thesis, in particular, simple closed-form models of tendon-pulley transmission are developed which are based on the notions and concepts of the belt drives mechanics and the creep theory. These models are subsequently applied to different problems in surgical robotic systems. The material presented in this section forms a background for the developments presented in the rest of the thesis. In this sections, all vectors are marked with an arrow sign, $\rightarrow$. No arrow means the symbol represents either the corresponding magnitude of the vector or a scalar quantity.

As mentioned earlier, the main challenge associated with the belt-drive mechanics is to properly describe the belt-pulley frictional interaction [68]. Below, the classical creep theory which is the conventional approach for studying belt-drive systems is outlined.
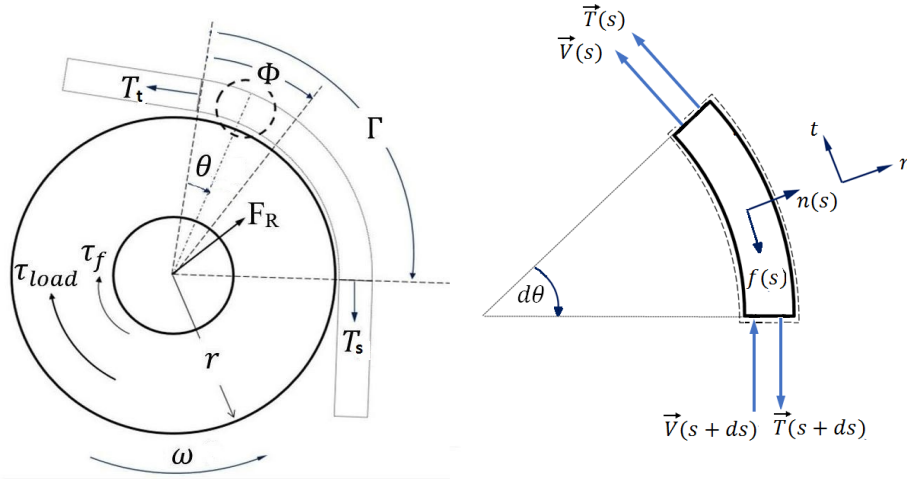
Figure 1.8: Free-body diagram of a driven pulley of a belt-drive (left). The control volume over the slip zone (right)

The creep theory assumes that the interaction between the pulley and the belt is characterized by Coulomb friction which results in forming up one slip zone and one stick zone on the contact arc of each pulley (Figure 1.6).

Consider an infinitesimal Eulerian control volume[3] in the slip zone $\Phi < \Gamma$ of a driven pulley shown in Figure 1.8 (left), where $\Gamma$ is the wrapping angle. The control volume has the length of $ds = rd\theta$ and is located at a fixed point $s$, $\theta \in [0, \Phi]$ is the angular location of $ds$, and $r > 0$ is the radius of the pulley. The steady state operation requires the mass flow of belt that enters and leaves the control volume be equal (which represents the conservation of mass). The mass flow rate $G$ is then defined

$$G := \rho A(s)V(s) = \rho A(s+ds)V(s+ds) = \text{const},$$

where the belt's density, its cross-section area, and its linear velocity are denoted by $\rho$, $A(s)$ and $V(s)$, respectively.

Additionally, for a single body of mass, Newton's second law is

$$\frac{d}{dt}\vec{P} = \vec{F} \tag{1.1}$$

---

[3]An Eulerian control volume is fixed in space, as opposed to Lagrangian control volume which moves with the material elements along the stream.

where $\vec{P} = m\vec{V}$ is the linear momentum and $\vec{F}$ is the external force applied to the mass. This formula for the fixed Eulerian control volume is written as

$$\frac{d\vec{P}}{dt} + \dot{\vec{P}}_{out} - \dot{\vec{P}}_{in} = \vec{F}, \tag{1.2}$$

where $\dot{\vec{P}}_{in}$ is the flow of belt's momentum into the control volume, $\dot{\vec{P}}_{out}$ is the flow of belt's momentum out of the control volume, and $dP/dt$ is defined as the rate of change of momentum inside the control volume due to fluctuations of flow properties, respectively[4], and $\vec{F}$ is the net force applied to the surface of the control volume. In the case of steady state rotation of the belt derive, the variables in (1.2) are given as follows:

$$\begin{aligned} \dot{\vec{P}}_{in} &= G\vec{V}(s + ds), \\ \dot{\vec{P}}_{out} &= G\vec{V}(s), \\ \tfrac{dP}{dt} &= 0, \\ \vec{F} &= \vec{T}(s) + \vec{T}(s + ds) + \vec{f} + \vec{n}, \end{aligned} \tag{1.3}$$

where $T(s)$ and $T(s + ds)$ are belt's tensions at the two ends of the segment, as shown in Figure 1.8 (right), and $\vec{f}$ and $\vec{n}$ are Coulomb friction and normal force per unit length, respectively. Gravity forces here are neglected in the net force applied to the control volume.

Force in (1.2) can be decomposed into the tangential and the normal force as follows [70],

$$T(s+ds)\left(\cos\frac{d\theta}{2}\right) - T(s)\left(\cos\frac{d\theta}{2}\right) + f(s)ds = G\left(V(s+ds)\left(\cos\frac{d\theta}{2}\right) - V(s)\left(\cos\frac{d\theta}{2}\right)\right),$$

$$-T(s+ds)\left(\sin\frac{d\theta}{2}\right) - T(s)\left(\sin\frac{d\theta}{2}\right) + n(s)ds = G\left(-V(s+ds)\left(\sin\frac{d\theta}{2}\right) - V(s)\left(\sin\frac{d\theta}{2}\right)\right).$$

For small $d\theta$, the above two equations can be simplified as follows:

$$dT + f(s)ds = GdV, \tag{1.4}$$

and

$$n(s) = \frac{T(s) - GV(s)}{r}. \tag{1.5}$$

---

[4]For basic definitions and concepts the reader is referred to [69].

Equation (1.4) relates change in belt's tension $dT$ with the contact friction $f(s)$ and the term $GdV$ which is called creep acceleration. Equations (1.5) relates the normal force $n(s)$ to the tension $T(s)$ and the centrifugal force $GV(s)$ which acts normal to the pulley surface [70]. In the classic creep theory analysis, the terms $GdV$ and $GV(s)$ are typically ignored [40] as the mass flow rate of the belt can often be neglected, thus resulting in the following new two equations:

$$dT + f(s)ds = 0, \tag{1.6}$$

$$n(s) = \frac{T(s)}{r}. \tag{1.7}$$

Equations (1.6) and (1.7) are valid as long as the belt has a negligible mass per unit length, *i.e.* $\rho \approx 0$, or moves with a very low operational velocity, *i.e.*, $V(s) \approx 0$. Using the equation for dry Coulomb friction $f(s) = \mu n(s)$, where $\mu > 0$ is the Coulomb friction coefficient, from (1.6) one can derive the following formula for the tension change in the slip zone,

$$dT + \mu T(s)d\theta = 0. \tag{1.8}$$

By integrating (1.8) over the slip zone, the formula for tension distribution in the slip zone is achieved as follows

$$T(\theta) = T_t\, e^{-\mu\theta}, \tag{1.9}$$

where $T_t = T(\theta = 0)$ is the cable tension at the point where it leaves the pulley surface. At the end of the slip zone ($\theta = \Phi$) the tension is

$$T_s = T_t\, e^{-\mu\Phi}. \tag{1.10}$$

In the whole stick zone, by definition, there is no interaction between the belt and the pulley, thus the tension $T_s$ remains constant.

In a two-pulley system, such as the one shown in Figure 1.9, the tension in the free span does not change. Thus, from (1.10) one obtains the following formulas for tension change in the driving and driven pulleys

$$\frac{T_t}{T_s} = e^{\Phi_1} = e^{\Phi_2}, \tag{1.11}$$

where $\Phi_1$ and $\Phi_2$ are the slip arcs on the driving and driven pulleys, respectively. Equation
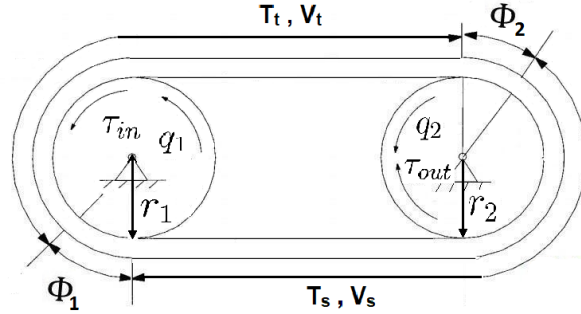
Figure 1.9: The driving and the driven pulleys in a belt-drive system. Adopted from [3].

(1.11) also confirms that the tension change over pulley surface is independent of the radius of the pulley. Moreover, from the conservation of angular momentum within a control volume assumed around the pulley, force equilibrium equations for the driving and driven pulleys can be written:

$$
\tau_{in} = (T_t - T_s)r_1,
$$
$$
\tau_{out} = (T_t - T_s)r_2.
$$
(1.12)

where $\tau_{in}$ is the torque applied to the input, $\tau_{out}$ is the load torque, $r_1$ is the radius of the input pulley, and $r_2$ is the radius of output pulley. From (1.12), a formula for force transmission in the belt-pulley system of Figure 1.6 can be derived:

$$
\tau_{out} = \frac{r_2}{r_1}\tau_{in}.
$$
(1.13)

A motion transmission formula can also be obtained. In the classical creep theory, it is assumed that the belt sticks to the surface of pulley as soon as it arrives [40]. Thus, the velocity of the belt at the tighter side $V_t$ is equal to the surface velocity of the driving pulley, and the velocity of the belt at the looser side $V_s$ equals to the velocity of the surface of the driven pulley,

$$
V_t = r_1\dot{q}_1,
$$
$$
V_s = r_2\dot{q}_2,
$$
(1.14)

where $q_1$ is the angular displacement of the input pulley and $q_2$ is the angular displacement of the output pulley, respectively. Besides, one can write the following strain-stress constitutive relation for the belt,

$$
\epsilon(s) = \frac{1}{EA}(T(s) - T_{ref}(s)),
$$
(1.15)

where the strain $\epsilon$ at a point $s$ along the tendon is described as ([70])

$$\epsilon(s) = \frac{dl(s)}{dl_{ref}(s)} - 1, \tag{1.16}$$

and $E$ is the modulus of elasticity. The subscript $ref$ corresponds to an arbitrary reference condition. If tendon in the slack condition is referenced, then $T_{ref}(s) = 0$ and $dl_{ref}(s)$ is the length of the material segment $dl(s)$ when not stretched or compressed. It is more common, however, in the literature to reference a pretensioned condition, *i.e.* $T_{ref}(s) = T_p$ and its corresponding elongation $dl_p$. Equation (1.16) can be turned into a formula for the velocity of tendon:

$$V(s) = (1 + \epsilon(s))V_{ref}, \tag{1.17}$$

where $V(s) = \frac{dl}{dt}$ and $V_{ref} = \frac{dl_{ref}}{dt}$. Substituting (1.15) in (1.17) results in the following formula

$$V(s) = \left(1 + \frac{T(s) - T_{ref}}{EA}\right)V_{ref}. \tag{1.18}$$

Combining (1.14) and (1.18) gives us the following speed ratio [38]:

$$\frac{dq_2}{dq_1}\frac{r_2}{r_1} = \frac{1 + \frac{T_s - T_{ref}}{EA}}{1 + \frac{T_t - T_{ref}}{EA}}. \tag{1.19}$$

Assuming small strains, *i.e.*, $\epsilon << 1$, we have

$$\frac{dq_2}{dq_1}\frac{r_2}{r_1} = 1 + \frac{T_s - T_t}{EA}. \tag{1.20}$$

Substituting (1.12) into (1.20), the motion transmission formula is achieved as follows:

$$\frac{dq_2}{dq_1} = \frac{r_1}{r_2}\left(1 + \frac{-\tau_{in}}{EAr_1}\right). \tag{1.21}$$

Equation (1.21) is the formula for motion transmission which is derived based on the classical creep theory. If the tendon is inelastic, *i.e.* $E \rightarrow \infty$, formula (1.21) becomes the following static relation:

$$\frac{dq_2}{dq_1} = \frac{r_1}{r_2}, \tag{1.22}$$

which is the motion transmission formula for rigid transmission. It is worth noting that the

creep theory's force transmission formula (1.13) is the same static proportionality formula of rigid transmissions, whereas motion transmission equation (1.21) is a function of both input torque $\tau_{in}$ and input displacement $q_1$.

## 1.5.1 The Compatibility Condition

One important notion which must be introduced here is the *compatibility condition* which is a physical constraint imposed on closed-loop belt/tendon systems. The compatibility condition states that the sum of all elongations and compressions along the tendon must be equal to zero,

$$\oint (dl - dl_{ref}) = 0, \tag{1.23}$$

where $\oint$ represents an integral over the tendon loop. Using (1.16) and (1.15), equation (1.23) can be rewritten in the following form,

$$\oint \epsilon \, dl_{ref} = \frac{1}{EA} \oint (T - T_{ref}) \, dl_{ref} = 0. \tag{1.24}$$

Equation (1.24) represents an important property of tendon and belt drives (including tendon-sheath transmission). Various forms of compatibility condition (1.24) are used throughout this thesis.

## 1.5.2 Conclusions on Belt-Drive Mechanics

The classical creep theory is not the only method to describe the belt-drive mechanics. More complex models that consider various additional belt properties, belt-pulley architectures, and friction models have been suggested in the past two decades. Betchel an co-authors [70] updated the classical creep theory by simultaneously considering the two centrifugal and creep-acceleration terms, as discussed earlier in this Chapter. Rubin [71] used the same analysis to develop an exact solution for a multiple-pulley arrangement. Kong *et al.* [41] incorporated belt's bending stiffness into modelling. Some researchers worked on alternative friction models. In [3], a formulation for belt-drive mechanics is suggested which employs a creep-rate-dependent friction. To account for pre-slipping friction, the

shear theory (also called the microslip theory) is developed [68]. A comparison between the shear theory and the creep theory for multipulley belt drives is given in [39]. Another interesting study is the work of Townsend *et al.* [38] which formulates the efficiency limit of the belt drives based on the principles of thermodynamics.

The literature of belt mechanics offers a wide range of numerical solutions to compute belt tensions, the slipping arcs, and the speed of rotation of the pulley(s) in multiple pulley systems. These solutions, however, are usually not applicable for control and/or estimation algorithms for tendon-drives in robotic applications as real-time computations in this case can be very challenging. Moreover, belt mechanics, which mostly targets industrial applications, ignores joint frictions and the effect of idlers, as the power loss due to these factors is not significant compared to the power transmitted between the main input and output(s). In robotic problems, however, precision usually matters. In particular, joint axis friction and idlers might affect the performance of the robot. The effect of joint frictions on tension distribution and the transmitted moment, in particular, is discussed in Chapter 5 of this thesis.

## 1.6 Contribution and Overview of the Thesis

The main goals of this thesis are: i) to provide extensive analysis of force and motion transmission in tendon-pulley mechanisms; and ii) to develop novel models for force and motion estimation for surgical robots. The approach taken in this thesis is to consider distributed frictions along the tendon in order to explain the nonlinear behavior of the force/motion transmission. The thesis can roughly be divided into two parts.

Chapters 2, 3, and 4 form the first part which deals with the issue of *force transmission* in tendon-pulley based surgical instruments. Different models are introduced, and notions such as distributed friction, the compatibility condition, and apparent stiffness of transmission are presented. A pure phenomenological model of the input-output behavior of a da Vinci® instrument is also presented in this part.

The second part, consisting of Chapters 5, 6 and 7, provides analysis and models for *motion transmission* in tendon-pulley surgical robots. A pseudo-kinematic model which relates the

output displacement to the input displacement and the input torque is presented, which effectively reproduces the static backlash-like hysteresis effect. Also, the model is extended to describe the coupling effects in a multi-DOF tendon-pulley instrument. Motion transmission in Raven II surgical robot is also investigated in this part.

### 1.6.1 Chapter 2

Chapter 2 presents some initial observations related to the force transmission in a da Vinci® instrument. The preliminary experimental measurements show a close similarity between the behavior of a tendon-pulley instrument (in our case, the da Vinci instrument) and that of a typical tendon-sheath mechanism. Therefore, based on the tendon-sheath analysis of [51] and [52], two closed-form models are suggested for the da Vinci instrument in a quasi-static condition. The two models are named the *pull model* and the *pull-push* model, respectively. Both models use only the motor torque and the rotation to estimate the forces at the tip of the instrument when it is locked in a force sensor. In particular, the compatibility condition is used in this chapter to derive the pull-push model.

### 1.6.2 Chapter 3

The goal of Chapter 3 is to examine how the models developed in Chapter 2 can be used for restoration of a fundamental functionality of the surgeons which is the ability to palpate. The method developed in this chapter allows to determine a regional map of stiffness of a tissue sample without using any force sensor and by just accounting for the available inputs, *i.e.*, the motor torque and the motor displacement. To this end, the quasi-static analysis of Chapter 2 is extended to derive a formula that describes the apparent stiffness of the instrument, from which the information about environmental stiffness can be extracted. The method is experimentally validated.

### 1.6.3 Chapter 4

In contrast with the two previous chapters, in Chapter 4 a purely phenomenological approach is taken to model force transmission behavior of the da Vinci® instrument. Specif-

ically, the applicability of the classic Preisach hysteresis approach for modelling tendon-pulley mechanism is investigated. The experimental observations reveal that the two key features of the Preisach hysteresis, which are the congruency and the wipeout properties, can be detected in the input-output behavior of the da Vinci® instrument when its tip is locked. The experimental results demonstrate that the developed approach allows for sufficiently precise prediction of the forces at the tip of the instrument.

### 1.6.4 Chapter 5

From this chapter, the motion transmission behavior of tendon-pulley mechanisms is investigated. A model for a one DOF motion of the tip of the da Vinci® instrument is derived based on the creep theory and tendon-slip analysis developed in Chapter 2 and 3. The developed model is of a pseudo-kinematic type; specifically, it relates the output displacement to both the input displacement and the input force. The model is also investigated as a part of a position control scheme, where the estimated position of the tip is used for computation of the position error. It is demonstrated that the proposed model-based controller can effectively eliminate the hysteretic behavior of the transmission and provide high accuracy positioning for various desired trajectories.

### 1.6.5 Chapter 6

In tendon-driven robots, the tendons that transmit motion/force to the distal links are routed along the proximal links. As a result, the motion of the latter affects that of the former. This is called the coupling effect. In this chapter, the novel motion transmission model which was developed in the previous chapter is extended to cover the coupling effect. While conventionally the coupling within a tendon-drive is represented with a single coupling matrix, the proposed formula in this chapter has one additional matrix which accounts for the coupling effect due to tendon elongation. The validity of the proposed coupling formula is experimentally investigated. Also in this chapter, as a further extension, a preliminary dynamic model to deal with high-frequency inputs is suggested and experimentally evaluated.

### 1.6.6 Chapter 7

In this chapter, based on the distributed friction approach which developed in the previous chapters, the motion of the first three joints of the RAVEN II surgical robot is analyzed. Our novel motion transmission model is applied to one of the joints of RAVEN II to demonstrate the effectiveness of the approach. Also the effect of pretension on system behavior is investigated for the first time. It is proven mathematically and shown experimentally that increasing pretension in a tendon-pulley transmission reduces the width of backlash in transmission. A complete derivation of the motion transmission formula in the presence of considerable pretension is given in the Appendix.

### 1.6.7 Chapter 8

Chapter 8 concludes the thesis and presents some ideas for future work.

# References

[1] "Canadian first in the treatment of lung cancer a demonstration of interdisciplinary cooperation," http://www.lhsc.on.ca/About_Us/LHSC/Media_Room/Media_Releases/ 2009/July_09.htm, 2009, [Online; accessed 07-Mar-2015].

[2] "Intuitive Surgical: Image gallery," http://www.intuitivesurgical.com/company/ media/images/, 2014.

[3] M. J. Leamy, and T. M. Wasfy, "Analysis of belt-driven mechanics using a creep-rate-dependent friction law," *Journal of Applied Mechanics*, vol. 69, no. 6, pp. 763–771, 2002.

[4] M. J. Mack, "Minimally invasive and robotic surgery," *The Journal of the American Medical Association*, vol. 285, no. 5, pp. 568–572, 2001.

[5] P. Dario, B. Hannaford, and A. Menciassi, "Smart surgical tools and augmenting devices," *IEEE Transactions on Robotics and Automation (ICRA)*, vol. 19, no. 5, pp. 782–792, 2003.

[6] A. L. Trejos, R. V. Patel, and M. D. Naish, "Force sensing and its application in minimally invasive surgery and therapy: a survey," *Institution of Mechanical Engineers, Part C: Journal of Mechanical Engineering Science*, vol. 224, pp. 1435 –1454, 2010.

[7] J. P. Ruurda, T. V. Vroonhoven, and I. Broeders, "Robot-assisted surgical systems: a new era in laparoscopic surgery," *Annals of the Royal College of Surgeons of England*, vol. 84, no. 4, pp. 223–226, 2002.

[8] P. Culmer, J. Barrie, R. Hewsonand, M. Levesley, M. Mon-Williams, D. Jayne, and A. Neville, "Reviewing the technological challenges associated with the development of a laparoscopic palpation device," *The International Journal of Medical Robotics and Computer Assisted Surgery*, vol. 8, no. 2, pp. 146–159, 2012.

[9] "Intuitive Surgical: Annual report 2015," http://investor.intuitivesurgical.com/, 2015.

[10] G. S. Guthart and J. K. Salisbury, "The Intuitive™ telesurgery system: overview and application," in *IEEE International Conference on Robotics and Automation 2000*, IEEE, pp. 618–621, 2000.

[11] M. J. Tierney, T. Cooper, C. Julian, S. J. Blumenkranz, G. S. Guthart, and R. G. Younge, "Mechanical actuator interface system for robotic surgical tools," cited July 2008. [Online]. Available: U.S.Patent6,491,701

[12] G. Hubens, H. Coveliers, L. Balliu, M. Ruppert, and W. Vaneerdeweg, "A performance study comparing manual and robotically assisted laparoscopic surgery using the da Vinci system," *Surgical Endoscopy And Other Interventional Techniques*, vol. 17, no. 10, pp. 1595–1599, 2003.

[13] L. J. Moore, M. R. Wilson, E. Waine, R. S. Masters, J. S. McGrath, and S. J. Vine, "Robotic technology results in faster and more robust surgical skill acquisition than traditional laparoscopy," *Journal of robotic surgery*, Springer, vol. 9, no. 1, pp. 67–73, 2015.

[14] H. G. Kenngott and L. Fischer and F. Nickel and J. Rom, and J. Rassweiler and B. P. Müller-Stich, "Status of robotic assistance - a less traumatic and more accurate minimally invasive surgery?," *Langenbeck's archives of surgery*, Springer, vol. 397, no. 3, pp. 333-341, 2012.

[15] B. Hannaford, J. Rosen, D. W. Friedman, H. King, P. Roan, L. Cheng, D. Glozman, J. Ma, S. N. Kosari, and L. White, "Raven-II: an open platform for surgical robotics research," *IEEE Transactions on Biomedical Engineering*, vol. 60, no. 4, pp. 954–959, 2013.

[16] B. T. Bethea, A. M. Okamura, M. Kitagawa, T. P. Fitton, S. M. Cattaneo, V. L. Gott, W. A. Baumgartner, and D. D. Yuh, "Application of haptic feedback to robotic surgery," *Journal of Laparoendoscopic & Advanced Surgical Techniques*, vol. 14, no. 3, pp. 191–195, 2004.

[17] C. R. Wagner, N. Stylopoulos, and R. D. Howe, "The role of force feedback in surgery: analysis of blunt dissection," in *International Symposium on Haptic Interfaces for Virtual Environment and Teleoperator Systems*, pp. 68–74, 2002.

[18] M. Tavakoli, R. V. Patel, and M. Moallem, "Robotic suturing forces in the presence of haptic feedback and sensory substitution," in *IEEE Conference on Control Applications*.   IEEE, pp. 1–6, 2005.

[19] A. L. Trejos, J. Jayender, M. P. Perri, M. D. Naish, R. V. Patel, and R. A. Malthaner, "Robot-assisted tactile sensing for minimally invasive tumor localization," *The International Journal of Robotics Research*, vol. 28, pp. 1118–1133, sep 2009.

[20] A. Talasaz and R. V. Patel, "Integration of force reflection with tactile sensing for minimally invasive robotic-assisted tumor localization," *IEEE Transaction on Haptics*, vol. 6, no. 2, pp. 217–227, 2013.

[21] C. H. King, M. O. Culjat, M. L. Franco, J. W. Bisley, G. P. Carman, E. P. Dutson, and W. S. Grundfest, "A multielement tactile feedback system for robot-assisted minimally invasive surgery," *IEEE Transactions on Haptics*, vol. 1, no. 2, pp. 52–56, 2009.

[22] S. Perreault, A. Talasaz, A. L. Trejos, C. D. Ward, R. V. Patel, and B. Kiaii, "A 7-DOF haptics-enabled teleoperated robotic system: Kinematic modeling and experimental verification," in *3rd IEEE RAS & EMBS International Conference on Biomedical Robotics and Biomechatronics*. Tokyo, Japan: IEEE, pp. 906–911, 2010.

[23] A. Talasaz, A. L. Trejos, S. Perreault, H. Bassan, and R. V. Patel, "A dual-arm 7-degrees-of-freedom haptics-enabled teleoperation test bed for minimally invasive surgery," *ASME Journal of Medical Devices*, vol. 8, no. 4, pp. 041 004–041 004–15, 2014.

[24] U. Seibold, B. Kubler, and G. Hirzinger, "Prototype of instrument for minimally invasive surgery with 6-axis force sensing capability," in *IEEE International Conference on Robotics and Automation (ICRA)*, pp. 496–501, 2005.

[25] *EndoWrist: Instrument and Accessory Catalog*, Intuitive Surgical, Inc., Jul. 2011.

[26] J. Rosen, B. Hannaford, M. P. MacFarlane, and M. N. Sinanan, "Force controlled and teleoperated endoscopic grasper for minimally invasive surgery experimental performance evaluation," *IEEE Transaction On Biomedical Engineering*, vol. 46, no. 10, pp. 1212–1221, 1999.

[27] D. B. Camarillo, T. M. Krummel, and J. K. Salisbury, "Robotic technology in surgery: past, present, and future," *The American Journal of Surgery*, vol. 188, no. 4, pp. 2–15, 2004.

[28] S. Sen, A. Garg, D. Gealy, S. McKinley, Y. Jen, and K. Goldberg, "Automating multi-throw multilateral surgical suturing with a mechanical needle guide and sequential convex optimization," in *IEEE International Conference on Robotics and Automation (ICRA)*, pp. 4178-4185, 2016.

[29] S. McKinley, A. Garg, S. Sen, D. V. Gealy, J. P. McKinley, Y. Jen, and K. Goldberg, "An interchangeable surgical instrument system with application to supervised automation of multilateral tumor resection," in *IEEE International Conference on Automation Science and Engineering (CASE)*, pp. 821-826, 2016.

[30] A. Murali, S. Sen, B. Kehoe, A. Garg, S. McFarland, S. Patil, W. D. Boyd, S. Lim, P. Abbeel, and K. Goldberg, "Learning by observation for surgical subtasks: Multilateral cutting of 3D viscoelastic and 2D orthotropic tissue phantoms," in *IEEE International Conference on Robotics and Automation (ICRA)*, pp. 1202–1209, 2015.

[31] S. McKinley, A. Garg, S. Sen, R. Kapadia, A. Murali, K. Nichols, S. Lim, S. Patil, P. Abbeel, A. M. Okamura *et al.*, "A single-use haptic palpation probe for locating subcutaneous blood vessels in robot-assisted minimally invasive surgery," in *IEEE International Conference on Automation Science and Engineering (CASE)*, pp. 1151–1158, 2015.

[32] R. C. Jackson and M. C. Çavuşoğlu, "Needle path planning for autonomous robotic surgical suturing," in *IEEE International Conference on Robotics and Automation (ICRA)*, pp. 1669–1675, 2013.

[33] C. Staub, T. Osa, A. Knoll, and R. Bauernschmitt, "Automation of tissue piercing using circular needles and vision guidance for computer aided laparoscopic surgery," in *IEEE International Conference on Robotics and Automation (ICRA)*, pp. 4585–4590, 2010.

[34] A. Talasaz and R. V. Patel, "Remote palpation to localize tumors in robot-assisted minimally invasive approach," in *IEEE International Conference on Robotics and Automation (ICRA)*, pp. 3719–3724, 2012.

[35] F. Anooshahpour, I. G. Polushin, and R. V. Patel, "Tissue compliance determination using da Vinci instrument," in *IEEE International Conference on Robotics and Automation (ICRA)*, pp. 5344–5349, 2015.

[36] M. Haghighipanah, Y. Li, M. Miyasaka, and B. Hannaford, "Improving position precision of a servo-controlled elastic cable driven surgical robot using unscented Kalman filter," in *International Conference on Intelligent Robots and Systems (IROS)*, pp. 2030–2036, 2015.

[37] O. Reynolds, "On the efficiency of belts or straps as communicators of work," *Journal of the Franklin Institute*, vol. 99, no. 2, pp. 142–145, 1875.

[38] W. T. Townsend and J. K. Salisbury, "The efficiency limit of belt and cable drives," *Journal of mechanisms, transmissions, and automation in design*, vol. 110, no. 3, pp. 303–307, 1988.

[39] D. G. Alciatore and A. E. Traver, "Multipulley belt drive mechanics: creep theory vs shear theory," *Journal of Mechanical Design*, vol. 117, no. 4, pp. 506–511, 1995.

[40] K. L. Johnson, *Contact Mechanics*. Cambridge University Press, 1987.

[41] L. Kong and R. G. Parker, "Steady mechanics of belt-pulley systems," *Journal of applied mechanics*, vol. 72, no. 1, pp. 25–34, 2005.

[42] J. N. Fawcett, "Chain and belt drives, a review," *Shock and Vibration Information Center The Shock and Vibration Digest*, vol. 13, no. 5, 1981.

[43] G. Borghesan, G. Palli, and C. Melchiorri, "Design of tendon-driven robotic fingers: Modeling and control issues," in *IEEE International Conference on Robotics and Automation (ICRA)*, pp. 793–798, 2010.

[44] T. Kato, I. Okumura, S. E. Song, A. J. Golby, and N. Hata, "Tendon-driven continuum robot for endoscopic surgery: Preclinical development and validation of a tension propagation model," *IEEE/ASME Transactions on Mechatronics*, vol. 20, no. 5, pp. 2252–2263, 2015.

[45] D. J. Abbott, C. Becke, R. I. Rothstein, and W. J. Peine, "Design of an endoluminal NOTES robotic system," in *IEEE/RSJ International Conference on Intelligent Robots and Systems (IROS)*, pp. 410–416, 2007.

[46] R. J. Franzino, "The laprotek surgical system and the next generation of robotics," *Surgical Clinics of North America*, vol. 83, no. 6, pp. 1317–1320, 2003.

[47] A. Nahvi, J. M. Hollerbach, Y. Xu, and I. W. Hunter, "An investigation of the transmission system of a tendon driven robot hand," in *IEEE/RSJ/GI International Conference on Intelligent Robots and Systems (IROS)*, vol. 1, pp. 202–208, 1994.

[48] M. Grebenstein, M. Chalon, W. Friedl, S. Haddadin, T. Wimböck, G. Hirzinger, and R. Siegwart, "The hand of the DLR hand arm system: Designed for interaction," *The International Journal of Robotics Research*, vol. 31, no. 13, pp. 1531–1555, 2012.

[49] M. Kaneko, W. Paetsch, and H. Tolle, "Input-dependent stability of joint torque control of tendon-driven robot hands," *IEEE Transactions on Industrial Electronics*, vol. 39, no. 2, pp. 96–104, 1992.

[50] G. Palli, G. Borghesan, and C. Melchiorri, "Modeling, identification, and control of tendon-based actuation systems," *IEEE Transactions on Robotics*, vol. 28, no. 2, pp. 277–290, 2012.

[51] M. Kaneko, T. Yamashita, and K. Tanie, "Basic considerations on transmission characteristics for tendon drive robots," in *IEEE Fifth International Conference on Advanced Robotics (ICAR),'Robots in Unstructured Environments'*, pp. 827–832, 1991.

[52] M. Kaneko, M. Wada, H. Maekawa, and K. Tanie, "A new consideration on tendon-tension control system of robot hands," in *IEEE International Conference on Robotics and Automation (ICRA)*, 1991, pp. 1028–1033.

[53] V. Agrawal, W. J. Peine, and B. Yao, "Modeling of transmission characteristics across a cable-conduit system," *IEEE Transactions on Robotics*, vol. 26, no. 5, pp. 914–924, 2010.

[54] V. Agrawal, W. J. Peine, B. Yao, and S. Choi, "Control of cable actuated devices using smooth backlash inverse," in *IEEE International Conference on Robotics and Automation (ICRA)*, pp. 1074–1079, 2010.

[55] T. N. Do, T. Tjahjowidodo, M. S. Lau, and S. J. Phee, "Nonlinear friction modelling and compensation control of hysteresis phenomena for a pair of tendon-sheath actuated surgical robots," *Mechanical Systems and Signal Processing*, vol. 60, pp. 770–784, 2015.

[56] S. B. Kesner and R. D. Howe, "Position control of motion compensation cardiac catheters," *IEEE Transactions on Robotics*, vol. 27, no. 6, pp. 1045–1055, 2011.

[57] S. C. Jacobsen, H. Ko, E. K. Iversen, and C. C. Davis, "Antagonistic control of a tendon driven manipulator," in *IEEE International Conference on Robotics and Automation*, pp. 1334–1339, 1989.

[58] V. Hayward and J. M. Cruz-Hernández, "Parameter sensitivity analysis for design and control of tendon transmissions," in *Experimental Robotics IV*,   Springer, 1997, pp. 239–252.

[59] J. K. Salisbury and J. J. Craig, "Articulated hands: Force control and kinematic issues," *The International journal of Robotics research*, vol. 1, no. 1, pp. 4–17, 1982.

[60] G. Prisco and M. Bergamasco, "Dynamic modelling of a class of tendon driven manipulators," in *International Conference on Advanced Robotics (ICAR)*, pp. 893–899, 1997.

[61] H. Kobayashi, K. Hyodo, and D. Ogane, "On tendon-driven robotic mechanisms with redundant tendons," *The International Journal of Robotics Research*, vol. 17, no. 5, pp. 561–571, 1998.

[62] E. Naerum, H. H. King, and B. Hannaford, "Robustness of the Unscented Kalman filter for state and parameter estimation in an elastic transmission," in *Proceedings of Robotics: Science and Systems*, Seattle, USA,2009.

[63] M. Haghighipanah, M. Miyasaka, Y. Li, and B. Hannaford, "Unscented Kalman filter and 3D vision to improve cable driven surgical robot joint angle estimation," in *IEEE International Conference on Robotics and Automation (ICRA)*, pp. 4135–4142, 2016.

[64] Y. Li, M. Miyasaka, M. Haghighipanah, and L. C. B. Hannaford, "Dynamic modeling of cable driven elongated surgical instruments for sensorless grip force estimation," in *2016 IEEE International Conference on Robotics and Automation (ICRA)*, pp. 4128–4134, 2016.

[65] M. Miyasaka, J. Matheson, A. Lewis, and B. Hannaford, "Measurement of the cable-pulley Coulomb and viscous friction for a cable-driven surgical robotic system," in *IEEE/RSJ International Conference on Intelligent Robots and Systems (IROS)*, pp. 804–810, 2015.

[66] J. Werkmeister and A. Slocum, "Theoretical and experimental determination of capstan drive stiffness," *Precision Engineering*, vol. 31, no. 1, pp. 55–67, 2007.

[67] O. Baser and E. I. Konukseven, "Theoretical and experimental determination of capstan drive slip error," *Mechanism and Machine Theory*, vol. 45, no. 6, pp. 815–827, 2010.

[68] L. Kongand and R. G. Parker, "Microslip friction in flat belt drives," *Proceedings of the Institution of Mechanical Engineers, Part C: Journal of Mechanical Engineering Science*, vol. 219, no. 10, pp. 1097–1106, 2005.

[69] J. D. Anderson, *Fundamentals of aerodynamics*. MacGraw-Hill, New York, 1991.

[70] S. E. Bechtel, S. Vohra, K. I. Jacob, and C. D. Carlson, "The stretching and slipping of belts and fibers on pulleys," *Journal of Applied Mechanics*, vol. 67, no. 1, pp. 197–206, 2000.

[71] M. B. Rubin, "An exact solution for steady motion of an extensible belt in multipulley belt drive systems," *Journal of Mechanical Design*, vol. 122, no. 3, pp. 311–316, 2000.

# Chapter 2

# Quasi-Static Modeling of Force Transmission in the da Vinci® Instrument

**T**wo simplified quasi-static models for the da Vinci instrument are proposed which take into account distributed frictions and compliance of the tendons. These models are derived from static analysis of the interaction of the tendons with a curved surface. The curved-surface analogy is suggested based on the similarity between the force transmission behavior of the tendon-pulley based da Vinci instrument and that of a typical dual tendon-sheath mechanism. The key parameters of the models are identified, and the performance of the models is experimentally evaluated. Experimental results obtained suggest that a weighted combination of the outputs of the two models provides a sufficiently close estimate of the output torque of the da Vinci instrument.

## 2.1 Introduction

The lack of haptic feedback is one of the major limitations of today's surgical teleoperator systems [1]. Without a proper haptic feedback mechanism, surgeons are deprived of the
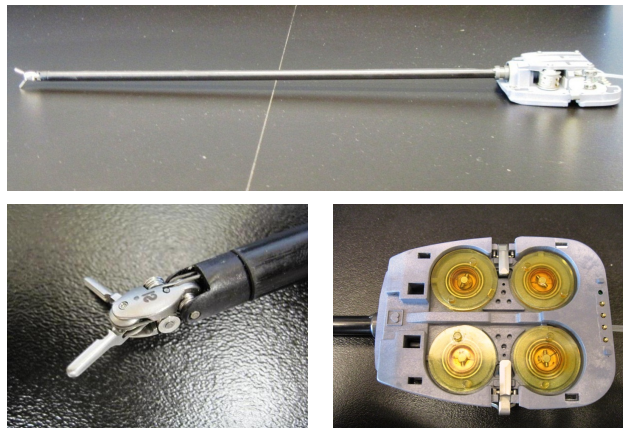
Figure 2.1: The da Vinci instrument (EndoWrist® grasper) [3].

feeling of interaction with the tissue, which may lead to poor force regulation resulting in application of excessive forces to healthy tissues and/or insufficient forces while grasping and suturing. Also, without force feedback, surgeons are not able to make use of the haptic cues which can be obtained in manual operations and partly in the traditional Minimally Invasive Surgery (MIS) by palpating tissue [2]. There exist several obstacles for implementation of haptic feedback in surgical teleoperator systems, one of which is related to difficulties in measuring the interaction forces between the tool and tissue. Most of the existing force sensors are too large to be mounted directly at the tip of the instrument, and they also typically do not tolerate the harsh chemical environment of the sterilization processes. Also, due to safety considerations, the MIS instruments allow for a limited number of uses, typically around ten [3]. Force sensors, on the other hand, are expensive; as a result, it is not economically feasible to use them in applications where they need to be discarded after a few operations.

An alternative solution consists of development and implementation of an online algorithm for estimation of the interaction forces at the tip of the instrument. Such an algorithm would require precise knowledge of the mathematical model of the corresponding tool. The major difficulty related to this approach is that the underlying mathematical models of the laparoscopic instruments are complex and highly nonlinear, which makes the processes of modelling and parameter identification difficult. For the da Vinci instruments (such as the EndoWrist® grasper shown in Figure 2.1) which use tendon-pulley force transmission, the nonlinearities come from the tendons' compliance as well as frictions between

the tendons and the pulleys. Tendon-based actuation systems have been used widely in robotic applications because of their high power-to-weight ratio and simplicity of the design. Tendon-based power transmission can be either in the form of tendon-sheath mechanisms or tendon-pulley systems; examples of the former are the University of Bologna robotic hand [4] and the flexible NOTES robotic system [5], while examples of the latter are the UTAH/MIT hand [6] and the DLR robotic hands [7]. The corresponding literature, however, is substantially richer for the case of tendon-sheath transmission in comparison with the tendon-pulley transmission case. In the 1990's, detailed static analysis for the case of tendon-sheath transmission was performed by Kaneko and coauthors [8, 9]; in particular, a numerical model was developed which was based on the infinitesimal mass, spring, and friction elements. In [10], a partial differential equation model that describes the dynamic behavior of a dual tendon-sheath system was proposed. A few closed-form models have also been suggested in the literature, including a model of the backlash-like behavior of a dual tendon-sheath system [11], and a three-mass model that describes a single tendon-sheath transmission [12]. In the case of a tendon-pulley transmission, the modeling is even more challenging as there is no general agreement on the source(s) of nonlinearity.

In this work, the quasi-static behavior of the da Vinci instrument is modelled using tendon-sheath analysis. Our preliminary analysis demonstrates that the input-output behavior of the da Vinci Instrument is closely similar to that of a dual tendon-sheath system. The sheath-like effect can be accounted for by considering the effect of tendon slippage on the surface of several idler pulleys on each forward and return tendon runs. Therefore, in this study, the tendon-sheath analysis is used to describe the quasi-static behavior of the instrument. We extend the available model of a single tendon-sheath transmission to the case of a dual tendon-pulley system. Based on the mathematical model of a dual tendon-sheath system, two simplified quasi-static models of the da Vinci instrument are proposed. Experimental results demonstrate that a certain linear combination of the outputs of the two models provides a sufficiently close estimate of the output torque of the da Vinci instrument.
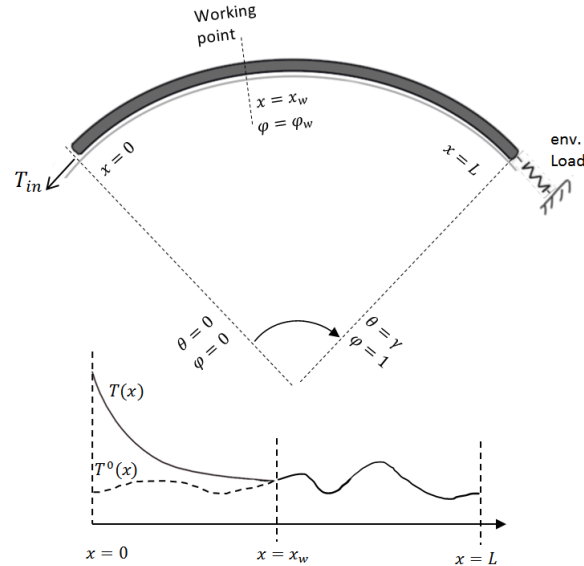
Figure 2.2: A tendon on a curved surface with constant curvature

## 2.2   Quasi-Static Analysis of Tendon Force Transmission in the Presence of Friction

In this section, a quasi-static model of a single tendon moving on a curved sheath or a curved surface is described; subsequently, the theory is extended to the case of two tendons in a pull-pull configuration. The derivations below are based on the theory presented in [8, 9]. Consider a tendon slipping on a curved surface with length $L$ and a constant radius of curvature $R$ shown in Figure 2.2 (top), where the interaction between the tendon and the surface is described by the Coulomb friction model. The tendon is elastic, and its strain-stress relation is described by Hooke's law. Let $x \in [0, L]$ denote the position along the curve, and let $T^0(x)$ be the initial tension distribution in the tendon. If a sufficiently large input force $T_{in}$ is applied to the free end of the tendon, the tension distribution over the curve changes to $T(x)$; an example of such a change is shown in Figure 2.2 (bottom). More precisely, depending on the magnitude of the input force $T_{in}$, the tension change propagates into a part of the tendon over the surface length described by $x \in [0, x_w)$, where $x_w \geq 0$ depends on the input force $T_{in}$ and the pretension $T^0(x)$. The part of the tendon that matches $x \in [0, x_w]$ is called *the active length*[1] of the tendon. For an infinitesimal segment of the tendon within its active length (shown in Figure 2.3), one can write the following

---

[1]Corresponding to the slip zone on the surface as explained in Chapter 1, under the classic creep theory.

force balance equations,

$$dT = F = \mu N \, \mathrm{sgn}(v), \tag{2.1}$$

$$N = (2T + dT)\sin(d\theta/2) \approx T d\theta = (T/R)dx, \tag{2.2}$$

where $T$, $F$, and $N$ are the tension, the Coulomb friction force, and the normal force at a
point $x \in (0, x_w)$, respectively, $v$ is the velocity of the element with respect to the surface,
$d\theta$ is the bending angle of the element, and $\mu \geq 0$ is the Coulomb friction coefficient. The
switching function $sgn(x)$ is defined as:

$$sgn(x) = \begin{cases} 1, & \text{if } x > 0 \\ 0, & \text{if } x = 0 \\ -1, & x < 0. \end{cases} \tag{2.3}$$

Substituting (2.2) into (2.1), one obtains the following equation

$$dT = (\mu T/R)\,\mathrm{sgn}(v)dx, \tag{2.4}$$

that describes the tension change in an infinitely small element of a tendon centred at $x \in
(0, x_w)$. Integrating (2.4) results in the following formula for tension distribution within the
active length of the tendon $x \in (0, x_w)$

$$T(x) = T_{in}e^{\frac{\mu}{R}x\,\mathrm{sgn}(v)}. \tag{2.5}$$

The upper bound $x_w$ of the active length of the tendon can be calculated according to the
formula

$$x_w := \min\{x \in [0, L]: \ T_{in}e^{\frac{\mu}{R}x\,\mathrm{sgn}(v)} = T^0(x)\}. \tag{2.6}$$

The tension in the remaining part of the tendon does not change[2]. Overall, the tension
distribution in the presence of an external force $T_{in}$ applied to the free end of the tendon is

---

[2]The assumption that the tension in the stationary part of the tendon does not change is used in [8, 9]. The
same assumption is also used in the classical creep theory in belt mechanics. More advanced theories, such
as the microslip theory [13], address the change of tension in the stationary part(s) also.
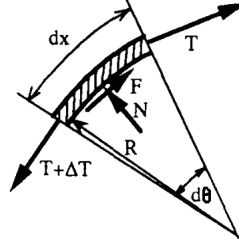
Figure 2.3: An infinitesimal element of the tendon [8]

described by the formula

$$T(x) = \begin{cases} T_{in} \, e^{\frac{\mu}{R} x \, sgn(v)} & 0 \leq x \leq x_w, \\ T^0(x) & x_w < x \leq L. \end{cases} \tag{2.7}$$

As $T_{in}$ increases, the wave of tension propagates from the input side towards the opposite
end.

On the other hand, increased tension results in elongation of the tendon which is described
by Hooke's law [14]. Specifically, the elongation of an infinitesimal element of the tendon
due to the change of tension from $T^0(x)$ to $T(x)$ is described by the following formula[3]

$$d\Delta(x) = \frac{T(x) - T^0(x)}{EA} dx, \tag{2.8}$$

where $d\Delta(x)$ is the elongation of the element $dx$, $E$ is Young's modulus, and $A$ is the
cross-sectional area of the tendon. The total elongation $\Delta$ can be found by integrating (2.8)
over the curve,

$$\Delta = \int_0^L d\Delta(x) = \frac{1}{EA} \int_0^L (T(x) - T^0(x))dx. \tag{2.9}$$

Normalizing the upper limit of the integral in (2.9) by changing the integration variable to
$\varphi := x/L$ results in the following formula

$$\Delta = \frac{1}{K_t} \int_0^1 (T(\varphi) - T^0(\varphi))d\varphi, \tag{2.10}$$

where $K_t := EA/L$ is the total stiffness of the tendon.

The approach outlined above can be used for modeling of a dual pulley-tendon mechanism

---

[3]According to the notation introduced in Chapter 1, $d\Delta(x) = dl(x) - dl_{ref}(x)$ and $dx \equiv dl_{ref}$.

shown in Figure 2.4. In this case, the input pulley with radius $r_1$ is connected to the output pulley $r_2$ using two tendons where, similar to the above considerations, each tendon slips over a curved surface. For the sake of generality, it is assumed that the tendons may have different transmission parameters. In quasi-static conditions, the input and the output torques are related to the tendons' tensions according to the following formulas

$$\tau_{in} = (T_{tl} - T_{bl})r_1, \quad \tau_{out} = (T_{tr} - T_{br})r_2, \tag{2.11}$$

where $T_{tl}$, $T_{bl}$, $T_{tr}$, $T_{br} \geq 0$ are the tensions in the tendon ends as shown in Figure 2.4. The subscripts $l$, $r$, $t$, and $b$ stand for left, right, top, and bottom, respectively.
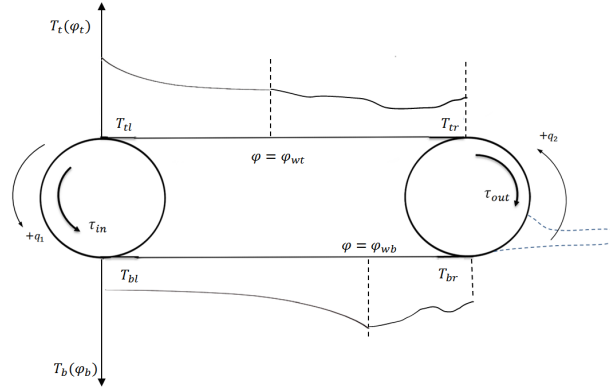


Figure 2.4: A dual tendon-sheath (pull-pull) system.

Based on the assumptions made above, the formulas for tensions and elongations of the two tendons can be written as follows:

$$T_t(\varphi_t) = \begin{cases} T_{tl}\, e^{-\eta_t \varphi_t \, \mathrm{sgn}(\dot{q}_1)} & \varphi_i < \varphi_{wt}, \\ T_t^0(\varphi_t) & \varphi_t \geq \varphi_{wt}, \end{cases} \tag{2.12}$$

$$T_b(\varphi_b) = \begin{cases} T_{bl}\, e^{\eta_b \varphi_b \, \mathrm{sgn}(\dot{q}_1)} & \varphi_b < \varphi_{wb}, \\ T_b^0(\varphi_b) & \varphi_b \geq \varphi_{wb}, \end{cases} \tag{2.13}$$

$$\Delta_i = \frac{1}{K_{ti}} \int_0^1 (T_i(\varphi_i) - T_i^0(\varphi_i))d\varphi_i, \tag{2.14}$$

where the subscript $i = \{t, b\}$ represents the top and the bottom tendons in Figure 2.4, respectively, and $\eta := \mu L/R$ is a dimensionless parameter which represents the effects of

both the bending and the Coulomb friction.

Assuming that the tendons' slippages over the pulleys are negligible, we can relate the elongations of the tendons to the rotation of the input and output pulley,

$$\Delta_t = \Delta q_1 r_1 - \Delta q_2 r_2, \quad \Delta_b = \Delta q_2 r_2 - \Delta q_1 r_1, \tag{2.15}$$

where $\Delta q_1$ and $\Delta q_2$ are the changes of angles of rotation for the input and the output pulley, respectively. The fact that the sum of elongations of the tendons $\Delta_t$ and $\Delta_b$ are zero, implies that a stretch in one tendon is compensated by an equivalent shrinkage in the other tendon, as long as none of the tendons has gone slack. In view of (2.14), the constraint equation $\Delta_t + \Delta_b = 0$ can be rewritten in the form

$$\int_0^1 (T_t(\varphi_t) - T_t^0(\varphi_t))d\varphi_t = -\int_0^1 (T_b(\varphi_b) - T_b^0(\varphi_b))d\varphi_b,$$

or

$$\int_0^1 (T_t d\varphi_t + T_b d\varphi_b) = \int_0^1 (T_t^0 d\varphi_t + T_b^0 d\varphi_b) = I, \tag{2.16}$$

where $I$ is a constant. Equation (2.16) is an important constraint which holds in a dual tendon-sheath system as long as none of the tendons becomes slack[4].

## 2.3 Modeling

In [10], the overall backlash-like transmission characteristics of a typical tendons-based transmission system in a pull-pull configuration have been demonstrated to have the shape shown in Figure 2.5. More specifically, if an input torque with sufficiently low frequency and sufficiently large amplitude is applied to the system shown in Figure 2.4, the response of the system consists of the following four phases.

- **Phase I**, during which the input torque is being applied but the corresponding change of tension has not yet been propagated to the output pulley; as a result, no change in the output torque can be observed.

---

[4]This is a variation of the compatibility condition (1.24) introduced in Chapter 1.
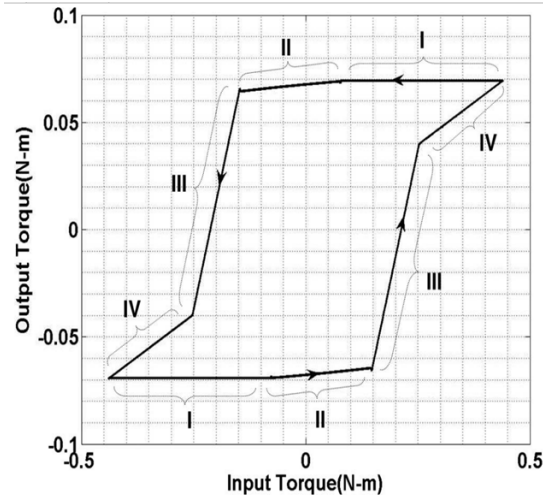
Figure 2.5: A typical input-output relation for a tendon-sheath mechanism in pull-pull architecture [10].

- **Phase II**, during which the change in tension due to the input torque has already reached the output pulley; however, the change in tension in the tendon that is being pushed has not yet reached the other end.

- **Phase III**, during which both the pulled and the pushed tendons transfer the force to the output pulley, *i.e.*, the whole length of both the tendons is active.

- **Phase IV**, where the pushed tendon has become slack while the pulled tendon is engaged in its whole length and is transferring force.

Even though the above four phases can typically be observed in practical systems, some of them may be ignored for the sake of modelling simplicity. In this study, two simplified models are used: i) a *pull model* which is based on Phases I and IV, and ii) a *pull-push model* which is based on Phases I and III.

## 2.3.1   Pull-Model

Under zero pretension condition, the tendon does not transfer force when pushed. On the other hand, if nonzero pretension exists, the tension distribution is described by equations (2.7). In our first model, the *pull model*, it is assumed that the force is being transferred

only through the pulled tendon, while the other (pushed) tendon does not transfer the force and is considered slack. This assumption corresponds to Phase IV above. Moreover, it is assumed that the tension propagates through the whole length of the tendon immediately; in other words, one has $\varphi_{wt} = \varphi_{wb} = 1$ in (2.12). Based on the above two assumptions, it follows from (2.12) that the tension in the tendon ends are described according to the following formulas:

$$\begin{aligned}
T_{tr} &= K(\dot{q}_1)\, T_{tl}\, e^{-\eta_t\, \mathrm{sgn}(\dot{q}_1)}, \\
T_{br} &= (1 - K(\dot{q}_1))\, T_{bl}\, e^{\eta_b\, \mathrm{sgn}(\dot{q}_1)},
\end{aligned} \tag{2.17}$$

where

$$K(x) := \begin{cases} 1 & x > 0, \\ 0 & x < 0. \end{cases}$$

In particular, formula (2.17) implies that the tension in the pushed tendon is zero.

Equations (2.11), (2.17) describes the model of the system that corresponds to Phase IV. The process of switching between Phases IV and I, on the other hand, is described by the following equation

$$\tau_{out}^{pl} = K(T_{tr})K(T_{br})\tau_{out} + (1 - K(T_{tr})K(T_{br}))\tau_{out}^{-}, \tag{2.18}$$

where $\tau_{out}^{pl}$ is the output of the pull model, and $\tau_{out}^{-}$ is defined as $\tau_{out}^{-}(t) := \tau_{out}(t^-)$, where $t^- := \sup\{s \le t :\ K(T_{tr}(s))K(T_{br}(s)) = 1\}$. In words, $t^-(t)$ is the last instant when the model (2.11), (2.17) returned nonnegative tensions $T_{tr}, T_{br}$. Equations (2.11), (2.17), (2.18) constitute the pull model.

## 2.3.2   Pull-Push Model

The *pull-push model* corresponds to Phases III and I. During Phase III, both tendons are fully active; assuming that the tension propagates immediately though the whole length of the tendon ($\varphi_{wt} = \varphi_{wb} = 1$ in (2.12)), from (2.12) one concludes that the following relations hold:

$$T_{tr} = e^{-\eta_u\, \mathrm{sgn}(\dot{q}_1)}T_{tl}, \quad T_{br} = e^{\eta_d\, \mathrm{sgn}(\dot{q}_1)}T_{bl}. \tag{2.19}$$

Also, since none of the tendons is slack during Phase III, the constraint (2.16) holds. Substituting (2.19) in (2.16) results in

$$T_{bl}\frac{\text{sgn}(\dot{q}_1)}{\eta_d}(e^{\eta_d \text{sgn}(\dot{q}_1)} - 1) - T_{tl}\frac{\text{sgn}(\dot{q}_1)}{\eta_u}(e^{-\eta_u \text{sgn}(\dot{q}_1)} - 1) = I. \qquad (2.20)$$

Equations (2.11), (2.19), and (2.20) describe the behavior of the model during Phase III. The switching between Phases III and I is performed according to the following formula

$$\tau_{out}^{pp} = K(T_{tr})K(T_{br})K\left(\dot{q}_1(T_{tr} - T_{br})\right)\tau_{out} + \left(1 - K(T_{tr})K(T_{br})K\left(\dot{q}_1(T_{tr} - T_{br})\right)\tau_{out}^-,\right.$$
$$(2.21)$$

where $\tau_{out}^{pp}$ is an output of the pull-push model, and $\tau_{out}^-$ is defined as $\tau_{out}^-(t) := \tau_{out}(t^-)$, where $t^- := \sup\{s \leq t: \ K(T_{tr}(s)) = 1, K(T_{br}(s)) = 1, \text{ and } K(\dot{q}_1(s)(T_{tr}(s) - T_{br}(s))) = 1\}$. The term $K(\dot{q}_1(T_{tr} - T_{br}))$ ensures that the pulling force is always greater than the pushing force. Equations (2.11), (2.19), (2.20), and (2.21) describe the pull-push model.

## 2.4 Experimental Results

### 2.4.1 The Experimental Setup

The two simplified quasi-static models derived above have been used for modelling of the EndoWrist™ grasper utilized in the da Vinci surgical robot. The EndoWrist™ grasper is a state-of-the-art laparoscopic instrument which consists of four sets of tendon-pulley mechanisms in a highly compact arrangement. The mechanisms transmit power from the base through a narrow shaft to the tip of the instrument and provide the tip with 4-DOF motion capability similar to the one of the human hand [15]. For each degree of freedom, a separate tendon is wrapped around several pulleys, including the input pulley which is attached to the actuator and the output pulley attached to the tip. In order to identify the parameters and evaluate the performance of the proposed models, experiments were conducted using a specially designed setup shown in Figure 2.6. In this setup, the base of the da Vinci instrument, in this case the EndoWrist™ grasper, is mounted on an actuation mechanism which is fixed on a 6 DOF gripper. The shaft of the instrument is also fixed to the ground. On the actuation holder, four Faulhaber DC motors apply torques to the input pulleys at the
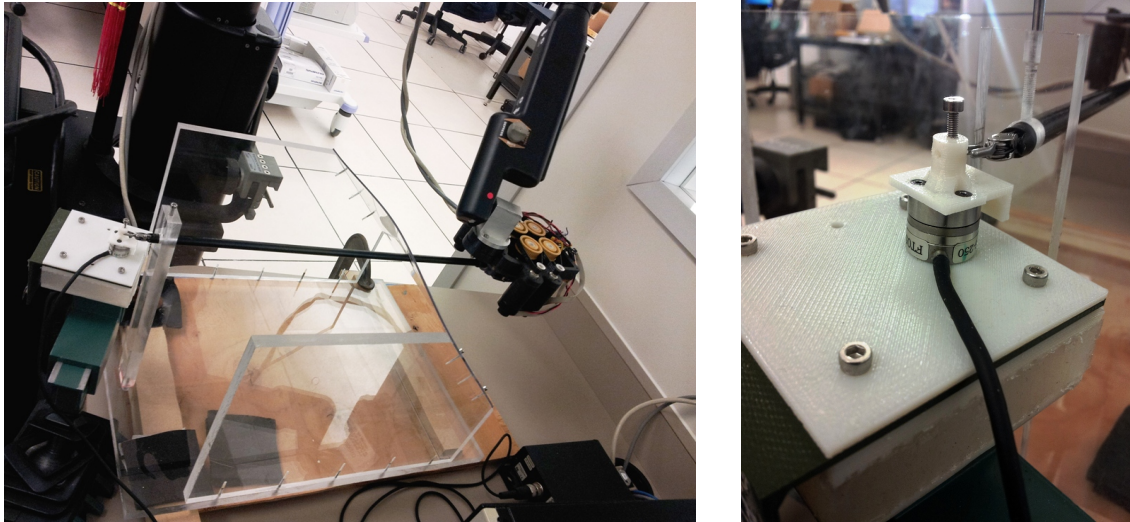
Figure 2.6: The experimental setup: the overall view (left); the force sensor close-up (right)

base of the instrument. The positions of the motors are read by incremental encoders with 2048 counts per turn. The amplifiers of motors are set to the voltage-to-current mode so that the commanded voltage is proportional to the input torque. At the output side, the tip of the instrument is fixed on top of an ATI Nano17 force sensor. The identification and the model validation procedures in this paper have been performed for the gripping DOF of the instrument; for other DOFs/configurations, similar procedures can be used.

## 2.4.2 Instrument Parameter Identifications

In order to utilize the above derived quasi-static models in the case of a dual tendon mechanism, four parameters have to be identified which are the friction-bending parameters $\eta_t$, $\eta_b$ and the stiffness parameters $K_{tt}$, $K_{tb}$. In addition, in the case of the push-pull model, the constraint parameter $I$ must be identified. The values of $r_1 = 2.6$ mm and $r_2 = 2.4$ mm were obtained by direct measurement using a caliper. The method used in our identification procedure is to apply sufficiently large input torque such that one of the tendons goes slack while the other is fully tight, and subsequently identify the parameters of the tight tendon. Following this method, a triangular wave of torque shown in Figure 2.7, left, is applied to the input pulley. The amplitude of the input torque is $0.155$ N·m which is sufficiently large torque for the instrument under study, while the rate of change of the input torque is

kept low at $0.015$ N·m/sec in order to ensure the quasi-static conditions. Figure 2.7, right, demonstrates the experimentally obtained hysteresis-type relationship between the magnitude of the input torque on one hand and the output torque and output displacement on the other hand. This figure clearly demonstrates that the input-output behavior of the system is quite similar to the one that characterizes the tendon-sheath transmission as shown in Figure 2.5. The procedures for identification of parameters $\eta$, $K_t$, and $I$ used in our work are explained below.
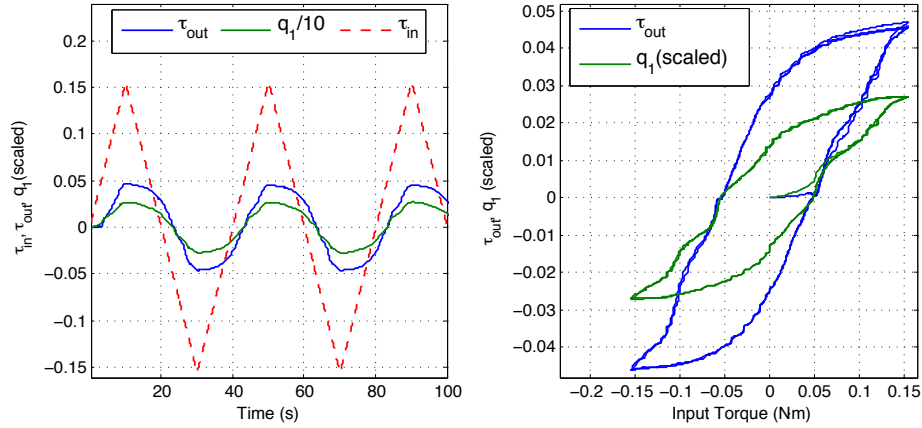


Figure 2.7: Left plot: the input torque $\tau_{in}$, the output torque $\tau_{out}$, and the angular position $q_1$ (scaled) vs. time, the tip is locked ($q_2 \equiv 0$). Right plot: $\tau_{out}$ and $q_1$ (scaled) vs. $\tau_{in}$.

### 2.4.2.1 Identification of $\eta_t$ and $\eta_b$

Assuming that large enough torque is applied to the mechanism in Figure 2.4 such that one of the tendons is fully tight while the other is slack, it follows from (2.12) that $\eta_i = -\ln(T_{ir}/T_{il})$, where $i = t$ if the top tendon is fully tight and the bottom one is slack, and $i = b$ in the opposite case. Then from (2.11) one obtains

$$\eta_i = -\ln\left(\frac{\tau_{out}\, r_1}{\tau_{in}\, r_2}\right). \tag{2.22}$$

Therefore, under the condition that one of the tendons is fully tight and the other is slack, the formula (2.22) is expected to return approximately constant values that would correspond to either $\eta_t$ or $\eta_b$ (more precisely, the formula (2.22) would return the value of $\eta_t$ if the top tendon is tight and the bottom one is slack, and the value of $\eta_b$ in the opposite case).

The method that we use to determine the values of the friction-bending parameters $\eta_t$, $\eta_b$ is as follows. During the experiment, when the above described triangle wave of input torque is applied to the instrument, an estimate of the parameter $\eta$ is continuously calculated using the formula (2.22). The result of this experiment is illustrated in Figure 2.8, where the value of $\eta_i$ calculated using formula (2.22) is superimposed on a scaled input torque curve. It is clearly seen that the curve $\eta_i$ settles down to approximately constant values when the magnitude of input torque is greater than certain threshold(s). The instants where $\eta_i$ settles down to approximately constant values are denoted by circles in Figure 2.8; for convenience, we call these *slack instants* as at these instants one of the tendons goes slack. Table 2.1 summarizes the values of $\eta_t$, $\eta_b$ and the input torque $\tau_{in}$ at each slack instant; it can be seen that these values are relatively consistent across the set of slack instants. Averaging the experimentally obtained values of the friction-bending parameters $\eta_t$, $\eta_b$, one gets $\eta_t \approx 1.1414$ and $\eta_b \approx 1.1404$, respectively.
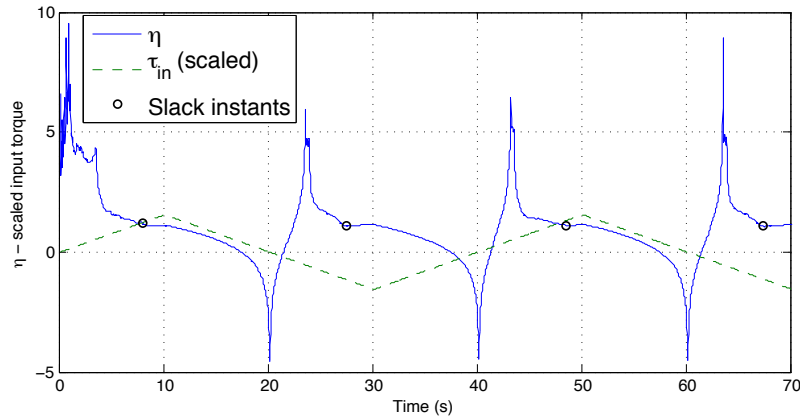


Figure 2.8: Estimate $\eta$ and the input torque (scaled) $\tau_{in}$ vs. time.

Table 2.1: Values of $\eta_t$ and $\eta_b$ measured at the slack instants $t^s$

| time | $t_1^s$=8.08 | $t_2^s$=27.52 | $t_3^s$=48.54 | $t_4^s$=67.36 | $t_5^s$=88.28 |
|---|---|---|---|---|---|
| $\tau_{in}$ | 0.1227 | -0.1140 | 0.1299 | -0.1115 | 0.1258 |
| $\eta_t$ | 1.1236 | - | 1.1527 | - | 1.1479 |
| $\eta_b$ | - | 1.1430 | - | 1.1384 | - |

### 2.4.2.2  Identification of $K_{tt}$ and $K_{tb}$

Formula (2.14) implies that the tendons' stiffnesses $K_{tt}$ and $K_{tb}$ can be calculated based on known tension distributions at two different instants of time and the corresponding equivalent elongations of the tendons. In our calculations, the two time instants are a slack instant $t_s$ and the instant $t_p$ when the torque achieves its maximum value. Since between these instants the pulled tendon remains fully tight and the pushed tendon fully slack, the corresponding tension distributions can be calculated using formulas (2.12). On the other hand, since the tip of the instrument is locked ($\Delta q_2 \approx 0$), the elongation of the tendon can be calculated based on the amount of rotation of the input pulley between $t_s$ and $t_p$. Specifically, (7.2) implies that

$$\Delta_t = -\Delta_b = (q_1(t_p) - q_1(t_s))r_1. \tag{2.23}$$

Based on the tension distributions and the corresponding elongations, the tendons' stiffness can be calculated using (2.14). For example, if the top tendon is tight, then the tension distribution at time $t_s$ is given by the formula

$$T_t(\varphi_t) = T_{tl}(t_s)e^{-\eta_t \varphi_t} = (\tau_{in}(t_s)/r_1) \cdot e^{-\eta_t \varphi_t}, \tag{2.24}$$

while the tension distribution at time $t_p$ is

$$T_t(\varphi_t) = T_{tl}(t_p)e^{-\eta_t \varphi_t} = (\tau_{in}(t_p)/r_1) \cdot e^{-\eta_t \varphi_t}. \tag{2.25}$$

Substituting (2.24) and (2.25) into (2.14) and using (2.23), one gets the following formula for $K_{tt}$,

$$K_{tt} = \frac{\tau_{in}(t_p) - \tau_{in}(t_s)}{q_1(t_p) - q_1(t_s)} \cdot \frac{(e^{-\eta_t} - 1)}{-r_1^2 \eta_t}. \tag{2.26}$$

The formula for $K_{tb}$ can be obtained in a similar manner. Experimental results give the following average values of the stiffnesses: $K_{tt} = 5.0664 \cdot 10^4$ N/m and $K_{tb} = 5.0831 \cdot 10^4$ N/m.

### 2.4.2.3 Identification of $I$

The constant $I$ can be found based on the tension distribution in the tendons using formula (2.16). At the instants where the bottom tendon goes slack, $T_t(\varphi_t)$ is given by (2.24), and $T_b(\varphi_b) \approx 0$. Table 2.2 shows the corresponding values of $I$ at different slack instances. On average, $I = 27.6984$.

Table 2.2: Constant $I$ measured at the slack instants

| time | $t_1^s$=8.08 | $t_2^s$=27.52 | $t_3^s$=48.54 | $t_4^s$=67.36 | $t_5^s$=88.28 |
|------|--------------|---------------|---------------|---------------|---------------|
| $I$  | 28.1393      | 26.1471       | 29.7820       | 25.5756       | 28.8535       |

## 2.4.3 Model Performance

After all the parameters are identified, the performance of the suggested pull model and the pull-push model can be evaluated. Figure 2.9 shows the responses of the two models with the same triangular input torque signal together with the actual response of the da Vinci instrument. One can observe that the actual response lies somewhere between the estimates provided by the pull model and the pull-push model. Comparing the transmission behavior of a dual-tendon transmission system reported in [8] and [10], one can conclude that the behavior of such a system can be closely described by the pull-model when the pretension of the mechanism is low, while it is more similar to the behavior of the pull-push model when the pretension is high. Therefore, one possible solution is to use a linear combination of both models, as follows:

$$\bar{\tau}_{out} = w_1 \tau_{out}^{pl} + w_2 \tau_{out}^{pp}, \tag{2.27}$$

where the coefficients $w_1 = 0.5904$ and $w_2 = 0.4686$ have been determined using the least-squares identification procedure. The performance of the proposed model (2.27) has been tested in several experiments; some of the results are shown in Figure 2.10. In this figure, the responses of the actual da Vinci instrument are shown together with the corresponding estimates obtained using the model (2.27), for different input torques $\tau_{in}(t)$. It can be seen that the model (2.27) provides a sufficiently close estimate of the output torque in all these cases.
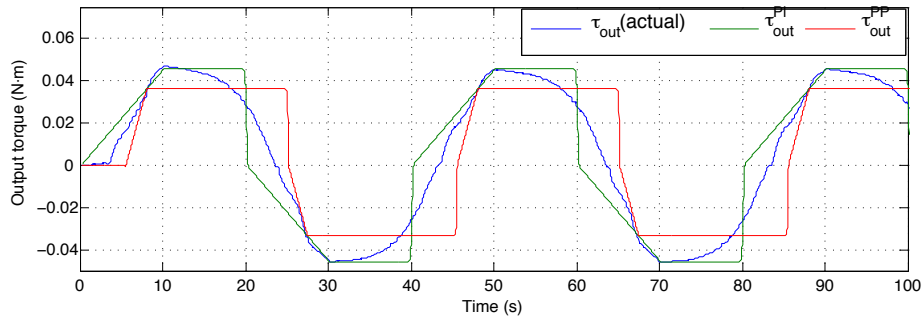
Figure 2.9: Estimates $\tau_{out}^{pl}$, $\tau_{out}^{pp}$, and the measured torque $\tau_{out}$ vs. time.
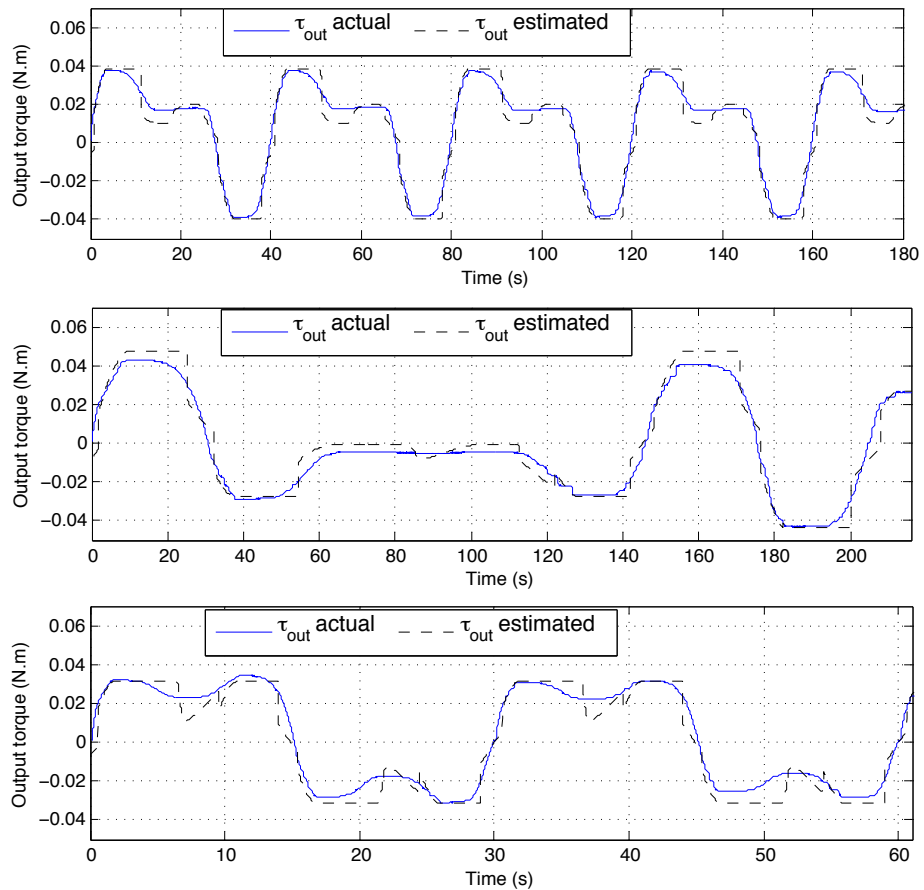


Figure 2.10: Measured output torque $\tau_{out}$ and estimate $\bar{\tau}_{out}$ vs. time, for different input torque signals. Top plot: The input signal is $\tau_{in} = 0.06228 \sin\left(2\pi \cdot 0.05t\right) + 0.06228 \sin\left(2\pi \cdot 0.025t\right)$ (N·m). Middle plot: $\tau_{in} = 0.06228 \sin\left(2\pi \cdot 0.02t\right) + 0.06228 \sin\left(2\pi \cdot 0.014t\right)$ (N·m). Bottom plot: $\tau_{in} = 0.06228 \sin\left(2\pi \cdot 0.1t\right) + 0.06228 \sin\left(2\pi \cdot 0.03t\right)$ (N·m).

# References

[1] A. M. Okamura, "Haptic feedback in robot-assisted minimally invasive surgery," *Current Opinion in Urology*, vol. 19, pp. 102–107, 2009.

[2] A. L. Trejos, R. V. Patel, and M. D. Naish, "Force sensing and its application in minimally invasive surgery and therapy: a survey," *Institution of Mechanical Engineers, Part C: Journal of Mechanical Engineering Science*, vol. 224, pp. 1435 –1454, 2010.

[3] Intuitive Surgical, Inc., *EndoWrist: Instrument and Accessory Catalog*, July 2011.

[4] G. Borghesan, G. Palli, and C. Melchiorri, "Design of tendon-driven robotic fingers: Modeling and control issues," in *IEEE International Conference on Robotics and Automation (ICRA)*, pp. 793–798, IEEE, 2010.

[5] D. J. Abbott, C. Becke, R. I. Rothstein, and W. J. Peine, "Design of an endoluminal NOTES robotic system," in *IEEE/RSJ International Conference on Intelligent Robots and Systems (IROS)*, pp. 410–416, 2007.

[6] A. Nahvi, J. M. Hollerbach, Y. Xu, and I. W. Hunter, "An investigation of the transmission system of a tendon driven robot hand," in *IEEE/RSJ/GI International Conference on Intelligent Robots and Systems IROS 94*, vol. 1, pp. 202–208, IEEE, 1994.

[7] M. Grebenstein, M. Chalon, W. Friedl, S. Haddadin, T. Wimböck, G. Hirzinger, and R. Siegwart, "The hand of the DLR hand arm system: Designed for interaction," *The International Journal of Robotics Research*, vol. 31, no. 13, pp. 1531–1555, 2012.

[8] M. Kaneko, T. Yamashita, and K. Tanie, "Basic considerations on transmission characteristics for tendon drive robots," in *IEEE Fifth International Conference on Advanced Robotics (ICAR),'Robots in Unstructured Environments'*, pp. 827–832, IEEE, 1991.

[9] M. Kaneko, M. Wada, H. Maekawa, and K. Tanie, "A new consideration on tendon-tension control system of robot hands," in *IEEE International Conference on Robotics and Automation (ICRA)*, pp. 1028–1033, IEEE, 1991.

[10] V. Agrawal, W. J. Peine, and B. Yao, "Modeling of transmission characteristics across a cable-conduit system," *IEEE Transactions on Robotics*, vol. 26, no. 5, pp. 914–924, 2010.

[11] V. Agrawal, W. J. Peine, B. Yao, and S. Choi, "Control of cable actuated devices using smooth backlash inverse," in *IEEE International Conference on Robotics and Automation*, pp. 1074–1079, IEEE, 2010.

[12] G. Palli, G. Borghesan, and C. Melchiorri, "Modeling, identification, and control of tendon-based actuation systems," *IEEE Transactions on Robotics*, vol. 28, no. 2, pp. 277–290, 2012.

[13] C. H. Menq, J. Bielak, and J. H. Griffin, "The influence of microslip on vibratory response, part i: a new microslip model," *Journal of Sound and Vibration*, vol. 107, no. 2, pp. 279–293, 1986.

[14] E. P. Popov, *Engineering mechanics of solids*. Prentice Hall, 1990.

[15] G. Guthart and J. K. Salisbury, "The Intuitive™ telesurgery system: overview and application," in *IEEE International Conference on Robotics and Automation*, pp. 618–621, IEEE, 2000.

# Chapter 3

# Tissue Compliance Determination Using a da Vinci® Instrument

I n this Chapter, based on the *Apparent Stiffness* analysis of a dual tendon-sheath system, we propose a method for using a surgical instrument of the classic da Vinci® surgical robotic system (from Intuitive Surgical Inc.) for estimation of mechanical properties of tissue. The performance of the method is experimentally evaluated by comparing tissues with different stiffnesses and by localizing tumors in an artificial tissue sample.

## 3.1 Introduction

Haptic feedback has been demonstrated to be beneficial for the performance of the Robotics-Assisted Minimally Invasive Surgery (RAMIS) systems [1]. The technology, however, has not yet been developed to the level that satisfies the expectations of clinicians, mostly due to the complexity of mounting force sensors on the robotic instruments. A well-known example of RAMIS systems is the da Vinci® (Intuitive Surgical, Sunnyvale, CA), which provides surgeons with several advantages over conventional Minimally Invasive Surgery

(MIS), including hand-eye coordination, 3D stereoscopic vision, and motion scaling. However, it does not provide haptic feedback that can reflect tool-tissue interaction forces to the surgeon's hands [2, 3].

Palpation is one of the essential functions performed by a surgeon which provides invaluable intraoperative information of the mechanical properties of the affected organs. For many tasks, such as tumor localization, palpation plays a major role in determining the boundaries of tumors even in the presence of preoperative imaging data [3]. In MIS and RAMIS, however, the surgeon's hands are not in direct contact with the operative field. As a result, the surgeon's feel of touch is drastically deteriorated in the former case, while completely disappears in the latter. To provide surgeons with haptic feedback, sensorized laparoscopic devices have been developed [4–7].

In this Chapter, some preliminary results are presented that show feasibility of determining a relative stiffness distribution in a tissue sample when doing palpation using the da Vinci instrument. The study is a continuation of the work reported in [8], where a da Vinci instrument was modeled using quasi-static tendon-sheath analysis[1]. Here, the analysis of [8] is further extended to derive a model that describes the *apparent stiffness/compliance* of the instrument, from which information about stiffness/compliance of the environment can subsequently be extracted. Based on the derived model, a method for determination of environmental compliance is proposed and experimentally justified.

The Chapter is organized as follows. In Section 3.2, a model that describes the apparent stiffness in tendon-sheath force transmission is derived, and subsequently extended to the case of dual tendon-sheath mechanisms. Since the hysteresis in force transmission of a typical dual-tendon mechanism has been shown to have four phases, in Section 3.3, the apparent stiffness in each phase is analyzed together with its effect on the *combined stiffness* of the system. Also, a method for estimation of the environmental compliance is proposed in this section. The hypothesis of the chapter is given in Section 3.3. The experimental setup is described in Section 3.5. In Section 3.6, two experiments are reported where the performance of the method for environmental compliance discrimination and tumour

---

[1]The tendon-sheath analysis can be used to describe a tendon-pulley based instrument due to the fact that both types of systems demonstrate similar behavior, as described in Chapter 2. Applicability of the tendon-sheath analysis for tendon-pulley transmissions, nonetheless, can be further justified in a more rigorous manner. This is elaborated in Chapter 5.
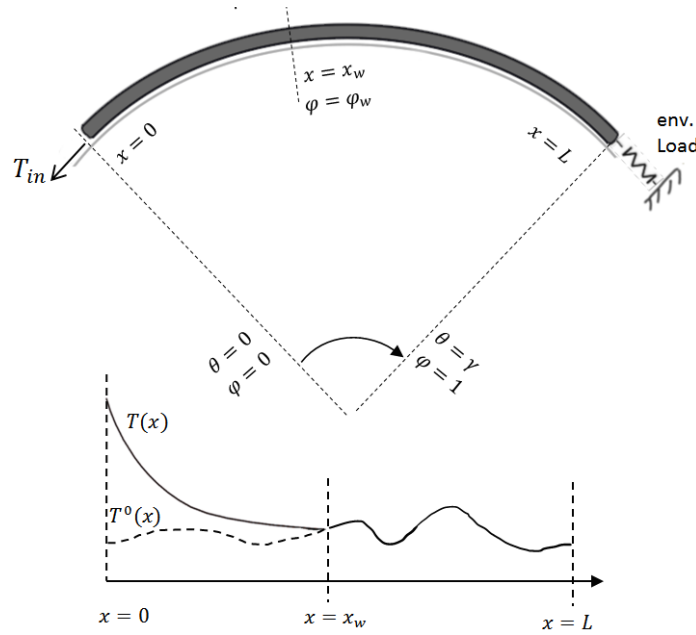
Figure 3.1: A tendon on a curved surface with a constant curvature (top); example of tension distribution (bottom) [8]

localization tasks is examined. Conclusions are given in Section 3.7.

## 3.2 Apparent Stiffness of a Tendon-Sheath Force Transmission System

In this section, we derive a mathematical model that describes the apparent stiffness of a tendon which slides on a curved surface or moves in a curved sheath. In this study, the apparent stiffness of a tendon-drive is defined as the stiffness which is seen from the point of view of the actuator. Subsequently, we extend the formula to the case of a dual tendon-sheath system. In contrast with the case of a free tendon, the stiffness of a tendon-sheath force transmission system is input-dependent and, therefore, not constant [9]. The derivations below are based on the quasi-static analysis of a dual tendon-sheath force transmission system developed in [8].

The equations that describe the tension distribution $T(\varphi)$ and the tendon elongation $\Delta$ in a single tendon-sheath mechanism (shown in Figure 3.1) in the presence of input force $T_{in}$

can be written as follows [8]:

$$T(\varphi) = \begin{cases} T_{in}\, e^{\varphi\eta\,\mathrm{sgn}(v)} & 0 \leq \varphi \leq \varphi_w, \\ T^0(\varphi) & \varphi_w < \varphi \leq 1, \end{cases} \tag{3.1}$$

$$\Delta = \frac{1}{K_n} \int_0^1 (T(\varphi) - T^0(\varphi))d\varphi, \tag{3.2}$$

where $\varphi := x/L \in [0,1]$ is a normalized position along a tendon with length $L > 0$, $\eta := \mu L/R$ is a dimensionless parameter which represents the effects of both the bending and the Coulomb friction where $R > 0$ is the curvature of the tendon and $\mu$ is the Coulomb friction coefficient. Also, $K_n := EA/L$ is the natural stiffness of the free tendon, where $E$ denotes the modulus of elasticity and $A$ is the cross-sectional area of the tendon. Furthermore, $T^0(\varphi)$ is the initial tension distribution (pretension) before the application of the input force $T_{in}$, $T(\varphi)$ is the tension distribution after the input force $T_{in}$ is applied, and $\varphi_w$ is the upper bound of the active length of the tendon, *i.e.*, the part of the tendon where the tension distribution changes as a result of application of the input force $T_{in}$ [8][2]. Also, $v$ is the speed of tendon's motion in its active part; thus, $\mathrm{sgn}(v)$ essentially represents the direction of the tendon's motion in its active part.

Assuming the environmental stiffness is infinite, the apparent stiffness $K_{app}$ of the tendon can be defined according to the formula

$$\frac{1}{K_{app}} := \frac{d\Delta}{dT_{in}}, \tag{3.3}$$

where $d\Delta$ is the infinitesimal change of the tendon's length resulting from an infinitesimal change of the input force $dT_{in}$. Combining (3.2) and (3.3) gives

$$\frac{1}{K_{app}} = \frac{1}{K_n}\frac{d}{dT_{in}}\left(\int_0^1 (T(\varphi) - T^0(\varphi))d\varphi\right). \tag{3.4}$$

On the other hand, the expression for tension distribution in (3.1) can be substituted for

---

[2]In accordance to the creep theory, the active length of the tendon can be called the slip zone of the interaction.

$T(\varphi)$ in (3.4), resulting in the following formula:

$$\frac{1}{K_{app}} = \frac{1}{K_n} \frac{d}{dT_{in}} \left( \int_0^{\varphi_w} T_{in} \, e^{\eta\varphi \, sgn(v)} d\varphi \right). \tag{3.5}$$

The formula for apparent stiffness can therefore be found by integrating (3.5), which gives

$$\frac{1}{K_{app}} = \frac{1}{K_n} T_{in} e^{\eta\varphi_w \, sgn(v)} \frac{d\varphi_w}{dT_{in}} + \frac{1}{K_n} \frac{sgn(v)}{\eta} (e^{\eta\varphi_w \, sgn(v)} - 1). \tag{3.6}$$

The first term to the right-hand side of the formula (3.6) can be considered as the transient part of the apparent stiffness which is dominant when change of tension just started to propagate (*i.e.*, when $\varphi_w \approx 0$), and disappears as soon as the tension propagation reaches to the other end, *i.e.,* when $\varphi_w = 1^3$. Neglecting the transient part results in the following formula for the apparent stiffness,

$$K_{app} \approx K_n \frac{\eta sgn(v)}{e^{\eta\varphi_w \, sgn(v)} - 1}. \tag{3.7}$$

Formula (3.7) implies that, as the upper bound of the active length $\varphi_w$ moves from zero to 1, the apparent stiffness of the tendon changes from infinity to a certain minimum value. In particular, if a tendon is active in its whole length, the apparent stiffness is equal to the following minimum values that depend on the direction of motion $sgn(v)$:

$$k_{app}^{min-pull} = K_n \frac{\eta}{1 - e^{-\eta}}, \tag{3.8}$$

and

$$k_{app}^{min-push} = K_n \frac{\eta}{e^{\eta} - 1}. \tag{3.9}$$

The two formulas (3.8) and (3.9) were originally reported in [9, 10]. Figures 3.2(a) and 3.2(b) (borrowed from [9]) illustrate the changes of apparent stiffness in a single tendon-sheath force transmission system.

The theory presented above can be extended to the case of dual tendon-sheath force transmission mechanisms such as the one shown in Figure 3.3. It is again assumed that the

---

[3]Based on the current assumptions on friction, applying $T_{in}$ results in two independent stick and slip zone in a way that $dT_{in}$ makes no change to the tendon in the stick zone. Therefore, $\frac{d\varphi_w}{dT_{in}}$ can not be exactly defined. A more advanced friction model can potentially be used here.
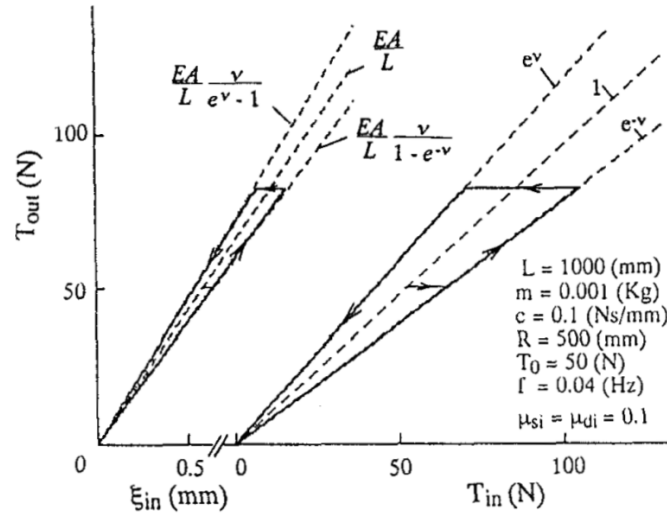
(a)
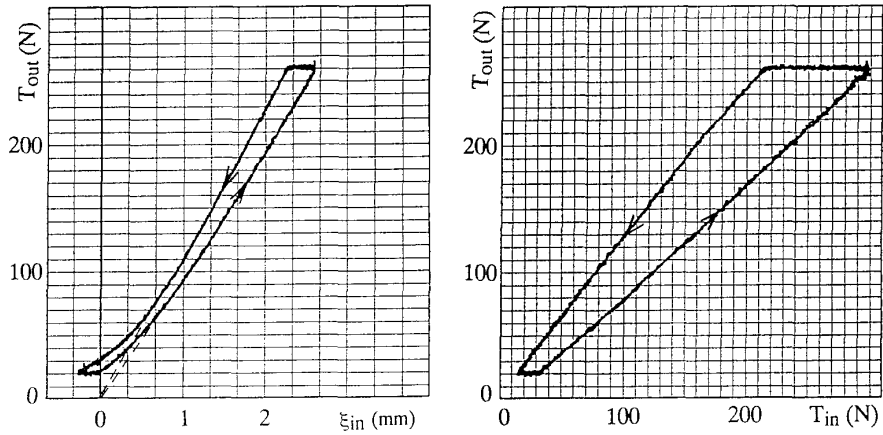


(b)

Figure 3.2: a) Numerical simulation of transmission characteristics in a single tendon-sheath system, where tendon is considered a chain of mass-spring-damper elements sliding on a curved surface under conditions mentioned in the legend. The input is sinusoidal displacement with $0.04Hz$ frequency. The apparent stiffness in pushed, natural and pulled tendon is shown in the left curve as dotted lines. here, $\nu = \frac{\mu L}{R}$ is the dimensionless bending-friction parameter. Unlike our study, the apparent stiffness is calculated as a ratio of the output force $T_{out}$ to the input elongation $\xi_{in}$ but easily interchangeable by considering $T_{out} = T_{in}e^{-sgn(v)\nu}$ as shown in the right curve. b) The experimental results for a $0.4Hz$ sinusoidal input force [9].

environmental stiffness is infinite so that only the stiffness of the instrument is visible at
the input. As shown in [8], the tension distribution $T_i(\varphi_i)$, the tendon elongation $\Delta_i$, and
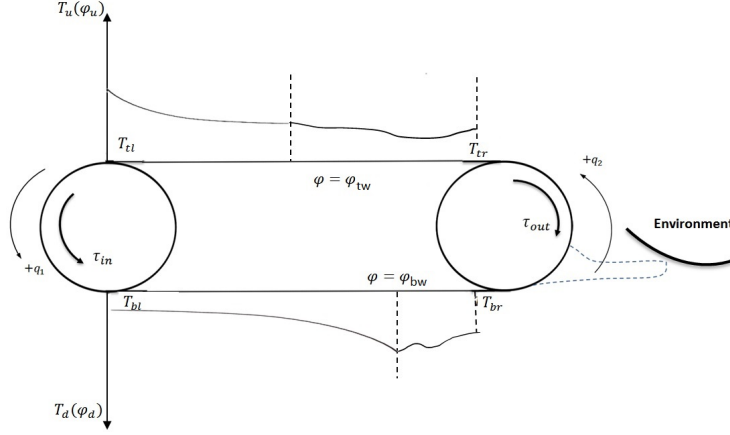


Figure 3.3: A dual tendon-sheath (pull-pull) system [8].

the force balance between the input and the output sides of a dual tendon-sheath mechanism
are described by equations

$$T_t(\varphi_t) = \begin{cases} T_{tl} \, e^{-\eta_t \varphi_t \, \text{sgn}(\dot{q}_1)} & \varphi_i < \varphi_{wt}, \\ T_t^0(\varphi_t) & \varphi_t \geq \varphi_{wt}, \end{cases} \tag{3.10}$$

$$T_b(\varphi_b) = \begin{cases} T_{bl} \, e^{\eta_b \varphi_b \, \text{sgn}(\dot{q}_1)} & \varphi_b < \varphi_{wb}, \\ T_b^0(\varphi_b) & \varphi_b \geq \varphi_{wb}, \end{cases} \tag{3.11}$$

$$\Delta_i = \frac{1}{K_{ni}} \int_0^1 (T_i(\varphi_i) - T_i^0(\varphi_i))d\varphi_i, \tag{3.12}$$

$$\tau_{in} = (T_{tl} - T_{bl})r_1, \tag{3.13}$$

$$\tau_{out} = (T_{tr} - T_{br})r_2, \tag{3.14}$$

respectively, where the subscript $i \in \{t, b\}$ denotes the top and bottom tendons in Fig-
ure 3.3, $T_{tl}, T_{bl}, T_{tr}, T_{br} \geq 0$ are the tensions in the tendon ends as shown in Figure 3.3.
The subscripts $l$, $r$, $t$, and $b$ stand for left, right, top, and bottom, respectively. Also, $\tau_{in}$
is the input torque applied by the actuator, and $\tau_{out}$ is the output torque applied to the

environment. Moreover, the following geometric relations are valid [8]:

$$\Delta_t = \Delta q_1 r_1 - \Delta q_2 r_2, \quad \Delta_b = \Delta q_2 r_2 - \Delta q_1 r_1, \tag{3.15}$$

where $\Delta q_1$ and $\Delta q_2$ are changes of angles of rotation for the input and the output pulleys, respectively.

As the environment is assumed to have infinite stiffness, one concludes that the motion of the output end of the mechanism can be neglected,

$$\Delta q_2 = 0. \tag{3.16}$$

Combining (3.15) and (3.16), the following relation between the elongation of the tendons and the rotation of the input pulley can be found

$$d\Delta_t = -d\Delta_b = r_1 dq_1. \tag{3.17}$$

Differentiating (3.13) with respect to $q_1$ and using (3.17), one obtains the following formula

$$\frac{d\tau_{in}}{dq_1} = r_1^2 \left( \frac{dT_{tl}}{d\Delta_t} + \frac{dT_{bl}}{d\Delta_b} \right), \tag{3.18}$$

where $\frac{dT_{tl}}{d\Delta_t}$ and $\frac{dT_{bl}}{d\Delta_b}$ are the apparent stiffnesses of the top and the bottom tendons, respectively, defined by (3.3). The apparent stiffness of a dual-tendon system $K_{app}^{Dual}$ is defined as:

$$K_{app}^{Dual} = r_1^2 \left( K_{app}^t + K_{app}^b \right), \tag{3.19}$$

Using (3.7), one can now write the following formula that describes the apparent stiffness of the dual-tendon system:

$$K_{app}^{Dual} \approx r_1^2 K_n \left( \frac{-\eta_t \, \text{sgn}(\dot{q}_1)}{e^{-\eta_t \varphi_{tw} \, \text{sgn}(\dot{q}_1)} - 1} + \frac{\eta_b \, \text{sgn}(\dot{q}_1)}{e^{\eta_b \varphi_{bw} \, \text{sgn}(\dot{q}_1)} - 1} \right), \tag{3.20}$$

where dimensionless variables $\varphi_{tw}$ and $\varphi_{bw}$ represent the ratio of active length to the whole length for the top and the bottom tendons, respectively. Also, in the above formula, $v$ is replaced by $\dot{q}_1$ as the motion of the active part of each tendon follows the rotation of the

input pulley. The natural stiffness is assumed equal for both tendons; it is denoted by $K_n$.

Finally, if both tendons are active along their whole lengths, the apparent stiffness of the dual tendon mechanism $k_{app}^{Dual-min}$ is constant and equal to

$$k_{app}^{Dual-min} = r_1^2(k_{app}^{min-pull} + k_{app}^{min-push}),\qquad(3.21)$$

where $k_{app}^{min-pull}$ is the apparent stiffness of the pulled tendon, and $k_{app}^{min-push}$ is the apparent stiffness of the pushed tendon, as defined by (3.8), (3.9).

## 3.3 Combined Stiffness of the Instrument and the Environment

Suppose a dual-tendon mechanism such as a jaw of the da Vinci instrument with apparent stiffness $K_{app}^{Dual}$ is in contact with an unknown environment with stiffness $K_{env}$. The stiffness form the point of view of the actuator $K_t$ has the following relation with the combined stiffness of environment and the instrument:

$$\frac{1}{K_t} = \frac{1}{K_{app}^{Dual}} + \frac{1}{K_{env}},\qquad(3.22)$$

where $K_t = d\tau_{in}/dq_1$ is a known value. Formula (3.22), however, is only valid if changes of input force could affect the environment, *i.e.* one or both tendons are fully active. If so, $K_{env}$ can be extracted from equation (3.22).

Figure 3.4 shows the four phases of transmission in a typical dual tendon-sheath mechanism when a sinusoidal input torque with sufficiently high amplitude and sufficiently low frequency is applied [11]. The corresponding combined stiffness in each phase is discussed below for the case where the top tendon is pulled and the bottom tendon is pushed (*i.e.* $\dot{q}_1 > 0$); in the opposite case, similar justification can be given.

**Phase I** corresponds to the situation where the change of tension has not yet propagated through the entire length of any of the tendons, so that $\varphi_{wt} < 1$ and $\varphi_{wb} < 1$. In this case, as the changes in the input torque do not yet affect the output, the stiffness of the
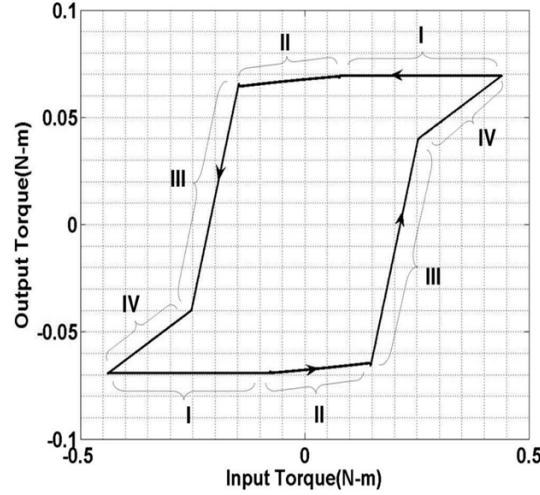
Figure 3.4: A typical input-output relation for a tendon-sheath mechanism in a pull-pull architecture [11].

environment is not reflected through the instrument, and therefore the stiffness that the actuator sees is only the apparent stiffness of the instrument:

$$\frac{1}{K_t} = \frac{1}{K_{app}^{Dual}},$$  (3.23)

where $K_{app}^{Dual}$ can be calculated using (3.20). Formula (3.20) implies that $K_{app}^{Dual}$ decreases from infinity to a minimum as $\varphi_{wt}$ and $\varphi_{wb}$ increase from 0 to 1.

**Phase II** corresponds to the situation where the change of tension has already propagated through the whole pulled tendon, but not through the pushed one. In this case, $\varphi_{wt} = 1$ and $\varphi_{wb} < 1$. In this case, the following equation is valid for the combined stiffness:

$$\frac{1}{K_t} = \left.\frac{1}{K_{app}^{Dual}}\right|_{\varphi_{wt}=1} + \frac{1}{K_{env}},$$  (3.24)

where again formula (3.20) can be used to calculate $K_{app}^{Dual}$. As the pulled tendon is fully active, the environmental stiffness is visible to the actuator. However, since the tension continues to propagate through the pushed tendon ($\varphi_{wb} < 1$), the apparent stiffness of the instrument continues to change as $\varphi_{wb}$ grows.

**Phase III** corresponds to the situation where the change of tension has propagated to the output side through both pulled and pushed tendons. In this case, $\varphi_{wt} = \varphi_{wb} = 1$. The

apparent stiffness of the instrument during this phase is constant and is in series with the stiffness of the environment, which results in the following formula:

$$\frac{1}{K_t} = \frac{1}{k_{app}^{Dual-min}} + \frac{1}{K_{env}},$$ (3.25)

where $k_{app}^{Dual-min}$ is given by (3.21).

**Phase IV** corresponds to the case where the pulled tendon is fully active, while the pushed tendon has become slack. In this case, $\varphi_{wt} = 1$ and the stiffness of the slack tendon can be assumed zero. The combined stiffness is the apparent stiffness of the pulling tendon in series with the stiffness of the environment.

$$\frac{1}{K_t} = \frac{1}{k_{app}^{min-pull}} + \frac{1}{K_{env}},$$ (3.26)

where $k_{app}^{min-pull}$ is given by (3.8).

## 3.4 Hypothesis

As explained above, as the input torque increases, the system consecutively goes through Phases I to IV. We hypothesize that, by applying a monotonically increasing or decreasing input torque, one can reach to Phase III (or Phase IV) of transmission, in which the environmental stiffness can be extracted from the measured combined stiffness using the formula (3.25) (or (3.26)). In this manner, the stiffness of different tissue samples can be compared. This hypothesis is experimentally validated in the subsequent sections.

## 3.5 The Experimental Setup

In order to investigate the hypothesis stated above, experiments have been conducted using an EndoWrist®grasper mounted on an actuator set, as described in [8]. The experimental setup is shown in Figure 3.5. The EndoWrist®grasper, shown in Figure 3.6, is a robotic laparoscopic tool designed for the da Vinci RAMIS system. It is designed such that four sets of tendon-pulley mechanisms facilitate the four degrees of freedom of the tip [12].
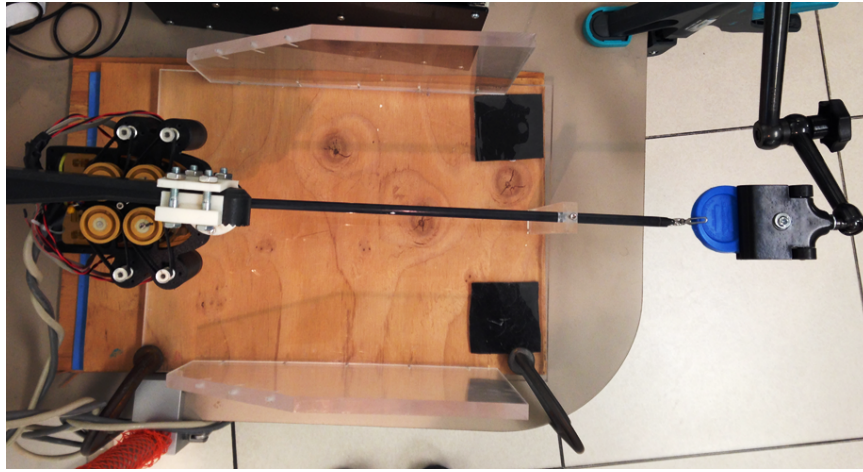
Figure 3.5: The experimental setup.



Figure 3.6: A close look of the tip of da Vinci EndoWrist®grasper [13].

The actuator set consists of four Faulhaber DC motors with encoders, tightly arranged to match the input pulleys of the instrument. At the distal side, the tip of the instrument is set in straight configuration to grip artificial tissues held by a vice, as shown in Figure 3.5. The gripping DOF of the instrument, which includes two tendon-pulley mechanisms, is used in this study.

Figure 3.7: The silicone samples used in the first experiment.

## 3.6 Results and Discussion

Two sets of experiments were conducted in order to demonstrate the possibility of using the dual tendon-pulley instrument for the environmental stiffness estimation. In the first set of experiments, the EndoWrist® grasper was used to discriminate between sample tissues based on their compliances. In the second set of experiments, the capability of the instrument for finding tumour-like elements in an artificial soft tissue was studied. In both experiments, triangular torque signals were sent to the actuators of the grasping jaws. Since the gripping DOF of the instrument includes two tendon-pulley mechanisms, the combined stiffness formula of (3.22) has to be modified as follows,

$$K_t = \frac{d\tau_{in}}{d(q_1^{J1} - q_1^{J2})},$$ 
(3.27)

where $q_1^{J1}$ is the rotation of the input pulley of the upper jaw and $q_1^{J2}$ is the rotation of the input pulley of the lower jaw.

### 3.6.1 First Set of Experiments

The aim of the first set of experiments was to determine if the above described method allows for detection of changes of the environmental stiffness. A set of compliant, semi-compliant and rigid silicone samples (Ecoflex® 00-20, Mold Star® 16, Crystal Clear® Series) is studied in this experiment (Figure 3.7). The samples were palpated by the EndoWrist® grasper and subsequently ranked in terms of their stiffnesses using the method described above.
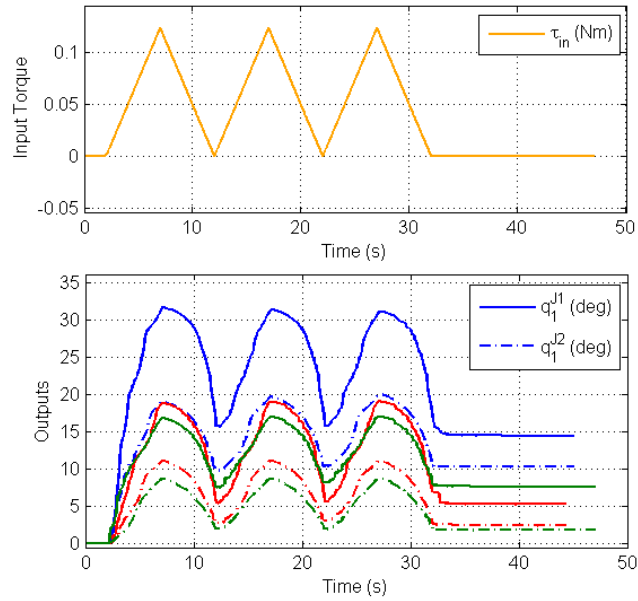
Figure 3.8: First set of experiments: the input torque (top); the resulting rotation of the input pulley (bottom). Blue, red, and green curves correspond to compliant, semi-compliant, and rigid samples, respectively.

Figure 3.8 represents the applied torque and the measured rotation of the input pulleys of the palpating experiments. The colours blue, red and green represent the case of compliant, semi-compliant and rigid samples, respectively. The resulting combined stiffness, which is found from (3.27), is illustrated in Figure 3.9 (top). As expected, in all cases, the combined stiffness curves go from large values during phases 1 and 2 to approximately constant values. It is much more convenient, however, to represent the stiffness of interaction in the form of combined compliance. The combined compliance curves are shown in Figure 3.9 (bottom). In this figure, the difference in combined compliance can be clearly seen during the intervals of time when the input torque is sufficiently high. The difference in compliance, however, is more identifiable when the sample is being released, in contrast with the time when it is being pressed. This is probably because the samples do not exhibit linear stiffness characteristics when squeezed.
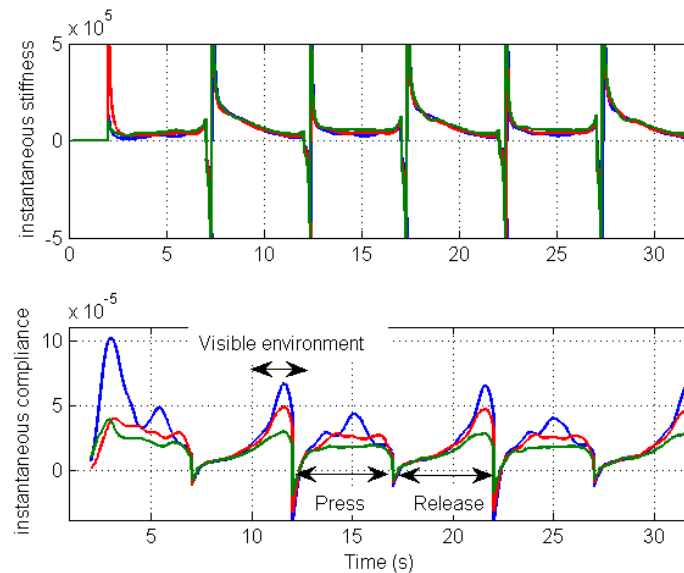
Figure 3.9: Experimental results: combined stiffness of the samples during palpation (top); combined compliance of the samples during palpation (bottom).

## 3.6.2   Second Set of Experiments

In the second set of experiments, the instrument was used to find the location of a tumour-like substance in an artificial tissue. A silicone-made artificial tissue was used which includes two strips of a harder material which emulate tumours (Figure 3.10). The EndoWrist® grasper was used for palpating the tissue from one end to the other. The same input signal as in the first experiment was applied to the input pulleys of the grasping DOFs to palpate the areas shown in Figure 3.12 (top). Figure 3.11 shows the combined compliance of the



Figure 3.10: The artificial tissue with tumors implemented at different depth
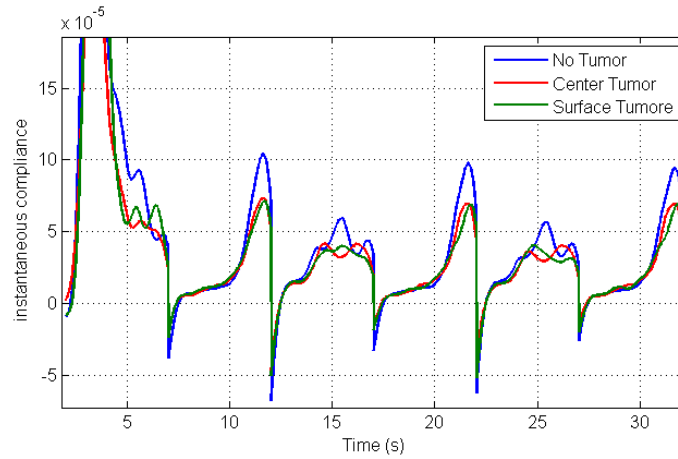
Figure 3.11: Experimental results: combined compliance of the system when palpating different areas of the artificial tissue.

system when grasping different areas of the tissue. Here the colors blue, red and green stand for tissue without a tumour, tissue with a tumour at the center, and the tissue with a tumour at the surface, respectively. As can be seen from this figure, the combined compliance of the parts of the tissue with tumours in it is visibly lower in comparison with the empty tissue.

By averaging the combined compliance in the last two seconds of each cycle of releasing, a compliance distribution map can be formed as shown in Figure 3.12 (bottom). The map clearly shows the location of the tumours in the tissue. The experiment verifies that the suggested method is feasible for localizing tumours regardless of their depth in the tissue.

## 3.7    Conclusion

Determining mechanical properties of the environment using cable-driven laparoscopic instruments such as those of the da Vinci surgical robotic system is a difficult task because of the highly nonlinear behavior of the instrument and the technical complexities associated with mounting sensors. This Chapter described a method for estimation of the compliance of the environment which is based on analysis of the behavior of a dual tendon-sheath system. The derived model suggests that, if a sufficiently large input torque is applied, the stiffness of the environment becomes detectable at the actuator. The method for extraction
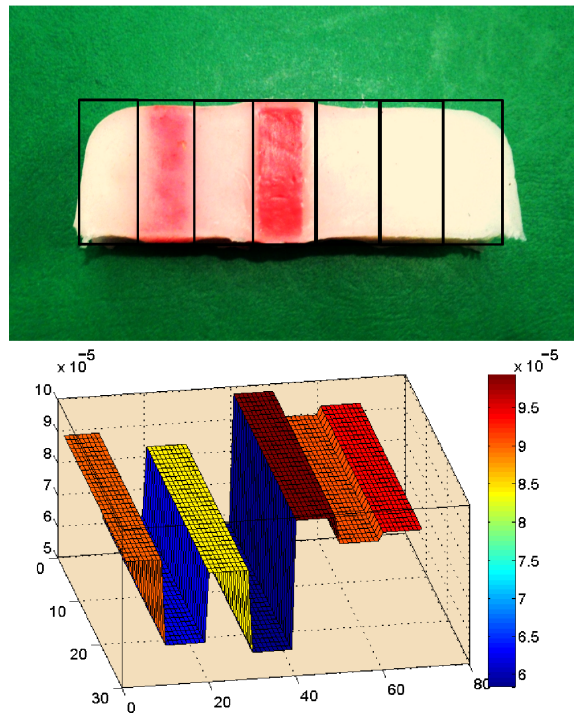
Figure 3.12: The artificial tissue with palpation regions (top); the corresponding distribution of combined compliances (bottom).

of environmental compliance data from combined stiffness was tested in two preliminary experiments, one using silicone samples and the other using artificial tissue with tumours. The feasibility of determining the relative stiffness of these samples using the proposed method was demonstrated. Further work is required to obtain a quantitative assessment of the stiffness estimation that can be achieved using this approach. Work is in progress in this context with the goal of determining the accuracy with which tumour localization can be performed. To this end, an extensive study will be conducted using the dVRK (da Vinci Research Kit) [14] and the da Vinci RAMIS system available at CSTAR.

# References

[1] O. A. J. V. der Meijden and M. P. Schijven, "The value of haptic feedback in conventional and robot-assisted minimal invasive surgery and virtual reality training: a current review," *Surgical endoscopy*, vol. 23, no. 6, pp. 1180–1190, 2009.

[2] G. T. Sung and I. S. Gill, "Robotic laparoscopic surgery: a comparison of the da Vinci and Zeus systems," *Urology*, vol. 58, no. 6, pp. 893–898, 2001.

[3] P. Culmer, J. Barrie, R. Hewsonand, M. Levesley, M. Mon-Williams, D. Jayne, and A. Neville, "Reviewing the technological challenges associated with the development of a laparoscopic palpation device," *The International Journal of Medical Robotics and Computer Assisted Surgery*, vol. 8, no. 2, pp. 146–159, 2012.

[4] M. V. Ottermo, O. Stavdahl, and T. A. Johansen, "Palpation instrument for augmented minimally invasive surgery," in *IEEE/RSJ International Conference on Intelligent Robots and Systems (IROS)*, pp. 3960–3964, 2004.

[5] S. Perreault, A. Talasaz, A. L. Trejos, C. D. Ward, R. V. Patel, and B. Kiaii, "A 7-dof haptics-enabled teleoperated robotic system: Kinematic modeling and experimental verification," in *3rd IEEE RAS & EMBS International Conference on Biomedical Robotics and Biomechatronics*, (Tokyo, Japan), pp. 906–911, IEEE, 2010.

[6] S. Schostek, C. N. Ho, D. Kalanovic, and M. O. Schurr, "Artificial tactile sensing in minimally invasive surgery - a new technical approach," *Minimally Invasive Therapy and Allied Technologies*, vol. 15, no. 5, pp. 296–304, 2006.

[7] M. T. Perri, A. L. Trejos, M. D. Naish, R. V. Patel, and R. A. Malthaner, "New tactile sensing system for minimally invasive surgical tumour localization," *The International Journal of Medical Robotics and Computer Assisted Surgery*, vol. 6, no. 2, pp. 211–220, 2010.

[8] F. Anooshahpour, I. G. Polushin, and R. V. Patel, "Quasi-static modeling of the da Vinci instrument," in *IEEE/RSJ International Conference on Intelligent Robots and Systems (IROS)*, pp. 1308–1313, IEEE, 2014.

[9] M. Kaneko, M. Wada, H. Maekawa, and K. Tanie, "A new consideration on tendon-tension control system of robot hands," in *IEEE International Conference on Robotics and Automation (ICRA)*, pp. 1028–1033, IEEE, 1991.

[10] M. Kaneko, T. Yamashita, and K. Tanie, "Basic considerations on transmission characteristics for tendon drive robots," in *IEEE Fifth International Conference on Advanced Robotics (ICAR),'Robots in Unstructured Environments'*, pp. 827–832, IEEE, 1991.

[11] V. Agrawal, W. J. Peine, and B. Yao, "Modeling of transmission characteristics across a cable-conduit system," *IEEE Transactions on Robotics*, vol. 26, no. 5, pp. 914–924, 2010.

[12] G. Guthart and J. K. Salisbury, "The Intuitive™ telesurgery system: overview and application," in *IEEE International Conference on Robotics and Automation*, pp. 618–621, IEEE, 2000.

[13] Intuitive Surgical, Inc., *EndoWrist: Instrument and Accessory Catalog*, July 2011.

[14] P. Kazanzidesf, Z. Chen, A. Deguet, G. S. Fischer, R. H. Taylor, and S. P. DiMaio, "An open-source research kit for the da Vinci® surgical system," in *2014 IEEE International Conference on Robotics and Automation (ICRA)*, pp. 6434–6439, IEEE, 2014.

# Chapter 4

# Classical Preisach Model of Hysteretic Behavior in a da Vinci® Instrument

**T**endon-based instruments are widely used in both robotic and manual minimally invasive surgical procedures. Direct measurement of the interaction forces at the tip of such instruments is difficult. As a result, methods for estimation of these forces are of substantial interest. In this chapter, modeling of the input-output hysteretic behavior in a da Vinci instrument is addressed using the classical Preisach approach. The performance of the developed model is experimentally evaluated. The results obtained demonstrate that the classical Preisach model allows for sufficiently precise estimation of the forces at the tip of the da Vinci instrument.

## 4.1 Introduction

In recent years, substantial advancements in Minimally Invasive Surgery (MIS) have been achieved through incorporation of robotic technologies. Robot-Assisted Minimally Invasive Surgery (RAMIS) can potentially solve some of the most significant problems associated with MIS, including restricted view of the operative field, difficulty in achieving precise control of the laparoscopic instruments, and limited sense of touch. At the

---

The material presented in this chapter is published in the proceeding of "IEEE International Conference on Advanced Intelligent Mechatronics (AIM), Banff, AB, pp. 1392-1397.IEEE, 2016"

Figure 4.1: EndoWrist™ instruments by Intuitive Surgical [4]

present time, however, commercially available RAMIS systems do not provide haptic feedback [1, 2]. Some of the difficulties associated with haptic feedback are related to the fact that, typically, RAMIS instruments have miniature tips (see Figure 4.1), which makes it challenging to install force sensors. Also, RAMIS instruments must undergo sterilization in the harsh environment of autoclave chambers, and must be disposed of after a few uses due to safety considerations. Force sensors, on the other hand, are generally sensitive to harsh environments and usually too expensive to be decommissioned after a few uses. A possible alternative solution for restoration of the tool-tissue interaction forces at the tip of a RAMIS instrument consists of designing an observer which generates an estimate of these forces based on the measurements of torques and/or motions at the actuator end of the instrument. Implementation of such an observer would, however, require an appropriate and sufficiently precise mathematical model of the instrument. A particular group of RAMIS instruments on which our research is focused are the EndoWrist™ instruments designed for the da Vinci surgical system [3]. These instruments utilize a compact set of tendon-pulley mechanisms placed inside a narrow shaft, which transmit the power from the actuators to the tip of the instrument. In particular, the input-output behavior of these instruments is characterized by pronounced hysteresis effect which comes from the compliance of the tendons as well as distributed friction between the tendons and their surroundings inside the instrument.

In their previous work [5, 6], the authors developed an approach to quasi-static modelling of such tendon-pulley mechanisms. The approach of [5, 6] is based on a first-principles model that describes mechanical behavior of a pair of tendons sliding on curved surfaces. As a result, a set of equations is obtained which relates the input motion/torque with the

output torque in quasi-static conditions. The relationship depends on a number of parameters as well as the initial tension distribution, all of which are typically unknown and have to be identified. In this work, however, we explore a completely different set of ideas; specifically, we aim at development of a purely phenomenological model of input-output behavior of a tendon-pulley force transmission system which is based on the classical Preisach model of hysteresis [7].

In the literature, a number of studies have been reported that address phenomenological modeling of tendon-based force/power transmission systems. In [8], a piecewise linear model that describes the backlash-like behavior of a dual tendon-sheath mechanism is proposed, and a controller is subsequently designed based on the smooth inverse model of the backlash. In [9], a modified Bouc-Wen model and a Coleman-Hodgdon model were proposed for single and dual tendon-sheath mechanisms. In [10], a formula for estimating the width of the backlash in a pretension-free single tendon-sheath mechanism is suggested, which relates geometrical features of the sheath and tendon, such as radius of curvature, bending angle, and the gap between sheath and tendon, to the width of hysteresis. However, none of these works addressed specifically a da Vinci instrument or a closely similar mechanism. Also, to the best of authors' knowledge, applicability of the classical Preisach hysteresis modeling to tendon-sheath and/or tendon-pulley mechanisms has not been addressed previously.

The objective of this work is to develop a phenomenological model that describes input-output behavior of a da Vinci instrument using the classical Preisach approach to hysteresis modeling. Developed originally as a mathematical model for magnetization processes, the Preisach hysteresis model has found numerous applications in many areas of science and engineering, including ferromagnetism, piezoceramic actuators, and smart materials [7, 11]. Our choice of the Preisach model was motivated by the fact that our preliminary experiments indicated that the input-output characteristics of the da Vinci instrument satisfy two particular properties, specifically the *wiping-out* and the *congruency* properties. According to [7], these two properties are necessary and sufficient for a hysteresis mechanism to be represented by the classical Preisach model. We demonstrate that application of the Preisach approach to modelling of a da Vinci instrument allows for fairly close prediction of the forces at the tip of the instrument.
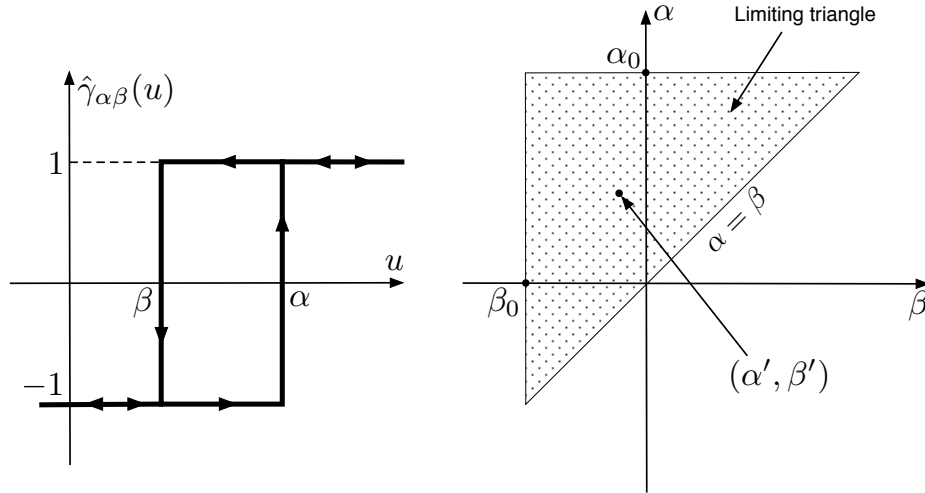
Figure 4.2: Relay operator $\hat{\gamma}_{\alpha\beta}(\cdot)$, $\alpha, \beta \in \mathbb{R}$ (left). Each point $(\alpha', \beta')$ of the triangular subset $\{(\alpha, \beta) \in \mathcal{R}^2, \alpha \geq \beta, \alpha \leq \alpha_0, \beta \geq \beta_0\}$ corresponds to a single relay operator $\hat{\gamma}_{\alpha'\beta'}$ together with its scaling factor $\mu(\alpha', \beta')$ (right).

The chapter is organized as follows. In Section 4.2, fundamentals of the Preisach hysteresis model are explained. In Section 4.3, an algorithm for real-time calculation of the polygonal interface in Preisach hysteresis model is presented; the algorithm is subsequently used in our experimental investigation. The experimental setup is described in Section 4.4. In Section 4.5, classical Preisach model of the da Vinci instrument is identified, and performance of the developed model in estimating the output force is evaluated. Conclusions are given in Section 4.6.

## 4.2 Classical Preisach Model of Hysteresis

In this section, a brief summary of the classical Preisach hysteresis model is given based on the general theory presented in [7, 12]. The core building block of Preisach hysteresis model is the relay operator $\hat{\gamma}_{\alpha\beta}(\cdot)$, where $\alpha, \beta \in \mathbb{R}$, $\alpha \geq \beta$, which is illustrated in Figure 4.2 (left). The output of the relay operator switches between 1 and $-1$ according to the following rules. If the input $u(t)$ is greater than the upper threshold $\alpha$ ($u(t) > \alpha$), the output $\hat{\gamma}_{\alpha\beta}(u(t))$ is equal to 1; if the input $u(t)$ is smaller than the lower threshold $\beta$ ($u(t) < \beta$), the output $\hat{\gamma}_{\alpha\beta}(u(t))$ is equal to $-1$. If $\beta \leq u(t) \leq \alpha$, the output depends on the history of the input; specifically, it depends on direction from which the input $u(t)$ has

approached the relay loop. Informally, if the input $u < \beta$ immediately before it entered the relay loop, then $\hat{\gamma}_{\alpha\beta}(u(t)) = -1$; similarly, $\hat{\gamma}_{\alpha\beta}(u(t)) = 1$ if $u > \alpha$ immediately before it entered the relay loop. [1]

The classical Preisach model describes hysteretic behavior using a superposition of an infinite number of the above described relay operators $\hat{\gamma}_{\alpha\beta}(\cdot)$ scaled using a weighting function $\mu(\alpha, \beta) \geq 0$. Both the relay operators $\hat{\gamma}_{\alpha\beta}(\cdot)$ and the weighting function $\mu(\alpha, \beta) \geq 0$ are defined on a compact subset of a half-plane $\{(\alpha, \beta) \in \mathcal{R}^2, \alpha \geq \beta\}$. This is illustrated in Figure 4.2 (right), where each point $(\alpha', \beta')$ of a triangular subset of the half-plane $\{(\alpha, \beta) \in \mathcal{R}^2, \alpha \geq \beta\}$ can be mapped to a specific relay operator $\hat{\gamma}_{\alpha'\beta'}$ and its weighting coefficient $\mu(\alpha', \beta')$. The overall formula that describes the classical Preisach hysteresis model has a form

$$f(t) = \iint\limits_{\alpha \geq \beta} \hat{\gamma}_{\alpha\beta}(u(t)) \, \mu(\alpha, \beta) \, d\alpha \, d\beta. \tag{4.1}$$

The behavior of the classical Preisach model can be understood using geometric considerations, as follows. Consider a triangular subset of a half-plane $\{(\alpha, \beta) \in \mathcal{R}^2, \alpha \geq \beta\}$ satisfying $\alpha \leq \alpha_0$, $\beta \geq \beta_0$ with some bounds $\alpha_0 > \beta_0$, see Figure 4.2 (right). Each point $(\alpha, \beta)$ of this triangle corresponds to a relay operator $\hat{\gamma}_{\alpha\beta}(\cdot)$, while the bounds $\alpha_0$ and $\beta_0$ represent the largest upper threshold and the smallest lower threshold, respectively, of all relay operators. If the input signal $u \geq \alpha_0$, then all relay operators are switched positive ($\hat{\gamma}_{\alpha\beta}(u) = +1$ for all $\alpha, \beta$), which results in that the overall output $f$ is equal to its upper saturation limit $f^+$. Similarly, if the input signal $u \leq \beta_0$, then all relay operators are switched negative ($\hat{\gamma}_{\alpha\beta}(u) = -1$ for all $\alpha, \beta$), and the overall output $f$ is equal to its lower saturation limit $f^-$. If $\beta_0 < u(t) < \alpha_0$, then some of the relay operators are switched negative, while the rest are switched positive. Specifically, increasing the value of input $u(t)$ to some value $\alpha_1$ ($\beta_0 \leq \alpha_1 \leq \alpha_0$) switches all relay operators $\hat{\gamma}_{\alpha\beta}(\cdot)$ with $\alpha \leq \alpha_1$ positive, while decreasing $u(t)$ to some $\beta_1$ ($\beta_0 \leq \beta_1 \leq \alpha_0$) results in all relay operators $\hat{\gamma}_{\alpha\beta}(\cdot)$ with $\beta \geq \beta_1$ switched negative. The result of an increase of the input $u(t)$ from an initial value below $\beta_0$ to $\alpha_1$ and its subsequent decrease to $\beta_1$ is illustrated in Figure 4.3, where the polygonal line $L(t)$ represents the border between the set $S^+$ of relay operators

---

[1]Mathematically, assuming $u(t)$ is continuous, one can denote $t_\alpha(t) := \sup\{\tau < t : u(\tau) > \alpha\}$, and $t_\beta(t) := \sup\{\tau < t : u(\tau) < \beta\}$, where $\sup(\emptyset) = -\infty$. Then, $\hat{\gamma}_{\alpha\beta}(u(t)) := 1$ if $t_\alpha > t_\beta$, and $\hat{\gamma}_{\alpha\beta}(u(t)) := -1$ otherwise.
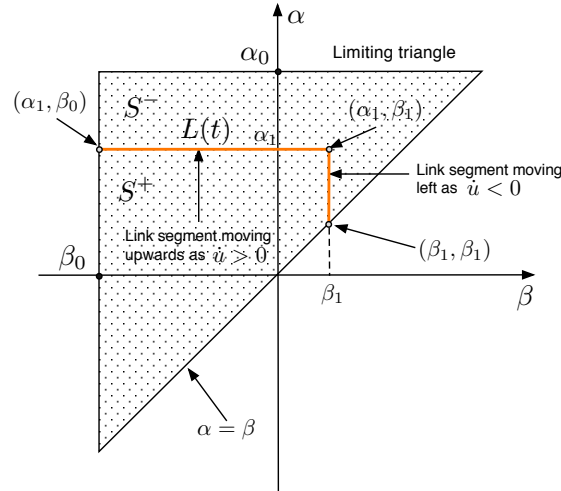
Figure 4.3: The interface $L(t)$ which results from increasing the input from $u(t_0) < \beta_0$ to $u(t_1) = \alpha_1$, and its subsequent decrease to $u(t_2) = \beta_1$.

switched positive and the set $S^-$ of relay operators switched negative. Further decrease of the input $u(t)$ would result in the last (*i.e.*, attached to the line $\alpha = \beta$) link of $L(t)$ moving left, while increasing the input $u(t)$ would result in emergence of a new horizontal link which moves up as input increases.

Taking into account that $\hat{\gamma}_{\alpha\beta}(u(t)) = +1$ for $(\alpha, \beta) \in S^+(t)$ and $\hat{\gamma}_{\alpha\beta}(u(t)) = -1$ for $(\alpha, \beta) \in S^-(t)$, formula (4.1) can be rewritten as follows,

$$f(t) = \int\int_{S^+(t)} \mu(\alpha, \beta) d\alpha d\beta - \int\int_{S^-(t)} \mu(\alpha, \beta) d\alpha d\beta. \tag{4.2}$$

Formula (4.2), in particular, indicates that the instantaneous value of output $f(t)$ depends upon the shape of interface $L(t)$ (*i.e.*, the polygonal line that separates $S^+$ and $S^-$), which in turn is defined by the history of the extremum values of the input signal $u(t)$.

The weighting function $\mu(\alpha, \beta)$ can in principle be identified using the following procedure. Given $\alpha, \beta$ such that $\beta_0 \le \beta \le \alpha \le \alpha_0$, consider an input trajectory $u(t)$ which starts from an initial value $u(t_0) < \beta_0$, increases monotonically to $u(t_1) = \alpha$, and subsequently decreases monotonically to $u(t_2) = \beta$, $t_0 \le t_1 \le t_2$. In response to such an input trajectory, the output $f(t)$ traces a so-called first-order transition (reversal) curve [7]. The final value of $f(t)$ at the end of this curve is denoted by $f_{\alpha\beta}$, *i.e.*, $f_{\alpha\beta} := f(t_2)$. Using such a procedure, the values of $f_{\alpha\beta}$ can in principle be experimentally obtained for all $\alpha, \beta$ satis-

fying $\beta_0 \leq \beta \leq \alpha \leq \alpha_0$ (in practice, $f_{\alpha\beta}$ can be obtained experimentally for some finite set of spatially distributed sample points $(\alpha, \beta)$, and subsequently estimated in between these points using some sort of interpolation procedure, as discussed below in Section 4.5.1). The weighting function $\mu(\alpha, \beta)$ can then be calculated according to the formula [7]:

$$\mu(\alpha, \beta) = \frac{1}{2} \cdot \frac{\partial^2 f_{\alpha\beta}}{\partial\alpha\,\partial\beta}. \tag{4.3}$$

In practice, direct implementation of the Preisach model according to formulas (4.1) (or (4.2)) and (4.3) may be difficult because of two reasons. First, real-time implementation of double integration in (4.1) may require substantial computational resources. Second, formula (4.3) requires double differentiation of an experimentally obtained function $f_{\alpha\beta}$, which may greatly amplify the noise inherently present in the experimental data. In order to avoid these pitfalls, one can use an alternative set of formulas that represents the response of Preisach model directly in terms of $f_{\alpha\beta}$ and the polygonal line $L(t)$. Specifically, it was shown in [7] that formulas (4.1) (or (4.2)) and (4.3) are equivalent to the following:

$$f(t) = -f^+ + \sum_{k=1}^{n(t)-1} (f_{\alpha_k\beta_k} - f_{\alpha_k\beta_{k-1}}) + f^*(t), \tag{4.4}$$

where

$$f^*(t) = \begin{cases} f_{\alpha_n u(t)} - f_{\alpha_n\beta_{n-1}} & \text{whenever } \dot{u}(t) < 0, \\ f_{u(t)u(t)} - f_{u(t)\beta_{n-1}} & \text{whenever } \dot{u}(t) > 0. \end{cases} \tag{4.5}$$

In the above formulas (4.4), (4.5), $f^+$ is the upper saturation limit of the output $f$, $n(t)$ is the number of horizontal segments of the polygonal line $L(t)$, and $\alpha_k$, $\beta_k$ are coordinates of the corresponding vertices of $L(t)$ (see Figure 4.4). Formulas (4.4), (4.5) will be used for numerical implementation of the Preisach model in our work.

## 4.3  Algorithm for Real-Time Calculation of $L(t)$

The response of Preisach model (4.2) (or, equivalently, (4.4), (4.5)) depends upon the exact form of the polygonal line $L(t)$ which represents the interface between sets $S^+$ and $S^-$. For our experiments, an algorithm for real-time calculations of $L(t)$ was developed which
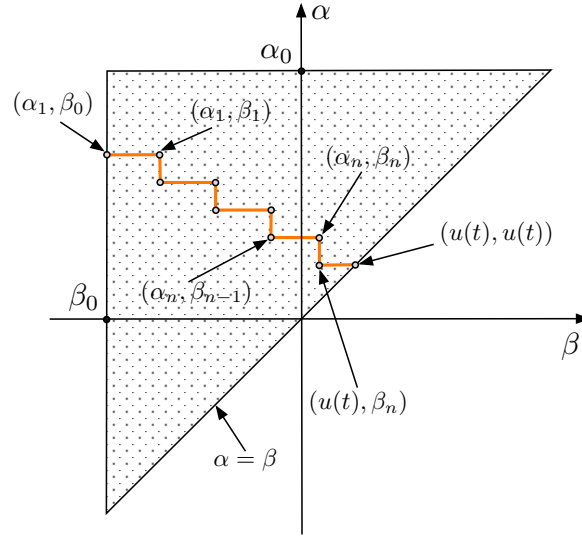
Figure 4.4: Notation for coordinates of vertices of $L(t)$.

is described as follows. At any given instant of time $t$, the interface $L(t)$ is represented by a matrix $\hat{L}(t)$ of the form

$$\hat{L}(t) = \begin{bmatrix} \alpha_1 & \alpha_1 & \alpha_2 & \cdots & \alpha_n & u(t) & u(t) \\ \beta_0 & \beta_1 & \beta_1 & \cdots & \beta_n & \beta_n & u(t) \end{bmatrix} \tag{4.6}$$

whenever $\dot{u}(t) > 0$, and/or of the form

$$\hat{L}(t) = \begin{bmatrix} \alpha_1 & \alpha_1 & \alpha_2 & \cdots & \alpha_n & \alpha_n & u(t) \\ \beta_0 & \beta_1 & \beta_1 & \cdots & \beta_{n-1} & u(t) & u(t) \end{bmatrix} \tag{4.7}$$

whenever $\dot{u}(t) < 0$. Each column of $\hat{L}(t)$ consists of $(\alpha, \beta)$ coordinates of the vertices of the polygonal line $L(t)$; thus, matrix $\hat{L}$ completely describes the geometry of the interface $L(t)$. The developed algorithm for real-time calculations of $\hat{L}(t)$ consists of the following steps.

**Step 1. Initialization:** The value of $\hat{L}(0)$, generally speaking, depends on the initial value of the input $u(0)$ as well as on the sign of $\dot{u}(0)$. In our experiments, the initial value of the input signal is always equal to its lower saturation limit ($u(0) = \beta_0 = -5V$), which

implies that

$$\hat{L}(t) = \begin{bmatrix} u(t) & u(t) \\ \beta_0 & u(t) \end{bmatrix} \tag{4.8}$$

is valid for $t = 0$ as well as for sufficiently small $t > 0$.

**Step 2. Adding vertices:** A new vertex is added to $L(t)$ (which, in particular, corresponds to adding a new column to $\hat{L}(t)$) whenever the derivative of input changes its sign. Specifically, the following two rules are to be executed:

- *Adding vertices, Rule 1:* If at $t = t_0$ the input derivative changes sign from negative to positive (strictly speaking, if there exist $\epsilon_1, \epsilon_2 > 0$ such that $\dot{u}(t) \leq 0$ for $t \in (t_0 - \epsilon_1, t_0)$, $\inf_{t \in (t_0 - \epsilon_1, t_0)} \dot{u}(t) < 0$, and $\dot{u}(t) > 0$ for $t \in (t_0, t_0 + \epsilon_2)$), then $L(t)$ changes as follows:

$$\hat{L}(t) = \begin{bmatrix} \alpha_1 & \alpha_1 & \cdots & \alpha_n & u(t) \\ \beta_0 & \beta_1 & \cdots & u(t) & u(t) \end{bmatrix} \quad \text{for } t \in (t_0 - \epsilon_1, t_0]$$

$$\Downarrow \ t = t_0$$

$$\hat{L}(t) = \begin{bmatrix} \alpha_1 & \alpha_1 & \cdots & \alpha_n & u(t) & u(t) \\ \beta_0 & \beta_1 & \cdots & \beta_n := u(t_0) & \beta_n := u(t_0) & u(t) \end{bmatrix}.$$

- *Adding vertices, Rule 2:* If at $t = t_0$ the input derivative changes sign from positive to negative (strictly speaking, if there exist $\epsilon_1, \epsilon_2 > 0$ such that $\dot{u}(t) \geq 0$ for $t \in (t_0 - \epsilon_1, t_0)$, $\sup_{t \in (t_0 - \epsilon_1, t_0)} \dot{u}(t) > 0$, and $\dot{u}(t) < 0$ for $t \in (t_0, t_0 + \epsilon_2)$), then $L(t)$ changes as follows:

$$\hat{L}(t) = \begin{bmatrix} \alpha_1 & \alpha_1 & \cdots & u(t) & u(t) \\ \beta_0 & \beta_1 & \cdots & \beta_{n-1} & u(t) \end{bmatrix} \quad \text{for } t \in (t_0 - \epsilon_1, t_0]$$

$$\Downarrow \ t = t_0$$

$$\hat{L}(t) = \begin{bmatrix} \alpha_1 & \alpha_1 & \cdots & \alpha_n := u(t_0) & \alpha_n := u(t_0) & u(t) \\ \beta_0 & \beta_1 & \cdots & \beta_{n-1} & u(t) & u(t) \end{bmatrix}.$$

**Step 3. Deleting vertices:** Vertices are deleted from $L(t)$ (equivalently, a number of columns of $\hat{L}(t)$ decreases) whenever the value of input equals either $\alpha_n$ or $\beta_{n-1}$. This

represents the so-called *wipe-out* property of the Preisach model [7]. Specific rules are as follows:

- *Deleting vertices, Rule 1:* If $u(t_0) = \alpha_n$ at some instant $t_0$, then $L(t)$ changes as follows:

$$\hat{L}(t) = \begin{bmatrix} \alpha_1 & \alpha_1 & \cdots & \alpha_n & \alpha_n & u(t) & u(t) \\ \beta_0 & \beta_1 & \cdots & \beta_{n-1} & \beta_n & \beta_n & u(t) \end{bmatrix}$$

$$\Downarrow \ t = t_0$$

$$\hat{L}(t) = \begin{bmatrix} \alpha_1 & \alpha_1 & \cdots & u(t) & u(t) \\ \beta_0 & \beta_1 & \cdots & \beta_{n-1} & u(t) \end{bmatrix}.$$

- *Deleting vertices, Rule 2:* If $u(t_0) = \beta_{n-1}$ at some instant $t_0$, then the following changes are applied to $L(t)$:

$$\hat{L}(t) = \begin{bmatrix} \alpha_1 & \alpha_1 & \cdots & \alpha_{n-1} & \alpha_n & \alpha_n & u(t) \\ \beta_0 & \beta_1 & \cdots & \beta_{n-1} & \beta_{n-1} & u(t) & u(t) \end{bmatrix}$$

$$\Downarrow \ t = t_0$$

$$\hat{L}(t) = \begin{bmatrix} \alpha_1 & \alpha_1 & \cdots & \alpha_{n-1} & u(t) \\ \beta_0 & \beta_1 & \cdots & u(t) & u(t) \end{bmatrix}.$$

The above described algorithm is used in our experiments for real-time calculation of the interface $L(t)$. An example of the algorithm's performance is shown in Figure 4.5, where a sample input signal is shown together with the resulting interface $L(t)$ which was generated by the above described algorithm.

## 4.4 Experimental Setup

In order to evaluate the applicability of the classical Preisach approach to modeling of the input-output behavior in da Vinci instruments, an experimental setup was assembled as shown in Figure 4.6. The setup is similar to the one used in [5], where it is described in detail. An EndoWrist™ forceps is chosen for this study. The force transmission system
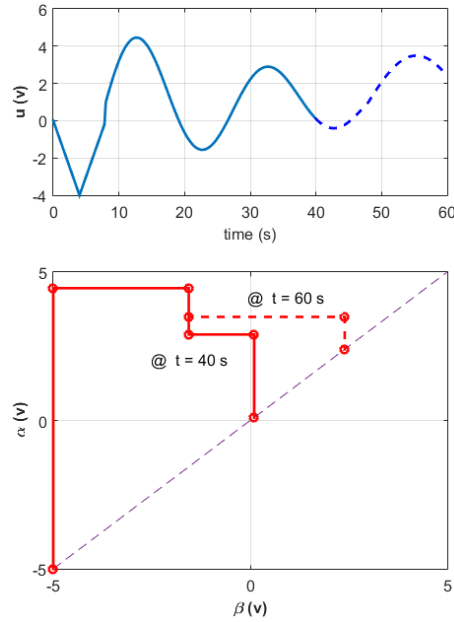
Figure 4.5: A sample input signal (top); the resulting interface $L(t)$ for $t = 40$ s and $t = 60$ s (bottom).

inside the instrument consists of four tendon-pulley mechanisms, tightly packed inside a casing and a narrow tube. Each tendon-pulley mechanism transfers forces to one of the four DOF of the distal tip, these include a pitch, a roll, and two griping DOFs, although there is notable coupling between these DOFs. The input side of the instrument is fixed in an actuator set, which consists of four Faulhaber® 2642W024CR Coreless DC Motors equipped with Faulhaber® Magnetic Encoders Model R IE2-512 that provide 2048 counts per revolution. The motors' drivers are set to current mode; as a result, the torques applied to the instrument by the motors are approximately proportional to the voltage commands generated by the IO card. During the experiments, one of the jaws of the EndoWrist™ forceps is fixed to an ATI Nano 17 force sensor as shown in Figure 4.6 (bottom); the sensor has a force resolution of 1/160 N (calibration SI-25-0.25) in all directions, with maximum sensing range of $\pm 25$ N in the directions of the $x$ and $y$ axes, and $\pm 35$ N along the $z$-axis. The force measurements are captured by a National Instrument PCI 6220 data acquisition card. For the purposes of modelling, the force $F_x$ is considered to be the output of the system, while the voltage across the corresponding Faulhaber DC motor is the input. Other components of the output force (such as $F_z$) appear to be relatively minor, and are neglected in this study.

Figure 4.6: The experimental setup: the overall view (top); close-up of the instrument tip fixed to a force sensor (bottom).

## 4.5  Experimental Results

### 4.5.1  Model Identification

The experimental investigation begins with identification of the Preisach model that describes the da Vinci instrument. To this end, a discretized set of first-order transition curves was generated which covers the range of input signals $-5V \leq u \leq 5V$ with resolution $\Delta \alpha = \Delta \beta = 1V$. The maximal ($\alpha_0 = 5V$) and the minimal ($\beta_0 = -5V$) values of the input range were chosen experimentally such that the resulting output torque achieves its upper and lower saturation limits, respectively. The input signal used during the identification procedure is shown in Figure 4.7 (top). As can be seen, the first cycle of the input signal begins with value $u = \beta_0 = -5V$, which slowly increases to $u = \alpha_0 = +5V$, and then slowly decreases back to $u = -5V$. While decreasing, the output force $F_x$ is sampled once per 1V drop of input. As a result of the first cycle, a set of values $f_{\alpha\beta}$, $\alpha = 5V$, $\beta \in \{-5V, -4V, \ldots, 4V, 5V\}$ is obtained. During second cycle, the input again starts from $u = \beta_0 = -5V$, increases to $u = \alpha_0 - \Delta\alpha = +4V$, and then decreases to $u = \beta_0 = -5V$ while being sampled once per 1V drop; as a result, a set $f_{\alpha\beta}$, $\alpha = 4V$, $\beta \in \{-5V, -4V, \ldots, 4V, 5V\}$ is obtained, *etc.*. The resulting first-order transition (reversal) curves are shown in Figure 4.7 (bottom), while the mesh of obtained values of $f_{\alpha\beta}$ is graphically illustrated in Figure 4.8.

An extension of $f_{\alpha\beta}$ to the continuous range $(\alpha, \beta) := \{-5V \leq \beta \leq \alpha \leq 5V\}$ is obtained using an interpolation procedure described in [7, Section 1.4], as follows. Consider a mech of points that covers the limiting triangle $(\alpha, \beta) := \{\beta_0 \leq \beta \leq \alpha \leq \alpha_0\}$. For each point inside a rectangular cell (*i.e.*, a cell with vertices $(\alpha_i, \beta_i)$, $(\alpha_{i-1}, \beta_i)$, $(\alpha_i, \beta_{i-1})$, and $(\alpha_{i-1}, \beta_{i-1})$), the value of $f_{\alpha\beta}$ is approximated according to the formula

$$f_{\alpha\beta} = k_0 + k_1 \alpha + k_2 \beta + k_3 \alpha \beta, \tag{4.9}$$

where $k_0$, $k_1$, $k_2$, and $k_3$ are coefficients obtained for each cell by matching the values of $f_{\alpha\beta}$ at the (four) cell vertices. For each point inside a triangular cell (*i.e.*, a cell adjacent to the line $\alpha = \beta$ with vertices $(\alpha_i, \alpha_i)$, $(\alpha_{i-1}, \alpha_{i-1})$, and $(\alpha_i, \alpha_{i-1})$), a three-point interpolation
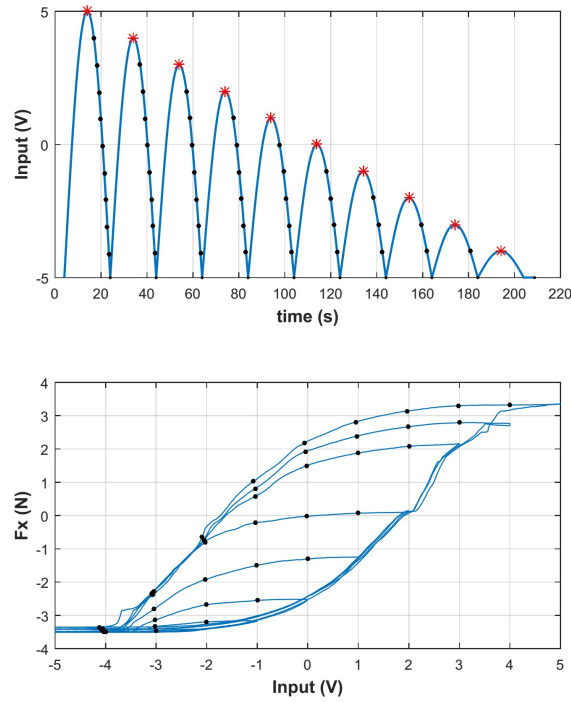
Figure 4.7: The input signal used for model identification (top); the resulting first-order transition (reversal) curves (bottom).

is used,

$$f_{\alpha\beta} = k_0 + k_1\alpha + k_2\beta, \tag{4.10}$$

where, again, $k_0$, $k_1$, and $k_2$ are obtained by matching the values of $f_{\alpha\beta}$ at the (three) cell vertices.

## 4.5.2 Output Force Estimation

In this subsection, we present results of some experiments which were performed in order to evaluate performance of the classical Preisach model in describing input-output behavior of the da Vinci instrument. In these experiments, for a number of test input signals, the output force $F_x$ was estimated using the developed Preisach model and compared with the actual measured force. The test input signals were chosen in the form of superposition of sinusoidal signals of different frequencies; the range of these frequencies corresponds to slow movements typically used by surgeons when performing actual minimally invasive surgical procedures. Specifically, the responses were evaluated for the following test input
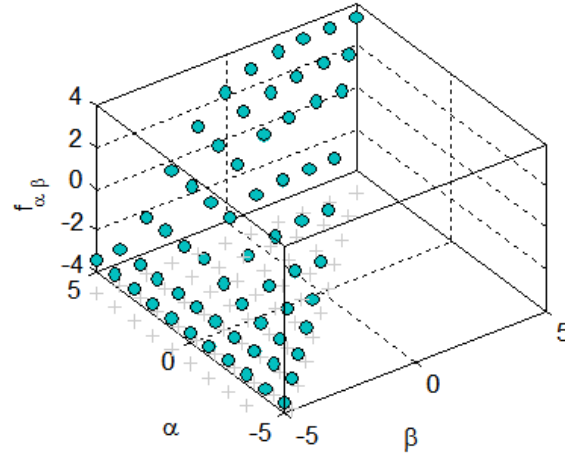
Figure 4.8: The mesh of experimentally obtained values $f_{\alpha\beta}$, $-5V \leq u(t) \leq 5V$, with resolution $\Delta\alpha = \Delta\beta = 1V$.

signals:

$$u_1(t) = 2\sin\left(\frac{2\pi}{10}t\right) + 2\sin\left(\frac{2\pi}{30}t + \pi\right) \text{ Volts,}$$

$$u_2(t) = 2\sin\left(\frac{2\pi}{10}t\right) + 2\sin\left(\frac{2\pi}{11}t\right) \text{ Volts,}$$

$$u_3(t) = \sum_{k=1}^{4}\sin\left(\frac{2\pi}{10 \cdot k}t\right) \text{ Volts.}$$

Figures 4.10, 4.11, and 4.12 demonstrate the responses of the developed Preisach model in comparison with the experimentally obtained responses of the actual da Vinci instrument for input signals $u_1(t)$, $u_2(t)$, and $u_3(t)$, respectively. In each of these figures, the top plot represents the responses in time domain, while the bottom plot demonstrates the input-output behavior of the instrument and the model. For each of the three test signals, the magnitude of the experimentally obtained force response, the maximum force estimation error, as well as RMS (root-mean-square) force estimation error were evaluated; these are summarized in Table 4.1.

| Test signal | Force response magnitude (N) | Maximum error (N) | RMS error (N) |
|---|---|---|---|
| $u_1(t)$ | 6.40 | 0.55 | 0.15 |
| $u_2(t)$ | 6.16 | 0.60 | 0.22 |
| $u_3(t)$ | 5.48 | 0.59 | 0.22 |

Table 4.1: Magnitude of the force response, maximum force estimation error, and RMS force estimation error for input signals $u_1(t)$, $u_2(t)$, and $u_3(t)$.
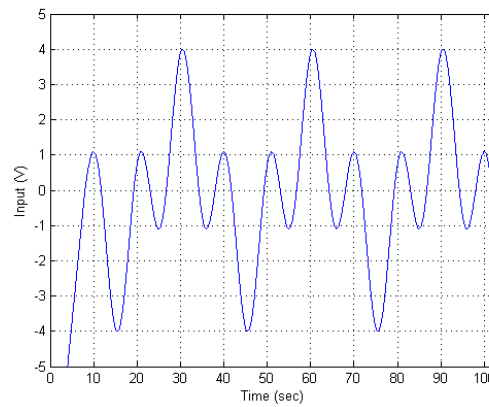


Figure 4.9: Input signal $u_1(t)$.

## 4.5.3 Discussion

It can be seen from the experimental results presented above that the developed Preisach model provides a close approximation of the forces at the tip of the da Vinci instrument. The errors presented in Table 4.1 are within the range for sensorized minimally-invasive surgical instruments (see for example [13]). It is also worth to mention that the specific combination of sinusoidal waves that comprise $u_1(t)$ results in a pattern that can roughly be described as cycles of oscillations with large and small magnitudes (see Figure 4.9). As expected, the resulting output response exhibits one large hysteresis loop as well as two minor loops, as can be clearly seen in Figure 4.10 (bottom). The two minor loops are symmetrical and of the same size, which illustrates the fact that the assumption of congruency, which is fundamental for Preisach modeling, holds in the case of the da Vinci instrument.
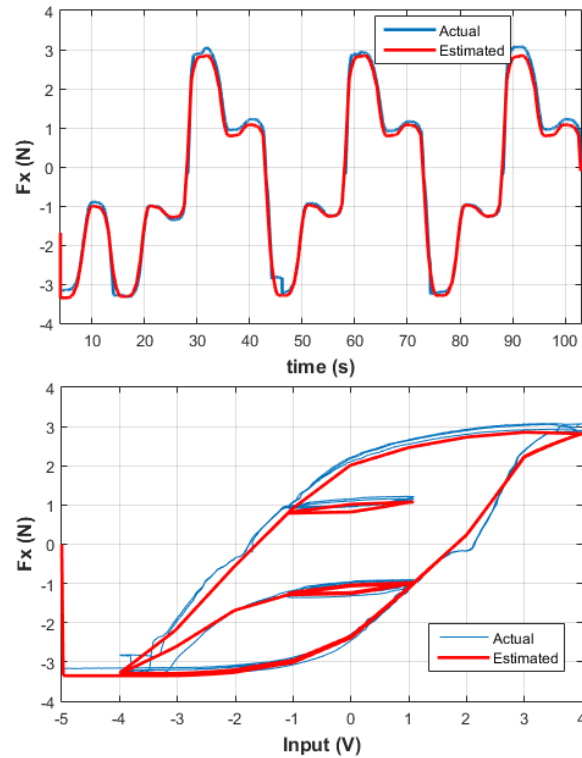
Figure 4.10: Response to input signal $u_1(t)$, measured vs. estimated (top); the corresponding input-output behavior (bottom).

## 4.6 Conclusion

In this chapter, the classical Preisach model of hysteresis was implemented and used for estimation of the forces at the tip of a da Vinci instrument. The model that describes the input-output behavior of EndoWrist™ forceps was identified and experimentally evaluated in the case of a rigidly fixed tip. The experimental results demonstrate that the developed approach allows for sufficiently precise prediction of the forces at the tip of the instrument. Implementation of the proposed approach for real-life surgical tasks, however, requires further studies. The major topics to be addressed include modeling the effect of motion at the tip when interacting with a soft environment, as well as the effect of coupling between different DOFs. Mathematical description of these effects can be combined with the model developed in this work to achieve real-time estimation of the forces at the tip of a da Vinci instrument for a variety of real life surgical scenarios. These are topics for future research.
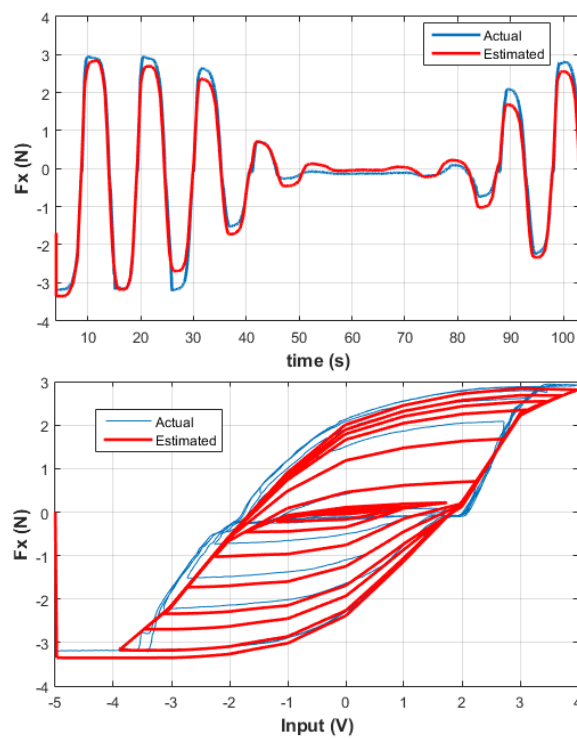
Figure 4.11: Response to input signal $u_2(t)$, measured vs. estimated (top); the corresponding input-output behavior (bottom).
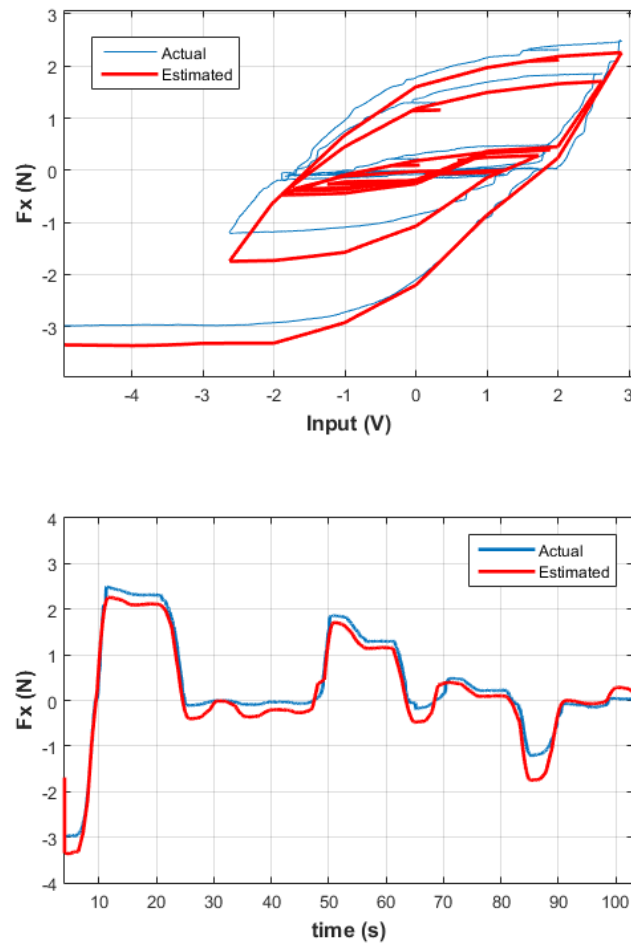
Figure 4.12: Response to input signal $u_3(t)$ measured vs. estimated (top); the corresponding input-output behavior (bottom).

# References

[1] G. S. Guthart and J. K. Salisbury, "The intuitive™ telesurgery system: Overview and application," in *IEEE International Conference on Robotics and Automation 2000*, (San Francisco, CA), pp. 618–621, IEEE, 2000.

[2] A. M. Okamura, "Haptic feedback in robot-assisted minimally invasive surgery," *Current Opinion in Urology*, vol. 19, pp. 102–107, 2009.

[3] Intuitive Surgical, Inc., *EndoWrist: Instrument and Accessory Catalog*, July 2011.

[4] "Intuitive Surgical: Image gallery." `http://www.intuitivesurgical.com/company/media/images/`, 2014.

[5] F. Anooshahpour, I. G. Polushin, and R. V. Patel, "Quasi-static modeling of the da Vinci instrument," in *IEEE/RSJ International Conference on Intelligent Robots and Systems (IROS)*, pp. 1308–1313, IEEE, 2014.

[6] F. Anooshahpour, I. G. Polushin, and R. V. Patel, "Tissue compliance determination using da Vinci instrument," in *IEEE International Conference on Robotics and Automation (ICRA)*, pp. 5344–5349, IEEE, 2015.

[7] I. D. Mayergoyz, *Mathematical models of hysteresis and their applications*. Academic Press, 2003.

[8] V. Agrawal, W. J. Peine, B. Yao, and S. Choi, "Control of cable actuated devices using smooth backlash inverse," in *IEEE International Conference on Robotics and Automation*, pp. 1074–1079, IEEE, 2010.

[9] T. N. Do, T. Tjahjowidodo, M. S. Lau, and S. J. Phee, "Nonlinear friction modelling and compensation control of hysteresis phenomena for a pair of tendon-sheath actuated surgical robots," *Mechanical Systems and Signal Processing*, vol. 60, pp. 770–784, 2015.

[10] S. B. Kesner and R. D. Howe, "Position control of motion compensation cardiac catheters," *Robotics, IEEE Transactions on*, vol. 27, no. 6, pp. 1045–1055, 2011.

[11] V. Hassani, T. Tjahjowidodo, and T. N. Do, "A survey on hysteresis modeling, iden-
    tification and control," *Mechanical systems and signal processing*, vol. 49, no. 1,
    pp. 209–233, 2014.

[12] I. Mayergoyz, "Mathematical models of hysteresis," *IEEE Transactions on Magnet-
    ics*, vol. 22, no. 5, pp. 603–608, 1986.

[13] A. L. Trejos, R. V. Patel, and M. D. Naish, "Force sensing and its application in min-
    imally invasive surgery and therapy: a survey," *Institution of Mechanical Engineers,
    Part C: Journal of Mechanical Engineering Science*, vol. 224, pp. 1435 –1454, 2010.

# Chapter 5

# A Motion Transmission Model for a Class of Tendon-Based Mechanisms with Application to Position Tracking of the da Vinci® Instrument

**T**endon-based motion/force transmission is a conventional approach in the design of surgical robots. However, due to compliance in the tendons and significant frictions between the tendons, the pulleys, and the sheath, tendon-based systems exhibit highly nonlinear behavior that, in particular, includes hysteresis. In this chapter, based on the concepts of creep theory in belt drive mechanics, a novel motion transmission model is developed for tendon-pulley mechanisms. The developed model is of pseudo-kinematic type; specifically, it relates the output displacement to both the input displacement and the input force. The model parameters are identified for a da Vinci® instrument, and the model performance is experimentally evaluated. The experimental results demonstrate greater than 50% improvement in terms of root-mean-square position error as compared to a more conventional friction/compliance-free kinematic model. The model is subsequently used for position control of the tip of the instrument, resulting in elimination of the static hysteresis and in accurate trajectory tracking.

---

# 5.1   Introduction

Tendon-based transmission is one of the primary approaches in the design of surgical tools for minimally invasive surgery (MIS). Tendon-based transmission allows the designer to remove the actuators from the patient's body, and helps to make the instruments sufficiently thin to pass through the trocar. Examples of well-known tendon-based surgical robots include the da Vinci® Surgical System [1] and the RAVEN II® open platform surgical robot [2].

Due to design simplicity and high power-to-weight ratio, tendon-based actuation has been employed in a variety of applications such as continuum robots [3], robotic hands [4], and laparoscopic instruments [5]. With all the advantages of the tendon-based transmission systems, they may exhibit substantially nonlinear behavior due to tendons' compliance and frictions between the tendons and the pulleys, as well as between the tendons and the sheath. In many robotic applications, the output of a tendon drive can be equipped with force/motion sensors, and therefore the inherent transmission nonlinearity can be compensated through feedback control (*i.e.*, [6, 7]). In the case of surgical robotics, however, sensors typically cannot be implemented at the distal end of the transmission, which results in uncertainty in the position of the joints and the applied torque. Examples are position [8–10] and force [11, 12] uncertainties that are reported for tendon-pulley based RAVEN II® surgical robot. While a good force estimation enhances the haptic feedback provided to the surgeon, an accurate motion estimation is also highly desirable in the emerging autonomous surgical robots [13–15]. Accurate positioning of a surgical tool can in principle be achieved by employing image processing techniques [10, 15]. However, a precise and computationally effective model of the system can significantly improve performance and robustness of the control algorithm.

Talasaz and co-authors [16] modeled the tendon-pulley based da Vinci® instrument as a rigid mechanism and identified its parameters accordingly; this model was subsequently used in a haptics-enabled MIS teleoperation system. In [8], an Unscented Kalman Filter (UKF) algorithm was designed for position control of three DOFs of the RAVEN II robot. The algorithm was augmented in [9] to enhance the position estimation using real-time stereo visual feedback. In both the aforementioned studies, the idler pulleys were ignored, the point-contact friction was assumed to be located at the joints of the input and the output

pulleys, and exponential springs were used to model the effect of the tendons' compliance. While improvement in positioning was shown in [8, 9], however, a relatively large number of the identified parameters and the estimated states together with a limited number of the states measured directly makes the already complicated method sensitive to parameter variations [12].

The authors previously investigated force transmission in the da Vinci instrument for the case where the output pulley was locked to a force sensor [17, 18]. Due to similarities observed between the force transmission behavior of the da Vinci® instrument and that of a typical tendon-sheath mechanism, two force transmission models were developed based on the tendon slip analysis [17]. In [18], it was demonstrated that the force transmission can also be accurately described by a Preisach hysteresis model. In [19], the apparent stiffness of a tendon-pulley transmission was described and evaluated in the palpation experiments.

The main contribution of this chapter is a novel motion estimation model which, in particular, allows for compensation of hysteresis in the motion transmission behavior of tendon-pulley drives. The model is derived based on the physical theory, known as the creep theory in the belt-drive mechanics, which describes a tendon's slippage on a pulley's surface. In tendon-pulley mechanisms, similarly to the belt drives, the predominant factor affecting the torque/force transmission between the tendon and the pulleys is the surface friction, which causes elongation of the tendon and its slippage on the pulley's surface. It is demonstrated in this chapter that, using tendon-creep analysis, contribution of each idler pulley to the overall nonlinear model of the system can be characterized; specifically, the effect of each idler pulley is similar to tendon's slip on a curved surface with a fixed length. Based on these considerations, in the proposed model, the total tendon slip on all pulleys of the system is represented by tendon's interaction with two imaginary curved surfaces; one in the forward and one in the return path. The interaction between the tendon and the corresponding surface involves the tendon slip and the tension decay along the corresponding path. In particular, our model encompasses distributed frictions as opposed to the point contact friction models addressed in [8, 9]. The proposed model can be considered as an extension of the conventional kinematics-based models, in that it additionally takes into account the relationship between the tendon elongation and the input (*e.g.*, the motor) torque. As a result, the proposed motion transmission model describes a nonlinear relationship between the input displacement, the output displacement, and the motor torque. An important property

of the developed model is its invertibility, which allows for its use in the real-time control applications. The model is implemented and experimentally verified for a da Vinci® instrument, specifically the EndoWrist™ microforceps [20], which utilizes tendon-pulley force/motion transmission mechanisms. Furthermore, a set of control experiments with a range of desired trajectory commands, including sinusoidal, exponential and multi-sine trajectories, was conducted in order to validate the effectiveness of the proposed modeling approach. The positioning performance is also thoroughly analyzed in terms of root mean squared errors, error distribution, and hysteresis compensation. The result indicates that the hysteresis in the motion transmission behavior of the instrument can be compensated using the closed-loop control based on the proposed modeling approach to achieve one-to-one (linear) relation between the input and output pulleys' rotations.

The chapter is organized as follows. In Section 5.2, the necessary background material on the belt drive mechanics and the tendon slip analysis is discussed. In Section 5.3, the proposed motion transmission model is derived. The experimental setup is described in Section 5.4. In Section 5.5, experimental results are presented; in particular, the parameters of the proposed model are identified for a da Vinci® instrument, and performance of the model in position control applications is evaluated. Section 5.6 concludes the chapter.

## 5.2 Preliminaries

### 5.2.1 Belt Drive Mechanics

In order to provide a basis for analysis of tendon-pulley systems, we first recall some notions from the belt drive mechanics. Belt drive is a form of tendon-pulley mechanisms which has been used widely in various mechanical systems such as refrigerators, washing machines, and vehicle engines for the purpose of power transmission. Belt drive mechanics is a subject of numerous studies, see for example [21–23]. The main challenge associated with the belt drive mechanics is how to properly describe the belt-pulley frictional interaction which is the principal factor in the power transmission. The classical creep theory is the most common approach to analysis of the belt drive mechanics [25]. The creep theory assumes that the interaction between the pulley and the belt is described by Coulomb fric-
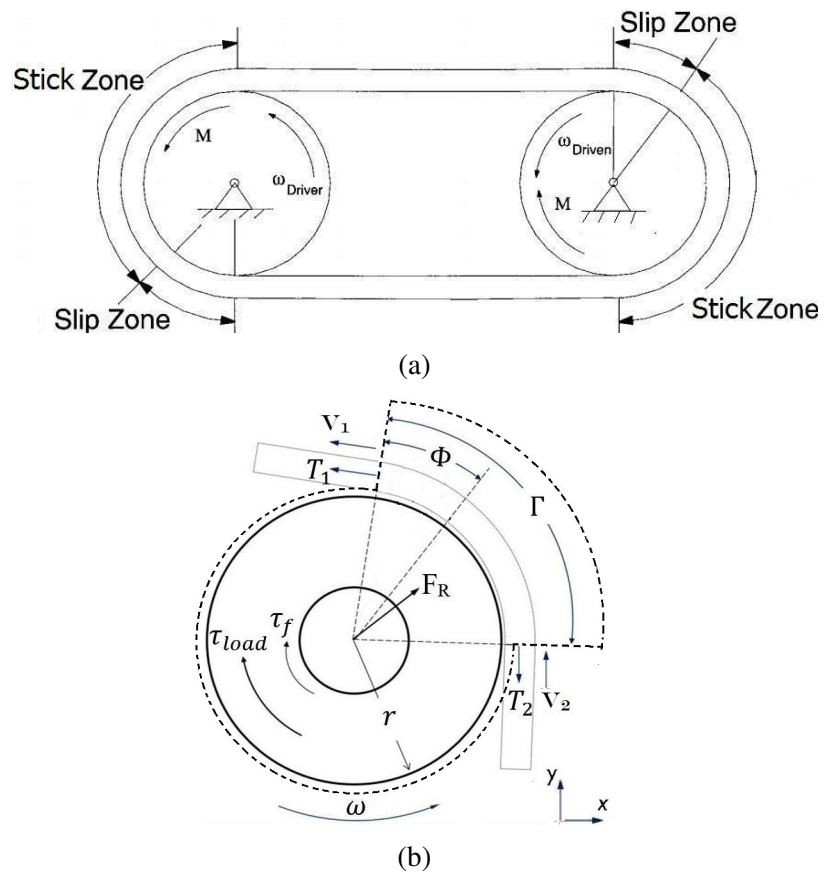
Figure 5.1: (a) Slip and stick zones on the input and output pulleys of a belt drive (adopted from [24]). (b) Free-body diagram of a driven pulley and the control volume (dashed line) in a belt drive mechanism.

tion model. Coulomb friction results in two distinct zones on the contact arc of the pulley, the stick zone and the slip zone, as shown in Figure 5.1(a). In the stick zone, there is no relative motion between the belt and the pulley, while a constant tension is maintained along the stick arc. In the slip zone, however, frictional forces cause the belt to stretch and/or contract, and consequently slip on the pulley, which results in the moment transmission [21].

In the steady-state mode (*i.e.*, where the pulleys rotate with a constant and sufficiently low velocity), the change of tension along the slip zone can be described by the following formula [26],

$$\frac{T_2}{T_1} = e^{-\mu_s \Phi}, \tag{5.1}$$

where, as shown in Figure 5.1(b), $T_1$ and $T_2$ are belt span tensions after and before the slip zone, respectively, $\mu_s$ is the coefficient of Coulomb surface friction, $\Phi \in [0, \Gamma]$ is the angular length of the slip zone, and $\Gamma \in [0, \pi]$ is the wrap angle. Note that, according to the creep theory, tension $T_2$ remains constant along the stick zone, and $\Phi$ increases as the transmitted moment increases.

In addition, from the conservation of linear momentum for the space-fixed control volume shown in Figure 5.1(b) (dashed line), one can derive the following equations which relate the joint normal force $F_R = (F_{Rx}, F_{Ry})$ to tensions $T_1$ and $T_2$ and the wrap angle $\Gamma$,

$$\begin{cases} \dot{m} V_1 \sin(\Gamma) = F_{Rx} - T_1 \sin(\Gamma), \\ \dot{m}(V_1 \cos(\Gamma) - V_2) = F_{Ry} + T_1 \cos(\Gamma) - T_2, \end{cases} \tag{5.2}$$

where $\dot{m}$ is the constant mass flow rate in the control volume, $V_1$ is speed of tendon entering and $V_2$ is the speed of tendon leaving the control volume, respectively. In the case of low-speed operation, the mass flow rate is negligible, and therefore equation (5.2) can be rewritten as follows:

$$\begin{cases} T_1 \sin(\Gamma) = F_{Rx}, \\ -T_1 \cos(\Gamma) + T_2 = F_{Ry}. \end{cases} \tag{5.3}$$

Similarly, from the conservation of angular momentum within the control volume and the

above assumption of a negligible mass flow, the following formula can be obtained:

$$T_2 - T_1 = -\frac{1}{r}(\tau_{load} + \tau_f), \tag{5.4}$$

where $\tau_f = \mu_J F_R r'$ is the joint frictional torque, $\mu_J$ is the friction coefficient, $r'$ is the inner radius of the pulley, $r$ is the outer radius of the pulley and $\tau_{load}$ is the external loading torque. Combining (5.4) and (5.3), one can obtain the following formula that describes the change of tension along the driven pulley,

$$T_2 - T_1 = -\frac{1}{r}\left(\tau_{load} + \mu_J r'\sqrt{(T_1^2 + T_2^2 - 2T_1 T_2 \cos(\Gamma))}\right). \tag{5.5}$$

Furthermore, the compatibility condition ensures that tendon extension due to change in tension must be compensated by an equal contraction, such that the total length of the tendon remains constant [25] and satisfy

$$\sum_{i=1}^{n} l_i T_i = L_t T_s, \tag{5.6}$$

where $L_t$ is the total tendon length, $l_i$ is the length of the tendon span $i \in \{1, \ldots, n\}$, and $T_s$ is the initial preset tension within the tendon.

In surgical robotic applications, the input torque and the rotation of the driving pulley can typically be measured, while the output torque and the rotational displacement of the output pulley are to be estimated. To solve for the output torque/displacement of a tendon-pulley system such as the one shown in Figure 5.2(a), equations (5.1) and (5.5) must be written for every single pulley in addition to equation (5.6) for the whole system. Solving such a set of equations requires extensive numerical computations, which is not desirable in real-time control application.

In this work, we propose a new method for modeling of tendon-pulley systems independently of their specific mechanical configuration. Specifically, as an idler pulley in a tendon-pulley drive does not bear any external loading (*i.e.*, $\tau_{load} = 0$), equation (5.5) for an idler pulley can be rewritten in terms of $T_2/T_1$, as follows:

$$\left(\frac{T_2}{T_1}\right)^2 - 2\frac{1 - \kappa \cos(\Gamma)}{1 - \kappa}\left(\frac{T_2}{T_1}\right) + 1 = 0, \tag{5.7}$$
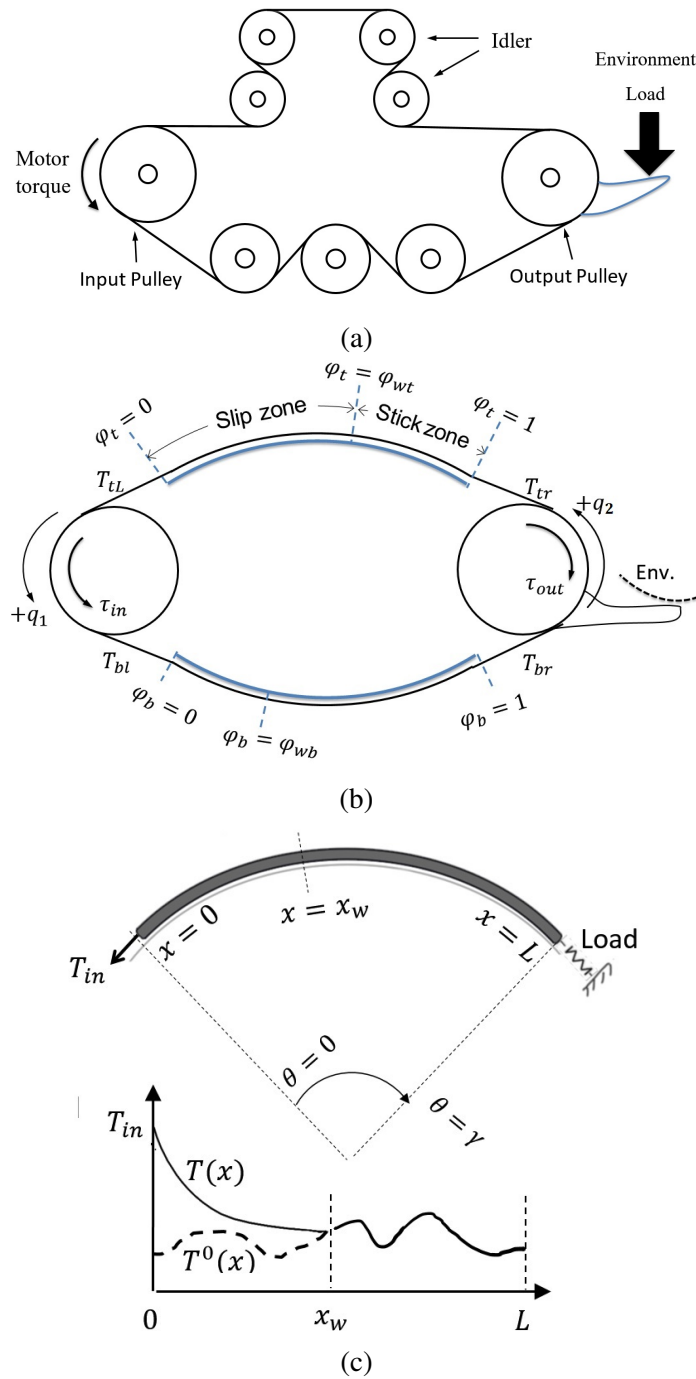
Figure 5.2: (a) A typical tendon-pulley drive in a surgical robot consists of the input and output pulleys as well as several idler pulleys for routing. The forward and backward routing are not necessarily similar. (b) The proposed equivalent dual tendon-surface system. Tendons' interaction with the curved surfaces accounts for tension decay and creeping effect in the original structure. (c) Tendon slipping on a curved surface under an axial load $T_{in}$.

where $\kappa := (\mu_J r'/r)^2$. Taking into account equations (5.1) and (5.7), one can conclude that the slip zone on idler pulleys always corresponds to a fixed bending angle, *i.e.*, $\Phi = const$. Since the effect of each idler pulley is similar to tendon slip on a fixed bent surface, the total effect of several pulleys can be represented by a single curved surface with a fixed length. In this study, we consider two curved surfaces on the forward and the return paths between the input and the output pulleys (Figure 5.2(b)) to replicate the tendon creep in the corresponding multiple-pulley system shown in Figure 5.2(a).

## 5.2.2   Tendon Slip Analysis

This subsection provides a brief review of some basic formulas for tendon slips on a curved surface which were previously developed by the authors in [17]. We first address the case of a single tendon-surface interaction, and subsequently extend our analysis to the case of dual tendon-surface interaction shown in Figure 5.2(b).

Figure 5.2(c) shows a tendon of length $L$ on a curved surface with a constant radius of curvature $R > 0$. In this case, application of a unidirectional force $T_{in}$ in a quasi-static condition results in distinct stick and slip zones formed along the tendon. Within the stick zone, tension remains equal to pre-tension $T^0(x)$, whereas the change of tension in the slip zone satisfies the following differential equation

$$dT(x) = -\frac{\mu T(x)}{R} \operatorname{sgn}(v)dx, \tag{5.8}$$

where $dx$ is an infinitesimal length, $T(x)$ is the tension in the segment, $\operatorname{sgn}(v)$ represents the direction of the impending motion of the tendon which follows the direction of the applied force, and $\mu$ is the coefficient of Coulomb friction. Integrating (5.8) results in the following formula for tension distribution in the slip zone:

$$T(x) = T_{in}\, e^{-\frac{\mu x}{R}\operatorname{sgn}(v)}. \tag{5.9}$$

The stick and the slip zones are separated by a point $x = x_w$ which is given by the formula

$$x_w := \min\{x \in [0, L] : T(x) = e^{-\frac{\mu x}{R}\operatorname{sgn}(v)} = T^0(x)\}. \tag{5.10}$$

The value of $x_w \in [0, L]$ is referred to as the slip length. Increase in the input force results in a larger slip zone. If the input force is large enough, the slip zone is extended to the distal end of the tendon (*e.g.* $x_w = L$), which causes force/motion transmission. Specifically, the tension at the load is given by the formula

$$T(L) = T_{in} e^{-\eta \, \mathrm{sgn}(v)}, \tag{5.11}$$

where $\eta := \mu L / R$ is the friction-bending constant. According to Hooke's law, the change of tension from $T^0(x)$ to $T(x)$ also results in tendon elongation, described by the following formula,

$$\Delta = \frac{1}{K_n} \int_0^L (T(x) - T^0(x)) dx, \tag{5.12}$$

where $\Delta$ is the total change of the tendon's length, and $K_n > 0$ is the stiffness of the tendon. Equations (5.9) to (5.12) describe the force and motion transmission in a single tendon in the presence of surface interaction.

The above analysis can be extended to the case of a dual tendon system shown in Figure 5.2(b), where tendons' interaction with two curved surfaces accounts for tension decay and creeping effect, while the angular positions of the input pulley $q_1$ and the output pulley $q_2$ impose geometric constraints only. Similarly to the case of single tendon-surface interaction, the following formulas can be derived that describe the tension distributions and tendons' elongations, respectively, in the dual tendon-pulley system:

$$T_t(\varphi_t) = \begin{cases} T_{tl} \, e^{-\eta_t \varphi_t \, \mathrm{sgn}(\dot{q}_1)} & \varphi_i < \varphi_{wt}, \\ T_t^0(\varphi_t) & \varphi_t \geq \varphi_{wt}, \end{cases} \tag{5.13}$$

$$T_b(\varphi_b) = \begin{cases} T_{bl} \, e^{\eta_b \varphi_b \, \mathrm{sgn}(\dot{q}_1)} & \varphi_b < \varphi_{wb}, \\ T_b^0(\varphi_b) & \varphi_b \geq \varphi_{wb}, \end{cases} \tag{5.14}$$

$$\Delta_i = \frac{1}{K_{ni}} \int_0^1 (T_i(\varphi_i) - T_i^0(\varphi_i)) d\varphi_i, \tag{5.15}$$

where $T_{il}$ is the tension in the left-end side of the $i$-th tendon, $\varphi_i := x_i/L$ is normalized position along the $i$-th tendon, $\varphi_{wi} := x_{wi}/L$ is the normalized slip length, and $i \in \{t, b\}$, where $t$ and $b$ denote the top and the bottom tendon in Figure 5.2(b), respectively. Further-

more, similarly to (5.4), the following two equations can be written for the input and output pulleys:

$$\tau_{in} = (T_{tl} - T_{bl})r_1, \tag{5.16}$$

$$\tau_{out} = (T_{tr} - T_{br})r_2, \tag{5.17}$$

where $\tau_{out}$ is the output torque, $T_{tr}$, $T_{br}$ are the tensions at the right end of the top and the bottom tendon, respectively, while $r_1$ and $r_2$ are the radii of the input and the output pulleys, respectively. Equations (5.13)-(5.17) describe the force transmission in a dual tendon system in a quasi-static condition. In order to derive the motion transmission model, however, the geometric constraints imposed on the tendon-pulley system must also be taken into account. These developments are presented in the next section.

## 5.3 The Motion Transmission Model

This section presents the main contribution of this paper. The geometric constraints imposed by the mechanism shown in Figure 5.2(b) require the elongation of the top tendon $\Delta_t$ to be related to the rotation of the input pulley $\Delta q_1$ and the output pulley $\Delta q_2$, as follows:

$$\Delta_t = \Delta q_1 r_1 - \Delta q_2 r_2. \tag{5.18}$$

Note that, in the above equation, $\Delta q_2 \neq 0$ only if the wave of tension (or equivalently the slip zone) has reached the output pulley, otherwise $\Delta q_1$ does not affect $\Delta q_2$. Applying the same line of reasoning to the bottom tendon, equation (7.1) can be extended to a more general formula

$$\Delta q_2 = \begin{cases} \frac{r_1}{r_2}\Delta q_1 - \frac{1}{r_2}\Delta_t & \text{if } \varphi_{wt} = 1, \\ \frac{r_1}{r_2}\Delta q_1 + \frac{1}{r_2}\Delta_b & \text{if } \varphi_{wb} = 1, \\ 0 & \text{otherwise}, \end{cases} \tag{5.19}$$

where $\varphi_{wt}$ and $\varphi_{wb}$ describe the transition state of each tendon. We will refer to equation (7.2) as the pseudo-kinematics-based model of the dual tendon mechanism. In contrast with kinematics-based models of rigid transmission systems, the pseudo-kinematics-based model does not only depend on the displacements, but is also a function of the tension dis-

tribution along the tendons as described in (5.15). Moreover, (7.2) replicates the hysteresis in the system; specifically, the first and second cases of (7.2) represent the ascending and descending branches of the hysteresis loops, respectively, while the third case describes transition between the two.

The value of $\Delta q_2$ can in principle be found from (7.2), provided that the elongation variables $\Delta_t$ and $\Delta_b$ and the transition variables $\varphi_{wt}$ and $\varphi_{wb}$ are known. Also, to calculate elongations from (5.15), one must know the current and the previous distributions of the tensions in both tendons. Solving (5.10)-(5.17) for all the values of interest is a challenging task due to the complexity of the possible solution(s). Therefore, in order to derive a closed form model suitable for real-time control applications, two additional assumptions are made. Given a scalar function $x(t)$ of time $t \in \mathbb{R}$, denote $t_x^+(t) := \sup\{\tau \le t : x(\tau) > 0\}$, and $t_x^-(t) := \sup\{\tau \le t : x(\tau) < 0\}$. A switching function with memory $J[x(t)]$ is defined as follows,

$$J(x(t)) := \begin{cases} 1 & \text{if } t_x^+(t) > t_x^-(t), \\ 0 & \text{if } t_x^+(t) < t_x^-(t). \end{cases} \tag{5.20}$$

It is easy to see that $J(x(t)) = 1$ if $x(t) > 0$, while $J(x(t)) = 0$ if $x(t) < 0$. On the other hand, if $x(t) = 0$, then $J(x(t))$ is equal to either $1$ or $0$ depending on whether $x(t)$ approached zero from the positive or the negative side[1]. The following two assumptions are made.

**Assumption 1.** *The power between the input and the output pulley is transmitted only through the tendon which is being pulled by the input pulley. Tension in the pushed tendon is zero, i.e., $T_b(\varphi_b) \equiv 0$ whenever $J(\dot{q}_1(t)) = 1$, and $T_t(\varphi_t) \equiv 0$ whenever $J(\dot{q}_1(t)) = 0$.*

**Assumption 2.** *Tension propagates immediately along the active tendon, i.e., $\varphi_{wt} = J(\dot{q}_1(t))$, and $\varphi_{wb} = 1 - J(\dot{q}_1(t))$.*

Under Assumptions 1 and 2, equations (5.13), (5.14), and (5.15) become

$$T_t(\varphi_t) = J(\dot{q}_1(t)) T_{tl} e^{-\eta_t \varphi_t}, \tag{5.21}$$

---

[1]Strictly speaking, there exist some curious functions $x(t)$ for which $J(x(t))$ is not well-defined for some $t$. In this work, however, we avoid these mathematical difficulties by assuming that all functions of interest $x(t)$ are such that $J(x(t))$ is well-defined for all $t$.

$$T_b(\varphi_b) = (1 - J(\dot{q}_1(t)))\, T_{bl}\, e^{\eta_b \varphi_b}, \tag{5.22}$$

$$\Delta_i = \frac{1}{K_{ni}} \int_0^1 T_i(\varphi_i) d\varphi_i, \tag{5.23}$$

where $i \in \{t, b\}$. Combining equation (5.23) with (5.21) and (5.22), respectively, one gets the following formulas that describe elongations of the top and bottom tendons, respectively,

$$\Delta_t = \frac{J(\dot{q}_1)}{K_{nt}} \int_0^1 T_{tl}\, e^{-\eta_t \varphi_t} d\varphi_t, \tag{5.24}$$

$$\Delta_b = \frac{(1 - J(\dot{q}_1))}{K_{nb}} \int_0^1 T_{bl}\, e^{-\eta_b \varphi_b} d\varphi_b. \tag{5.25}$$

Taking into account Assumption 1, it follows from equation (5.16) that $T_{tl} = \tau_{in}/r_1$ whenever $J(\dot{q}_1) = 1$, and $T_{bl} = -\tau_{in}/r_1$ whenever $J(\dot{q}_1) = 0$. Substituting these expressions into equations (5.24), (5.25), and performing integration, one obtains

$$\Delta_t = J(\dot{q}_1) \frac{1 - e^{\eta_t}}{r_1 \eta_t K_{nt}} \tau_{in}, \tag{5.26}$$

$$\Delta_b = (1 - J(\dot{q}_1)) \frac{e^{\eta_b} - 1}{r_1 \eta_b K_{nb}} \tau_{in}. \tag{5.27}$$

Taking into account Assumption 2 as well as equations (7.2), (5.26) and (5.27), the total rotation of the output pulley is

$$\Delta q_2 = J(\dot{q}_1) \alpha_1 \tau_{in} + (1 - J(\dot{q}_1)) \alpha_2 \tau_{in} + \beta \Delta q_1, \tag{5.28}$$

where the constant parameters $\alpha_1$, $\alpha_2$ and $\beta$ are defined as

$$\alpha_1 := \frac{1 - e^{\eta_t}}{r_1 r_2 \eta_t K_{nt}},$$

$$\alpha_2 := \frac{e^{\eta_b} - 1}{r_1 r_2 \eta_b K_{nb}}, \tag{5.29}$$

$$\beta := \frac{r_1}{r_2}.$$

Equation (7.3) will be used to estimate $q_2$ for given $q_1$ and $\tau_{in}$. The first and second terms in (7.3) describe the effect of tendon elongation on the motion transmission, while the third term represents the geometrical relationship between $q_1$ and $q_2$ similar to kinematic

constraints in rigid transmissions. In the absence of friction (*e.g.*, $\eta_t = \eta_b \to 0$), and/or in the case of zero compliance ($K_{nt} = K_{nb} \to \infty$), equation (7.3) indicates that the output is a scaled version of the input, which is similar to the case of rigid transmissions.

**Remark 5.1.** *Creep theory assumes that friction is zero at zero relative velocity between the belt and pulley, resulting in constant tension in the stick zone. This limiting assumption, however, is not valid in general. In particular, it is in fact a common practice to assume that the stick zone has a memory of its previous loading for the case of tendon slip on a fixed surface. Nonetheless, in our study as a result of Assumptions 1 and 2, the history of the input force has no effect of the motion transmission.*

**Remark 5.2.** *It can be shown that the transmission characteristics of the tendon motion on the imaginary surface is independent from the radius of curvature R, but depends on the total bending as studied in [27].*

**Remark 5.3.** *Assumption 1 presumes negligible pretension in the tendons. If the pretension is sufficiently large, it can be shown that the pseudo-kinematic formula of (7.3) can be updated to the following form:*

$$
\begin{aligned}
\Delta q_2 \approx & J(\dot{q}_1)(\alpha_1 \tau_{in} + \gamma_1 \Lambda) \\
& + (1 - J(\dot{q}_1))(\alpha_2 \tau_{in} + \gamma_2 \Lambda) + \beta \Delta q_1,
\end{aligned}
\tag{5.30}
$$

*where constant $\Lambda \geq 0$ is a weighted sum of the area under the tension distribution of the top and the bottom tendons [17], and $\gamma_1$, $\gamma_2 \geq 0$ are constant parameters. The full derivation of formula (7.5) is given in the Appendix.*

## 5.4 Experimental Setup

For experimental evaluation of the modeling approach developed above, an EndoWrist® micro-forceps instrument was used as a testbed. The instrument was mounted on an actuation system as shown in Figure 5.3. The setup consists of four sets of motor-timing belt mechanism that drive the instrument's pulleys, and a camera for motion detection. The actuation system utilizes four Faulhaber 2642W024CR DC motor-encoders. The motors were driven using Maxon 4-Q-DC servo amplifiers set to current mode.
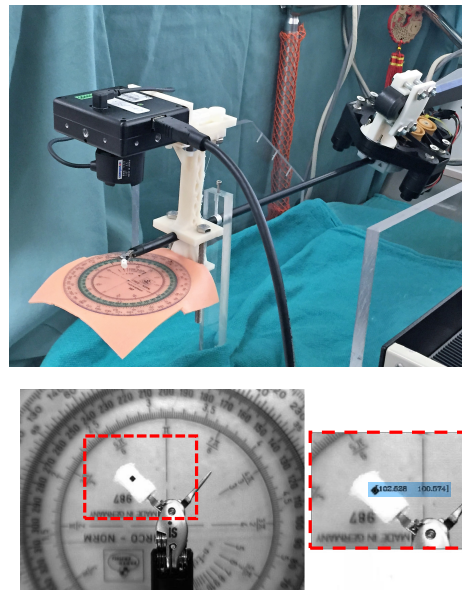
Figure 5.3: The experimental setup: the overall view (top); the instrument tip from the point of view of the camera (bottom).

The micro-forceps instrument used in this study consists of four sets of cable driven mechanisms that provide the tip with four rotational degrees of freedom: two DOFs for gripping motion, one for rolling the shaft, and one for the pitch motion of the tip. While there is no notable coupling between the roll and the gripping degrees of freedom, the pitch has a coupling effect on the gripping. In this study, the motion of only one of the jaws is studied, while the coupling effect is left for future investigations.

On the distal side of the instrument, a Point Grey® camera Dragonfly2 DR2-COL, mounted on a 3D-printed fixture, was used to capture the movements of the tip in real-time. The camera was secured on the instrument shaft to maintain a fixed vantage point during the experiments. The blob detection method [28] was implemented in C++ using OpenCV for tracking the tip position. A cylindrical cover was added to the jaw to provide a flat area for the marker as shown in Figure 5.3. The accuracy of detection was found to be $\pm$ 0.47 deg. In order to avoid the undesirable image noise, a steady lighting condition was maintained during the experiments. To increase the speed of the blob detection algorithm, the search zone was limited to a portion of the original captured image as shown in Figure 5.3 (bottom-right). Proportional-Integral-Derivative (PID) controller was implemented to control the

motor rotation $q_1$. The PID gains were adjusted to $k_p = 0.05$ ($\frac{A}{deg}$), $k_d = 0.0004$ ($\frac{A \cdot s}{deg}$) and $k_I = 0.01$ ($\frac{A}{deg \cdot s}$). The sampling rate of the control loop was set to 100 Hz, and the tip position was updated at 20 Hz rate due to the limitations of the image capturing process.

## 5.5 Experimental Results and Model Validation

### 5.5.1 Motion Transmission Analysis

In this subsection, the motion transmission behavior of the da Vinci® instrument is investigated. Figure 5.4(a) illustrates a sample response to a $0.1$ Hz sinusoidal command with the amplitude of $20$ degrees. The figure suggests that a hysteresis-like relationship exists between the motor angular position and the tip rotation angle. Hysteresis, by definition, is the presence of a non-degenerate input-output closed curve as the excitation signal approaches a zero-frequency signal [29]. To validate the presence of hysteresis, a series of sinusoidal commands with frequencies ranging from $0.01$ Hz to $0.7$ Hz and $15$ degrees amplitude was applied. Figure 5.4(b) shows the resulting input-output behavior. As can be seen from this figure, the behavior of the system converges to a fixed loop as frequency of the command signal tends to zero, which validates the existence of hysteresis. Furthermore, Figure 5.4(c) indicates the presence of minor loops in the input-output behavior of the system, which demonstrates a backlash-like hysteretic behavior. On the other hand, no dynamic effect is detectable for the frequencies lower than $0.1$ Hz, which suggests a static model for the system in low frequencies.

### 5.5.2 Model Identification

In order to identify the parameters of the proposed model (7.3), 15 experiments were conducted using $0.1$ Hz sinusoidal commands with varying amplitude of $20$, $15$, $10$, $5$ and $2.5$ degrees. Each experiment was repeated three times to account for possible non-repeatabilities. The initial positions of the tip were chosen arbitrarily. Parameters $\alpha_1$, $\alpha_2$ and $\beta$ were adjusted to minimize the root mean square error (RMSE), and the resulting values are shown in Table 7.1. The identified value of $\beta$ closely matches with the actual ratio

(a)

(b)

(c)
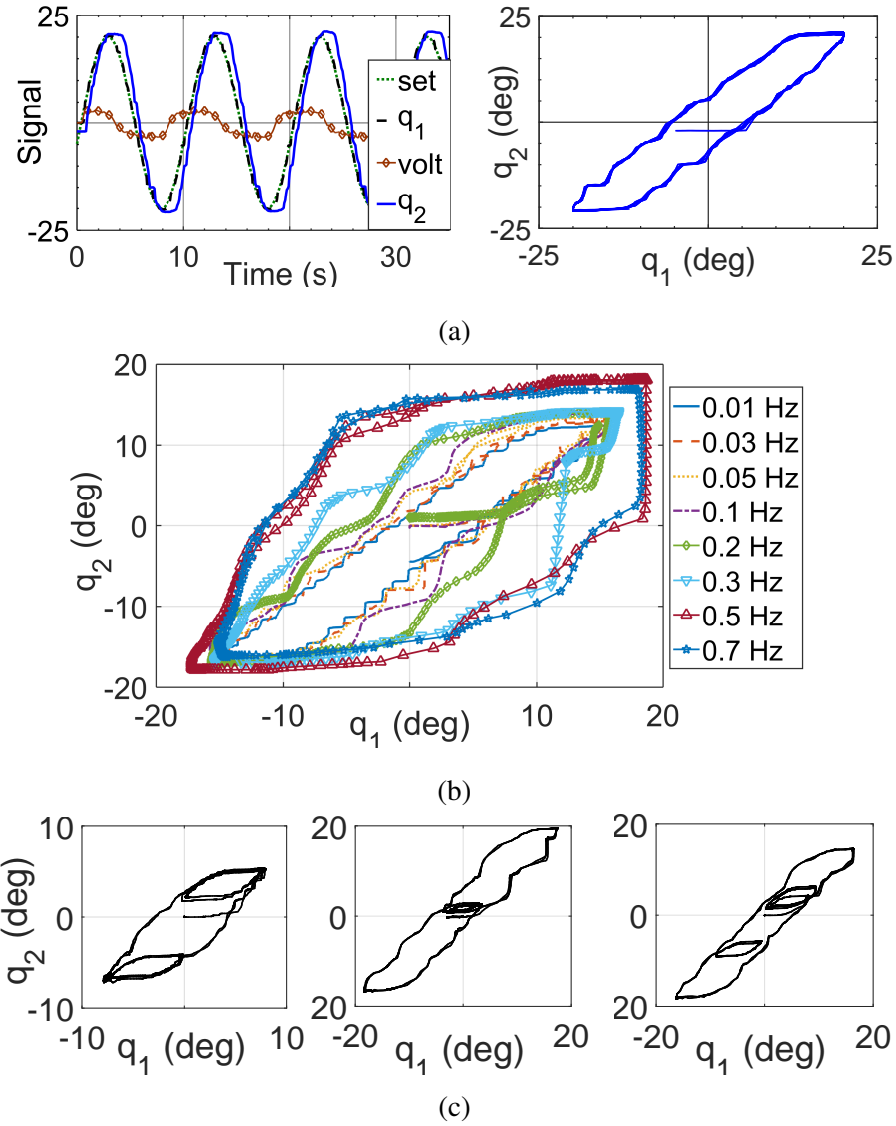
Figure 5.4: (a) An example of system's response to a 0.1 Hz sinusoidal input displacement (left); the hysteresis behavior (right). (b) System response to sinusoidal inputs with a fixed amplitude $q_{1\,\text{max}} = \pi/12$ rad and various frequencies. (c) Minor hysteresis loops in the system's response to the following desired input signals: $5sin(2\pi/30\,t) + 5sin(2\pi/10\,t)$ (left); $5sin(2\pi/30\,t+\pi)+5sin(2\pi/10\,t)$ (middle); $10sin(2\pi/30\,t+\pi/2)+7.5sin(2\pi/10\,t)$ (right).

Table 5.1: The identified values of the model's parameters

| $\alpha_1$ | $\alpha_2$ | $\beta$ |
|---|---|---|
| -1.626 | -1.213 | 1.142 |

of the pulleys in the da Vinci® instrument. As measured, $r_1 = 2.6$ mm and $r_2 = 2.4$ mm, resulting in $(r_1/r_2) = 1.08$ in the da Vinci® instrument versus the identified $\beta$ value of 1.142.

Figure 5.5(a) shows the estimates of the instrument tip angle $q_2$ along with the actual measurements using the camera. The motor rotation angle $q_1$ was controlled to track sinusoidal commands with various frequencies ranging from 0.05 Hz to 0.2 Hz. The tip position was estimated based on the proposed model (7.3). To further validate the model, its performance was evaluated by applying a multi-sinusoidal command signal using Schroeder-phased method,

$$q_1(t) = \sum_{k=1}^{N} A_m \, cos(\omega_k t + \phi_k) \tag{5.31}$$

where $\phi_k$ is chosen to minimize the crest factor [30],

$$\phi_k = \phi_1 - \frac{-k\pi(k-1)}{N}. \tag{5.32}$$

In our experiment, $\phi_1 = \pi/2$, and 10 different frequencies between 0.01 and 0.1 Hz were selected for generating the desired command signal. The results are shown in Figure 5.5(b).

Figure 7.11(a) shows the Box-Whisker plot of error, in which the range of error is shown along with the median and 25th and 75th percentiles. The outliers are marked based on the 99.3% coverage of the error values for each experiment[2]. As observed, implementation of the proposed model has significantly reduced the range of errors in comparison with that of the purely kinematics-based estimation. The probability distribution of the errors are also shown in Figure 7.11(b)[3]. Figure 7.11(b) indicates that, for the proposed model, majority of the error values lie within $\pm 1.5°$ and concentrated in the vicinity of zero, while the

---

[2]Let $\sigma$ be the standard deviation of the error distribution. The outliers set, **O**, was defined as follows:

$$\mathbf{O} := \big\{ o \, | \, (o > Q_3 + w \cdot \text{IQR}) \, or \, (o < Q_1 - w \cdot \text{IQR}) \big\},$$

in which IQR $= Q_3 - Q_1$ is the interquartile range, $Q_1$ and $Q_3$ are the 25th and 75th percentiles, respectively, and $w$ is the Whisker length. In this set of experiments, $w$ was set to 1.5, associated to approximately $\pm 2.7 \, \sigma$ or 99.3% coverage of the error values for each experiment.

[3]The height of each bar is the probability of the absolute error within the corresponding bin, i.e. $h_i = n_i/N$, where $h_i$ is the height of the i-th bar, $n_i$ is the number of error samples within the i-th bin, and $N$ is the total number of samples.
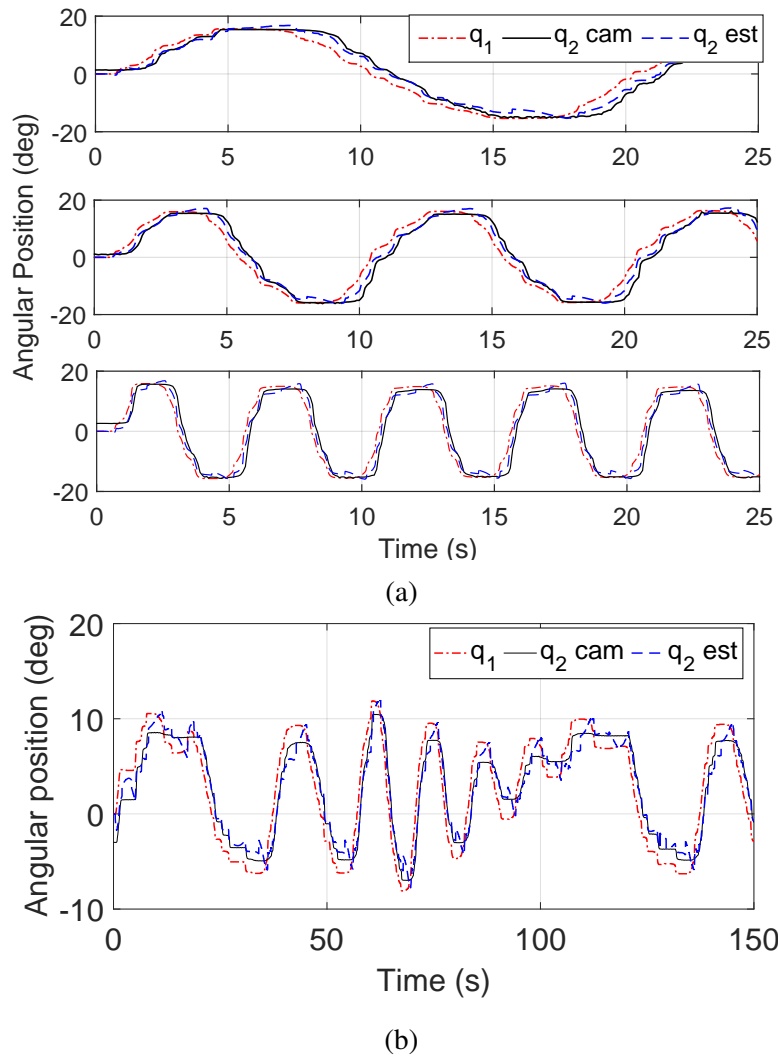
Figure 5.5: The proposed model estimation results for: (a) sinusoidal commands with frequencies of 0.05, 0.1, and 0.2 Hz, and (b) a multi-sinusoidal command signal. The dash-dot red line is the motor (input) position, the solid black line is the tip (output) position measured by the camera, and the dash blue line is an estimate of the output position by the proposed model.

kinematics-based estimation resulted in higher probability of larger error values. Further-more, Table 5.2 summarizes the results in terms of the RMSEs between the estimates and measurements, Goodness-of-Fit (GoF), and adjusted R-squared. GoF is calculated based on the normalized RMSE[4], and GoF of 1 (100%) corresponds to a perfect fit. R-squared values are the square of the correlation between the measured values and the model es-timations, indicating how well the model can predict the response variation. R-squared values are adjusted according to the number of parameters for a fair comparison[5]. It can be seen that the proposed model significantly improves the estimation accuracy of the actual tip position in comparison with that of the kinematics-based estimation; in fact, RMSE values show at least 50% decrease as compared to those of the kinematics-based model. Adjusted R-Squared values also indicate that the nonlinear terms corresponding to param-eters $\alpha_1$ and $\alpha_2$ in the proposed model considerably improve the accuracy as compared to the kinematics-based estimation.

Table 5.2: The model estimation results in comparison to those of kinematics-based model

| Signal type | | Sine | Sine | Sine | Multi-Sine |
|---|---|---|---|---|---|
| Frequency [Hz] | | 0.05 | 0.1 | 0.2 | 0.01-0.1 |
| | **PM** | **1.2522** | **1.6282** | **2.1241** | **0.8607** |
| RMSE | KM | 3.1258 | 3.7478 | 4.2512 | 2.2743 |
| | Improv. | 59.9% | 56.5% | 50.0% | 62.2% |
| Goodness-of-Fit | **PM** | **88.9%** | **86.4%** | **82.8%** | **83.1%** |
| | KM | 72.3% | 68.7% | 65.6% | 55.4% |
| Adjusted R-Squared | **PM** | **0.9877** | **0.9815** | **0.9704** | **0.9715** |
| | KM | 0.9232 | 0.9020 | 0.8815 | 0.8009 |

*PM and KM refer to as the proposed model and kinematics-based model.

---

[4]GoF is defined by,

$$\text{GoF} = 1 - \frac{\|q_2 - \hat{q}_2\|}{\|\hat{q}_2 - \Sigma_{k=1}^{k=N}\hat{q}_2(k)/N\|},$$

where, $q_2$ is the measured tip angle by camera, $\hat{q}_2$ is the tip angle estimated by the proposed model, and $N$ is the total number of samples.

[5]Adjusted R-squared are calculated based on the following equation:

$$\text{Adjusted R-squared} = 1 - \frac{(N-1)\text{SSE}}{(N-m)\text{SST}},$$

where SSE and SST stand for sum of squared errors of estimation and total sum square of estimation varia-tions, and $m$ is the number of parameters ($m = 3$ for the proposed model, and $m = 1$ for the kinematics-based estimation).

(a)



(b)
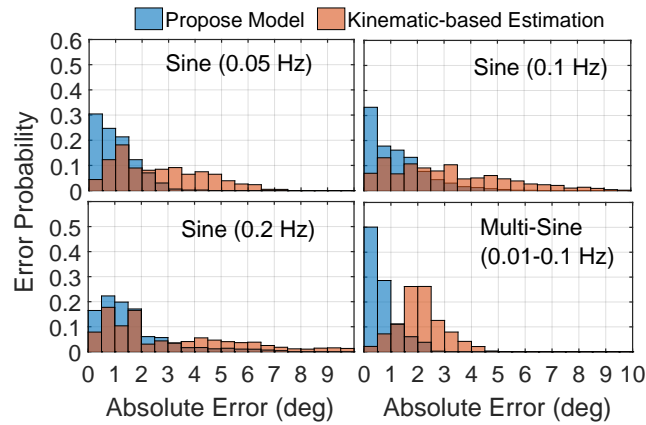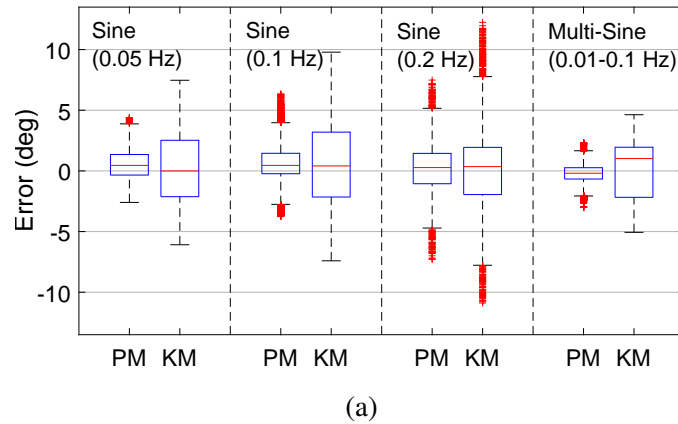
Figure 5.6: (a) Error distributions of the proposed model in comparison with those of kinematics-based estimation along with (b) the absolute error probability. Inputs are sinusoidal commands with frequencies of 0.05, 0.1, and 0.2 Hz, and a multi-sine command with frequency range of 0.01-0.1 Hz. PM and KM refer to as the proposed model and kinematics-based estimation, respectively.

Table 5.3: Position control RMSEs

| Signal type | Frequency (Hz) | KM RMSE (deg) | PM RMSE (deg) | Control RMSE (deg) |
|---|---|---|---|---|
| Sine | 0.01 | 3.1330 | 1.2761 | 1.4920 |
| Sine | 0.05 | 3.2818 | 1.2499 | 2.3546 |
| Sine | 0.1 | 4.0079 | 2.1849 | 4.0821 |
| Sine | 0.2 | 6.1706 | 4.4009 | 7.2908 |
| Exponential decay | 0.01 | 1.7045 | 0.8213 | 0.5289 |
| Multi-Sine | 0.015-0.075 | 2.8541 | 1.33854 | 1.6321 |

*PM and KM refer to as the proposed model and kinematics-based model.

### 5.5.3 Control results

A primary goal of modeling a tendon-based system is to use the developed model in a control algorithm to compensate for the hysteresis. To this end, this section provides a set of experimental results that evaluate the effectiveness of the proposed model in control applications. A set of experiments were conducted using a PID controller to control the tip position in the da Vinci® instrument, where the position estimated by the proposed model was used in the control loop to compute the tracking error. No visual feedback was used in the control process, and the camera measurements are only provided for the sake of comparison. Figures 5.7 and 5.8 show control results for sinusoidal commands with frequencies of 0.01 Hz, 0.05 Hz, 0.1 Hz and 0.2 Hz. As observed, the instrument tip closely tracks the desired trajectory, and the PID controller is able to largely eliminate the hysteresis for the two lowest frequencies as displayed in the lower-right sub-figures. Furthermore, Figure 5.9(a) shows a control result for an exponential decay command with a base frequency of 0.01 Hz, and Figure 5.9(b) displays the result for a multi-sine command with 5 frequencies ranging from 0.015-0.075 Hz. Table 5.3 summarizes the control results in terms of RMSEs. As expected, the control error increases as the frequency of the command signal grows, which can be attributed to unmodeled dynamic effects. This includes the model estimation error in part plus the control error between the estimation and the desired trajectories.
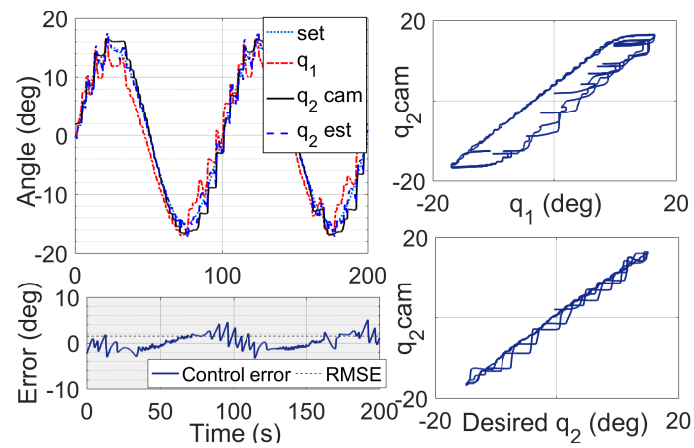
(a) 0.01 Hz
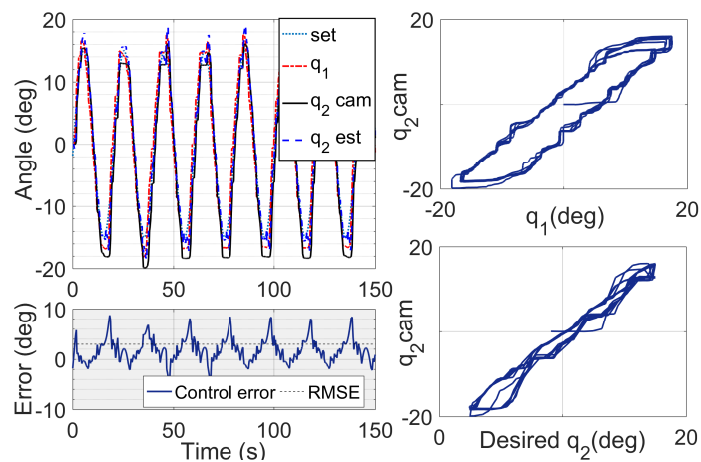


(b) 0.05 Hz

Figure 5.7: Control results for sinusoidal commands with frequency of (a) 0.01 Hz and (b) 0.05 Hz. The transmission hysteresis with and without the proposed model is shown in the bottom-right and top-right subfigures, respectively.
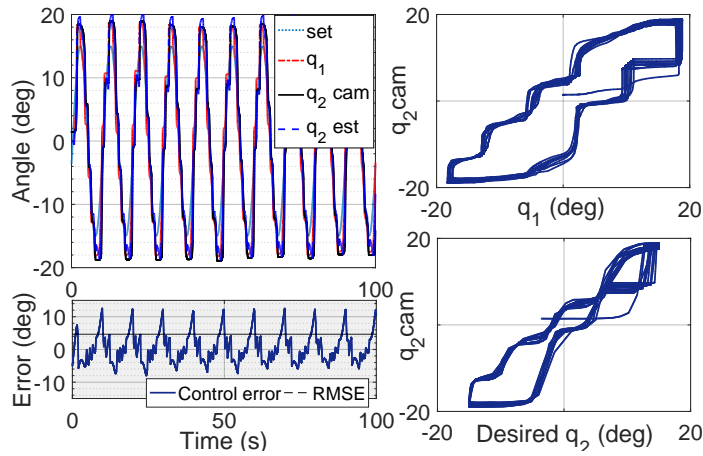
(a) 0.1 Hz
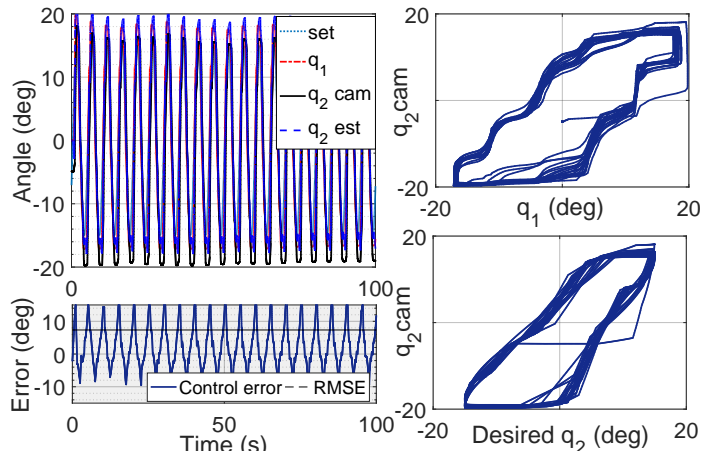


(b) 0.2 Hz

Figure 5.8: Control results for sinusoidal commands with frequency of (a) 0.1 Hz and (b) 0.2 Hz. The transmission hysteresis with and without the proposed model is shown in the bottom-right and top-right subfigures, respectively.
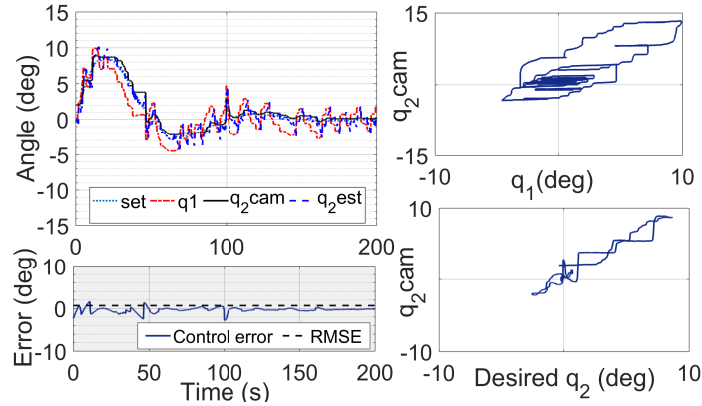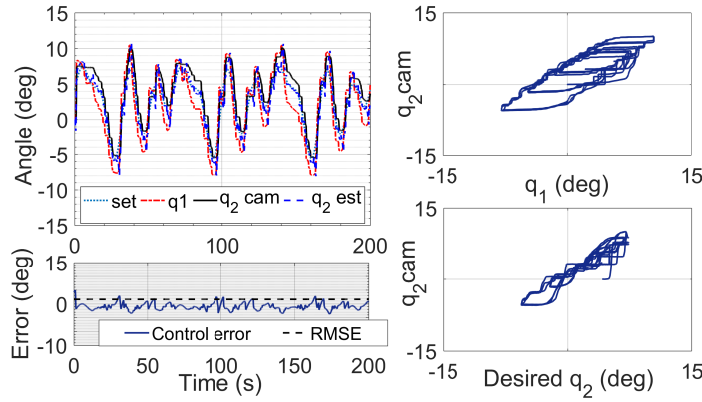
Figure 5.9: Control result for (a) an exponentially decaying sinusoidal command with a frequency of 0.01 Hz, time constant of 0.025 sec and (b) a multi-sine input command with five frequencies ranging from 0.015 Hz to 0.075 Hz.

## 5.5.4   Discussions

- Figure 5.10 shows the proposed model performance in mimicking the hysteresis of the system for a sample sinusoidal signal with 0.05 Hz frequency. As observed, the proposed model closely captures the hysteresis effect, providing a better estimation compared to the kinematics-based estimation.

- The observed jumps in error signals in Figure 5.7 can be associated with the trajectory extrema, where the direction of the motion changes. This is because of the Assumption 2, under which the wave of tension was assumed to propagate immediately after direction change. This effect is also visible in Figure 5.10, where there
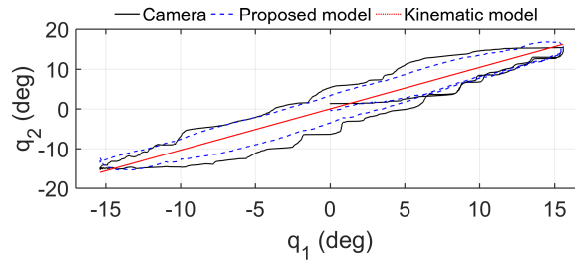
Figure 5.10: Hysteretic behavior of the proposed modelling approach versus the kinematics-based estimation.

is a small discrepancy at the returning points between the estimation and the actual hysteresis.

- Assumption 1 implies that the pre-tension is zero. Despite the strict assumption made in the derivation of the model, the experimental results validate that the model can predict the hysteretic behavior of tendon-pulley system. In other words, the motion transmission in a class of tendon-pulley systems can adequately be characterized by that of tendon-surface systems under zero pre-tension.

## 5.6 Conclusion

In this chapter, a new motion estimation model for tendon-pulley transmission mechanisms was proposed which is based on physical principles governing such mechanisms. The model was derived using the creep theory and tendon slip analysis, where distributed tension and elastic creep were taken into account. The proposed model was validated experimentally using a da Vinci® instrument as a test case. The results clearly demonstrated the effectiveness of the proposed model in reducing the estimation error by more than 50% in terms of RMSE as compared to the purely kinematics-based estimation. Furthermore, the model was investigated as a part of a position control scheme, where the estimated position of the tip was used for computation of the position error. The result indicated high accuracy positioning with RMSEs ranging from 0.5 to 2.3 degrees for various low frequency desired trajectories. It also demonstrated that the proposed approach can effectively eliminate the quasi-static hysteresis of a tendon-pulley transmission.

Future work will focus on the extension of the developed model for higher number of
DOFs to account for the coupling effect in surgical robots and instruments. Additionally,
further work related to the use of the proposed modeling approach in a hybrid force-position
control scheme is a part of our ongoing research. The final goal of our ongoing research is
to develop a comprehensive theory which allows for simultaneous description of the force
and motion transmission in tendon-pulley drives, and its subsequent integration into the
robot dynamic modeling.

## 5.7 Appendix: Pseudo-Kinematic Model for a System With Large Constant Pretension

In this section, the pseudo-kinematic model of (7.2) is solved for a dual tendon-surface
mechanism with equally pretensioned top and bottom tendons, *i.e.* $T_t^0(\varphi_t) = T_b^0(\varphi_b) = T_s$.
To this end, from the first two cases of equation (7.2), one can derive the following formula:

$$\Delta_t + \Delta_b = 0. \tag{5.33}$$

which implies that the amount of elongation on one side is equal to the amount of shrinkage
on the other side. Equation (A.9) can be solved to obtain the following formula [17],

$$\int_0^1 \frac{T_t(\varphi_t)}{K_{nt}}d\varphi_t + \int_0^1 \frac{T_b(\varphi_b)}{K_{nb}}d\varphi_b =$$
$$\int_0^1 \frac{T_t^0(\varphi_t)}{K_{nt}}d\varphi_t + \int_0^1 \frac{T_b^0(\varphi_b)}{K_{nb}}d\varphi_b = \Lambda. \tag{5.34}$$

Equation (5.34) can be interpreted as a weighted sum of the areas under the tension distri-
bution curves of the top and the bottom tendons remains constant regardless of the input.
Since the tension propagation is immediate, *i.e.*, $\varphi_{wt} = \varphi_{wb} = 1$, we have

$$aT_{tl} + bT_{bl} = \Lambda, \tag{5.35}$$

where

$$a = \frac{\operatorname{sgn}(\dot{q}_1)}{-K_{nt}\eta_t}(e^{-\eta_t \operatorname{sgn}(\dot{q}_1)} - 1),$$

$$b = \frac{\operatorname{sgn}(\dot{q}_1)}{K_{nb}\eta_b}(e^{\eta_b \operatorname{sgn}(\dot{q}_1)} - 1).$$

On the other hand, the sum of first two cases of formula (7.2) results in the following pseudo-kinematic equation:

$$\Delta q_2 = \frac{r_1}{r_2}\Delta q_1 - \frac{1}{2r_2}\nabla \tag{5.36}$$

where $\nabla := \Delta_t - \Delta_b$, or

$$\nabla = aT_{tl} - bT_{bl} - \left( \int_0^1 \frac{T_t^0(\varphi_t)}{K_{nt}} d\varphi_t - \int_0^1 \frac{T_b^0(\varphi_b)}{K_{nb}} d\varphi_b \right). \tag{5.37}$$

Assuming $K_{nt} \approx K_{nb}$, since $T_t^0(\varphi_t) = T_b^0(\varphi_b)$, the term in brackets on the right-hand side of (5.37) is zero. Therefore, taking into account (5.16) and (5.35), equation (5.37) can be solved to obtain the following formula:

$$\nabla = \frac{2ab}{K_n r_1(a+b)}\tau_{in} + \frac{a-b}{K_n(a+b)}\Lambda. \tag{5.38}$$

Equation (5.36) is the pseudo-kinematic model for the case of high pretension within the tendons. The second term on the right of (5.38), in fact, adjusts the gap between the ascending and the descending branch of the backlash (*i.e.* the backlash width).

# References

[1] J. K. S. Gary Guthart, "The Intuitive™ telesurgery system: Overview and application.," in *IEEE International Conference on Robotics and Automation*, pp. 618–621, IEEE, 2000.

[2] B. Hannaford, J. Rosen, D. W. Friedman, H. King, P. Roan, L. Cheng, D. Glozman, J. Ma, S. N. Kosari, and L. White, "Raven-II: an open platform for surgical robotics research," *IEEE Transactions on Biomedical Engineering*, vol. 60, no. 4, pp. 954–959, 2013.

[3] R. Kang, Y. Guo, L. Chen, D. T. B. III, and J. S. Dai, "Design of a pneumatic muscle based continuum robot with embedded tendons," *IEEE/ASME Transactions on Mechatronics*, vol. 22, pp. 751–761, April 2017.

[4] M. Grossard, J. Martin, and G. F. D. C. Pacheco, "Control-oriented design and robust decentralized control of the cea dexterous robot hand," *IEEE/ASME Transactions on Mechatronics*, vol. 20, pp. 1809–1821, Aug 2015.

[5] Y. H. Kim, Y. J. Park, H. In, C. W. Jeong, and K. J. Cho, "Design concept of hybrid instrument for laparoscopic surgery and its verification using scale model test," *IEEE/ASME Transactions on Mechatronics*, vol. 21, pp. 142–153, Feb 2016.

[6] V. Hayward and J. M. Cruz-Hernández, "Parameter sensitivity analysis for design and control of tendon transmissions," in *Experimental Robotics IV*, pp. 239–252, Springer, 1997.

[7] J. K. Salisbury and J. J. Craig, "Articulated hands: Force control and kinematic issues," *The International Journal of Robotics Research*, vol. 1, no. 1, pp. 4–17, 1982.

[8] M. Haghighipanah, Y. Li, M. Miyasaka, and B. Hannaford, "Improving position precision of a servo-controlled elastic cable driven surgical robot using unscented Kalman filter," in *International Conference on Intelligent Robots and Systems (IROS)*, pp. 2030–2036, IEEE, 2015.

[9] M. Haghighipanah, M. Miyasaka, Y. Li, and B. Hannaford, "Unscented Kalman filter and 3D vision to improve cable driven surgical robot joint angle estimation," in *IEEE*

*International Conference on Robotics and Automation (ICRA)*, pp. 4135–4142, IEEE, 2016.

[10] B. Kehoe, G. Kahn, J. Mahler, J. Kim, A. Lee, A. Lee, K. Nakagawa, S. Patil, W. D. Boyd, P. Abbeel, *et al.*, "Autonomous multilateral debridement with the Raven surgical robot," in *Robotics and Automation (ICRA), 2014 IEEE International Conference on*, pp. 1432–1439, IEEE, 2014.

[11] Y. Li, M. Miyasaka, M. Haghighipanah, and L. C. B. Hannaford, "Dynamic modeling of cable driven elongated surgical instruments for sensorless grip force estimation," in *2016 IEEE International Conference on Robotics and Automation (ICRA)*, pp. 4128–4134, IEEE, 2016.

[12] Y. Li and B. Hannaford, "Gaussian process regression for sensorless grip force estimation of cable-driven elongated surgical instruments," *IEEE Robotics and Automation Letters*, vol. 2, no. 3, pp. 1312–1319, 2017.

[13] S. McKinley, A. Garg, S. Sen, D. V. Gealy, J. P. McKinley, Y. Jen, and K. Goldberg, "Autonomous multilateral surgical tumor resection with interchangeable instrument mounts and fluid injection device," in *IEEE International Conference on Robotics and Automation (ICRA)*, IEEE, 2016.

[14] A. Murali, S. Sen, B. Kehoe, A. Garg, S. McFarland, S. Patil, W. D. Boyd, S. Lim, P. Abbeel, and K. Goldberg, "Learning by observation for surgical subtasks: Multilateral cutting of 3D viscoelastic and 2D orthotropic tissue phantoms," in *IEEE International Conference on Robotics and Automation (ICRA)*, pp. 1202–1209, IEEE, 2015.

[15] S. Sen, A. Garg, D. Gealy, S. McKinley, Y. Jen, and K. Goldberg, "Automating multi-throw multilateral surgical suturing with a mechanical needle guide and sequential convex optimization," in *IEEE International Conference on Robotics and Automation*, pp. 4178–4185, 2016.

[16] A. Talasaz, A. L. Trejos, S. P. H. Bassan, and R. V. Patel, "A dual-arm 7-degrees-of-freedom haptics-enabled teleoperation test bed for minimally invasive surgery," *ASME Journal of Medical Devices*, vol. 8, no. 4, p. 041004, 2014.

[17] F. Anooshahpour, I. G. Polushin, and R. V. Patel, "Quasi-static modeling of the da Vinci instrument," in *IEEE/RSJ International Conference on Intelligent Robots and Systems (IROS)*, pp. 1308–1313, IEEE, 2014.

[18] F. Anooshahpour, I. G. Polushin, and R. V. Patel, "Classical Preisach model of hysteretic behavior in a da Vinci instrument," in *Advanced Intelligent Mechatronics (AIM), 2016 IEEE International Conference on*, pp. 1392–1397, IEEE, 2016.

[19] F. Anooshahpour, I. G. Polushin, and R. V. Patel, "Tissue compliance determination using da Vinci instrument," in *IEEE International Conference on Robotics and Automation (ICRA)*, pp. 5344–5349, IEEE, 2015.

[20] Intuitive Surgical, Inc., *EndoWrist: Instrument and Accessory Catalog*, July 2011.

[21] K. L. Johnson, *Contact Mechanics*. Cambridge University Press, 1987.

[22] D. Kim, "Dynamic modeling of belt drives using the elastic/perfectly-plastic friction law," Master's thesis, Georgia Institute of Technology, 2009.

[23] L. Kongand and R. G. Parker, "Microslip friction in flat belt drives," *Proceedings of the Institution of Mechanical Engineers, Part C: Journal of Mechanical Engineering Science*, vol. 219, no. 10, pp. 1097–1106, 2005.

[24] M. J. Leamy and T. M. Wasfy, "Analysis of belt-driven mechanics using a creep-rate-dependent friction law," *Journal of Applied Mechanics*, vol. 69, no. 6, pp. 763–771, 2002.

[25] D. G. Alciatore and A. E. Traver, "Multipulley belt drive mechanics: creep theory vs shear theory," *Journal of Mechanical Design*, vol. 117, no. 4, pp. 506–511, 1995.

[26] S. E. Bechtel, S. Vohra, K. I. Jacob, and C. D. Carlson, "The stretching and slipping of belts and fibers on pulleys," *Journal of Applied Mechanics*, vol. 67, no. 1, pp. 197–206, 2000.

[27] M. Kaneko, M. Wada, H. Maekawa, and K. Tanie, "A new consideration on tendon-tension control system of robot hands," in *IEEE International Conference on Robotics and Automation (ICRA)*, pp. 1028–1033, IEEE, 1991.

[28] D. G. Lowe, "Distinctive image features from scale-invariant keypoints," *International Journal of Computer Vision*, vol. 60, no. 2, pp. 91–110, 2004.

[29] J. Oh, B. Drincic, and D. S. Bernstein, "Nonlinear feedback models of hysteresis," *IEEE Control Systems*, vol. 29, no. 1, pp. 100–119, 2009.

[30] P. Guillaume, J. Schoukens, R. Pintelon, and I. Kollar, "Crest-factor minimization using nonlinear Chebyshev approximation methods," *IEEE Transactions on Instrumentation and Measurement*, vol. 40, no. 6, pp. 982–989, 1991.

# Chapter 6

# A Motion Transmission Model for Multi-DOF Tendon-Driven Mechanisms with Hysteresis and Coupling: Application to a da Vinci® Instrument

I n Chapter 5, a novel motion transmission model was developed for the case of one degree-of-freedom (DOF) tendon-driven mechanism in a quasi-static condition. In this chapter, an extension of this model is proposed that allows for estimation of angular displacements in multi-DOF tendon-driven devices while special attention is given to the coupling effect between DOFs. The proposed model consists of the conventional coupling matrix and a novel elongation matrix which compensates for the coupled hysteretic effect. The model is applied to the problem of position estimation in three DOFs (one pitch and two grasping DOFs) of a da Vinci® surgical instrument. As a further extension, a preliminary dynamic model is also suggested to deal with high-frequency inputs. Both models are validated through extensive experiments. According to the experimental results obtained, the proposed quasi-static model can describe the transmission behavior with goodness-of-fit of 76-92 per cent, and the estimates are improved by 35-72 per cent in terms of the RMSE for the proposed dynamic model as compared to the conventional rigid

model.

## 6.1 Introduction

Tendon-based transmissions, in the form of tendon-pulley or tendon-sheath mechanisms, have been widely used in Minimally Invasive Surgery (MIS) as well as in Robot Assisted Minimally Invasive Surgery (RAMIS). In particular, tendon-pulley based mechanisms exhibit significant hysteretic behavior, induced mainly by tendons' frictions and compliance characteristics. An example of such mechanisms is a da Vinci EndoWrist® instrument. The instrument consists of a set of tendon-pulley systems tightly packed into a casing with a narrow shaft, which bears a 3-DOF wrist mechanism at its remote end. The instrument's internal frictions and tendons' compliance give rise to hysteretic motion behavior even when the tip is not in contact with the environment. Additional hysteresis is generated by coupling between different DOFs of the instrument. Such a complex behavior results in significant errors in motion control for da Vinci and other tendon-pulley based serial surgical manipulators such as RAVEN II [1].

In many previous research works, *e.g.* [2–5], tendons were considered as either elastic, viscoelastic, or rigid elements, the positions of all joints were assumed known (measurable), and the nonlinearities of the transmission were compensated by the controller. In surgical applications, however, the positions of the remote joints of MIS and RAMIS systems typically can not be directly measured due to difficulties in sensors implementation; as a result, the hysteresis presents a substantial problem. On the other hand, the hysteretic motion behavior of the cable-driven mechanisms in the absence of external load cannot be described using pure elastic or rigid elements. In [6], a tendon-multipulley transmission system was lumped into an input and output pulleys, the tendons were replaced with parallel interconnections of two exponential springs and two linear dampers, and the frictions are considered point contact resistive forces at the pulleys' axes. The approach was adopted for position control of the RAVEN II surgical robot [1], where the Unscented Kalman Filter (UKF) was used to estimate the parameters and the states of the model. In [7], a stereo vision data was fed into the UKF to improve the accuracy of motion control algorithm. In [8], the above model was used to estimate the gripping force of the tendon-pulley RAVEN II instrument.

(a)
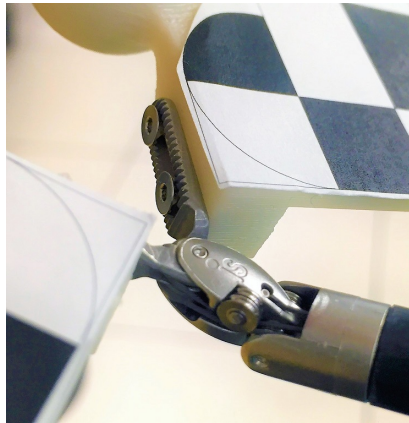


(b)
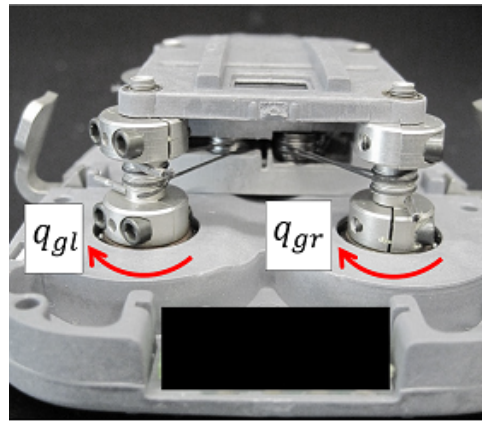


(c)
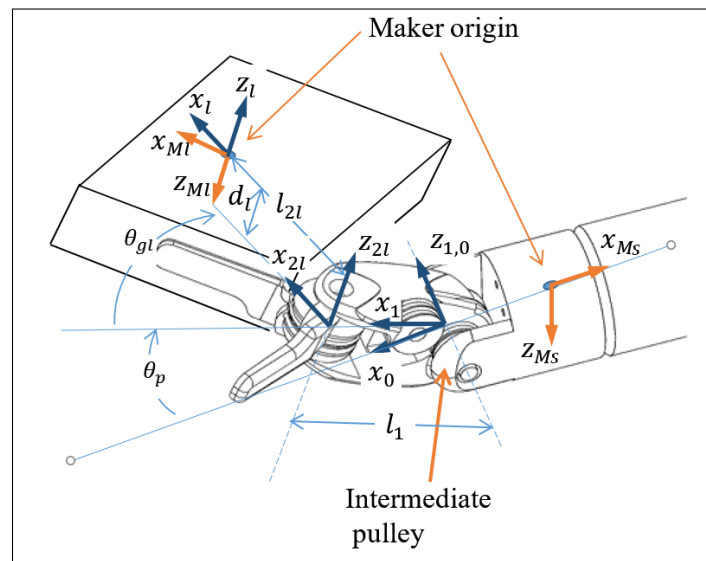


(d)

Figure 6.1: The case study: a) the da Vinci EndoWrist® instrument - overall view; b) wrist mechanism with markers; c) input pulleys at the actuator side, grasping pulleys are visible, with roll and pitch pulleys behind them; and d) the coordinate frames assigned to the wrist mechanism of the instrument.

The models given in [1, 6–8] are more focused on compensating the dynamic nonlinearities while the quasi-static hysteretic behavior is neither considered nor discussed.

There is another set of studies which attribute the nonlinear behavior of tendon-pulley mechanisms to tendon and pulley frictional interaction which results in distributed friction and tension along the tendon. Historically, this has been used in *belt-drive mechanics* to explain different aspects of power transmission in the industrial belt-pulley systems, especially those that operate at constant speed [9, 10]. The *classic creep theory* [11] used in belt mechanics assumes the existence of a stick and a slip zone on every pulley in the system. In the slip zone, the friction grows exponentially along the tendon, while in the stick zone, zero interaction is assumed [12]. In robotic applications, there are some studies that utilized the same distributed friction approach to explain tendon-pulley transmission. In [13], in order to estimate the transmission stiffness, two slip zones and one stick zone is assumed on the surface of the driven pulley in a capstan drive. This approach is followed by a number of similar studies such as [14] which is focused on the motion transmission error due to tendon slip in a capstan drive.

In [15], authors considered a fixed curved surface for each forward and return tendon in a 1 DOF tendon-multipulley transmission to replicate the overall elastic creep in the system (see Figure 6.2). The model was initially suggested for the force transmission based on the similarity between the force transmission behavior of the da Vinci Instrument and that of a typical tendon-sheath system. Also, a sensorless method for estimation of environmental stiffness using a da Vinci instrument was developed based on the same assumptions [16].

The main contribution of this chapter is as follows.

a) A new formula for modelling of the hysteretic coupling effect in multi-DOF tendon-pulley systems is suggested based on the previously developed tendon-surface technique. The proposed formula consists of two components: i) a conventional rigid transmission term; and ii) an elongation compensation term. The conventional rigid term models geometrical properties of the transmission, and the elongation compensation term describes the hysteretic behavior in the transmission.

b) A preliminary dynamical model is proposed to describe the high frequency effects in the transmission.

c) The models are applied to three DOFs of the EndoWrist® instrument as a case study, and validated extensively through experiments. The results demonstrate close agreement between the displacement estimates given by the proposed model and the camera-based measurements.

The chapter is organized as follows. Section 6.2 presents the proposed model for the motion transmission in multi-DOF tendon-pulley systems. Section 6.3 describes the EndoWrist® instrument used as a case study. Section 6.4 provides the identification results, and the experimental validations. A preliminary dynamical model is discussed in Section 6.5 to describe the high-frequency effects in the transmission. Finally, Section 6.6 concludes this chapter.

## 6.2   Model Development

In our modeling approach, two imaginary curved surfaces are introduced between the input and the output pulleys in order to replicate tendon elastic creep on the surface of all pulleys within the system (See Figure 6.2). For a single tendon with length $L > 0$ on a surface with radius of curvature $R > 0$ and Coulomb friction constant $\mu > 0$, application of a unidirectional input force $F$ results in two distinct slip and stick zones on the surface. Along the slip zone, the following differential equation describes the change in tension $dT(x)$,

$$dT(x) = -\frac{\mu T(x)}{R}\operatorname{sgn}(v)dx, \tag{6.1}$$

where $\operatorname{sgn}(v)$ represents the direction of the impending motion. In the stick zone, tension remains unchanged $T^0(x)$. The formula for elementary elongation, on the other hand, can be written in the form

$$d\Delta(x) = \frac{T(x) - T^0(x)}{EA}dx, \tag{6.2}$$

where $d\Delta(x)$ is the change of length of the infinitesimal segment of tendon $dx$, $E$ is the tendon modulus of elasticity, and $A$ is the cross section area of the tendon.

Assuming $I)$ tension propagation is immediate along the tendons as the direction of rotation changes (*e.g.* no stick zone), and $II)$ the pretension is zero, formula (6.1) implies that tension distribution $T(x)$ along the tendon is given by $T(x) = Fe^{-\frac{\mu x}{R}\operatorname{sgn}(v)}$. Also, the total
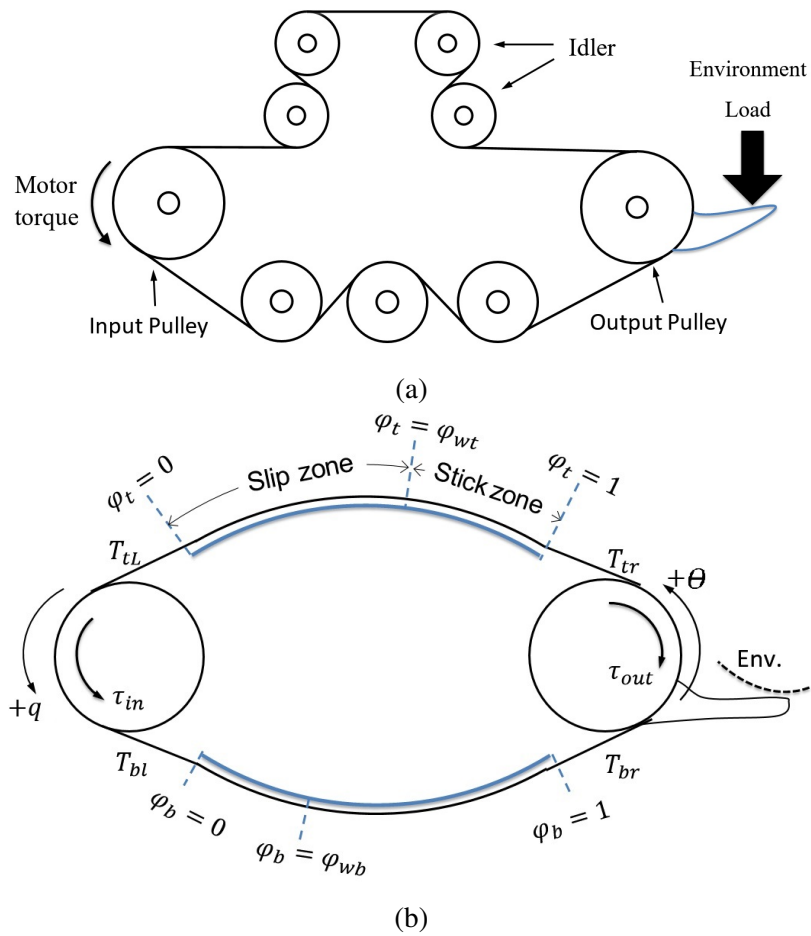
Figure 6.2: (a) A schematic overview of a single DOF tendon-multipulley transmission and (b) the tendon-surface based model to represent a one-DOF tendon-multipulley system.

tendon elongation $\Delta$ due to the external loading $F$ can be described by

$$\Delta = \frac{1}{EA} \int_0^L T(x)dx = \frac{F \operatorname{sgn}(v)}{K_n \eta}(1 - e^{-\eta \operatorname{sgn}(v)}), \tag{6.3}$$

where $\eta = \mu L/R$ is the dimensionless *friction-bending* parameter.

In the case of a dual tendon-surface system of Figure 6.2(b), the elongation of the top and the bottom tendon can be represented by the following formula:

$$\Delta_i = T_{il} \frac{\operatorname{sgn}(\dot{q}_1)}{K_n \eta} M_i \tag{6.4}$$

where $i \in \{t, b\}$ denotes the top and the bottom tendon in Figure 6.2(b), respectively, $T_{il}$ is the tension in the left-end side of the $i$-th tendon, $M_t = 1 - e^{-\eta \operatorname{sgn}(\dot{q}_1)}$ and $M_b = e^{\eta \operatorname{sgn}(\dot{q}_1)} - 1$. Considering the geometry of the dual tendon-surface system of Figure 6.2(b), we obtain the following formulas that relate the rotation of the output pulley $\Delta\theta$ to the rotation of the input pulley $\Delta q$ and the elongation of the top and the bottom tendons, respectively:

$$\Delta\theta = \frac{r_1}{r_2}\Delta q - \frac{1}{r_2}\Delta_t, \quad \Delta\theta = \frac{r_1}{r_2}\Delta q + \frac{1}{r_2}\Delta_b, \tag{6.5}$$

where $r_1$ and $r_2$ are the radii of the input and the output pulleys, respectively. Assuming power is only transmitted through the tendon which is tightened by the input pulley[1], $\Delta\theta$ is calculated by switching in between of the two equations given in (6.5),

$$\Delta\theta = S(\dot{q})\alpha_t \tau_{in} + (1 - S(\dot{q}))\alpha_b \tau_{in} + \beta \Delta q, \tag{6.6}$$

where the switching function $S(x)$ is defined as

$$S(x) := \begin{cases} 1 & x > 0, \\ 0 & x < 0, \end{cases} \tag{6.7}$$

and $\alpha_t := \frac{1-e^{-\eta_t}}{r_1 r_2 \eta_t K_{nt}}$, $\alpha_b := \frac{1-e^{-\eta_b}}{r_1 r_2 \eta_b K_{nb}}$, $\beta := \frac{r_1}{r_2}$ are constant parameters. In deriving (6.6), $T_{tl}$ and $T_{bl}$ are substituted with $\tau_{in}/r1$ and $-\tau_{in}/r1$, respectively, as the low-speed steady-state operating condition requires for the input and output pulleys. Also, to account for

---

[1]This is equivalent to the assumption of zero pretension, *i.e.* $T_i^0(x) = 0$.

possible dissimilarities of the forward and the return tendons' paths in actual tendon-pulley mechanisms, the friction-bending parameter $\eta$ and the stiffness $K_n$ may be different for the top and the bottom tendons in Figure 6.2(b). Formula (6.6) is the pseudo-kinematic relation between the input displacement $\Delta q$, the output displacement $\Delta \theta$, and the input torque $\tau_{in}$. If the transmission is rigid (i.e. $K_n \to \infty$), equation (6.6) reduces to $\Delta \theta = \beta \Delta q$, which is the conventional kinematic formulation for mechanisms of this type. If friction approaches zero, *i.e.* $\eta \to 0$, the tendon acts as a nonlinear spring which switches off when contracted, while maintaining constant tension along its length when stretched.

For a general $n$-DOF mechanism, equation (6.6) can be generalized as follows:

$$\boldsymbol{\Theta} = \boldsymbol{BQ} + \boldsymbol{AS}\tau_{in}, \tag{6.8}$$

where $\boldsymbol{\Theta} := [\Delta \theta_1, \Delta \theta_2, \ldots, \Delta \theta_n]^T$ is the vector of the output angular displacements, $\boldsymbol{Q} := [\Delta q_1, \Delta q_2, \ldots, \Delta q_n]^T$ the vector of input motor/pulley displacements, and $\boldsymbol{\tau_{in}} := [\tau_{in-1}, \tau_{in-2}, \ldots, \tau_{in-n}]^T$ the vector of the input torques commanded to the actuators, respectively; $\Delta \theta := \theta(t) - \theta_0$ is the relative change of angular displacement from its initial value at $\theta_0 = \theta(t_0)$, and $\Delta q := q(t) - q_0$. The matrix of rigid transmission, $\boldsymbol{B} \in \mathbb{R}^{n \times n}$, is defined as

$$\boldsymbol{B} = \begin{bmatrix} \beta_1 & \beta_{c12} & \ldots & \beta_{c1n} \\ \beta_{c21} & \beta_2 & \ldots & \beta_{c2n} \\ & & \vdots & \\ \beta_{cn1} & \beta_{cn2} & \ldots & \beta_n \end{bmatrix}, \tag{6.9}$$

where the off-diagonal elements $\beta_{cij}$ are the rigid coupling parameters representing the effect of motion in $i$-th DOF on $j$-th DOF of the system. Also, $\boldsymbol{A} \in \mathbb{R}^{n \times 2n}$ is the elongation matrix, or the matrix of hysteretic transmission,

$$\boldsymbol{A} = \begin{bmatrix} \alpha_{t1} & \alpha_{b1} & \alpha_{tc12} & \alpha_{bc12} & \ldots & \alpha_{tc1n} & \alpha_{bc1n} \\ \alpha_{tc21} & \alpha_{bc21} & \alpha_{t2} & \alpha_{b2} & \ldots & \alpha_{tc2n} & \alpha_{bc2n} \\ & & \vdots & & & & \\ \alpha_{tcn1} & \alpha_{bcn1} & \alpha_{tcn2} & \alpha_{bcn2} & \ldots & \alpha_{tn} & \alpha_{bn} \end{bmatrix}, \tag{6.10}$$

where the pairs $(\alpha_{ti}, \alpha_{bi})$ are the elongation parameters for the $i$th DOF as introduced in (6.6), and the pairs $(\alpha_{tcij}, \alpha_{bcij})$ represent the nonrigid coupling parameters that account for the hysteretic effect of the $i$-th DOF on the $j$-th DOF of the system. Matrices $\boldsymbol{B}$ and

$\boldsymbol{A}$ are not necessarily symmetrical. The coupling elements in these matrices depend on the specific structure of the system. In addition, $\boldsymbol{S}_{2n \times n}$ is the switching matrix defined as follows,

$$
\boldsymbol{S} := \begin{bmatrix}
S(\dot{q}_1) & 0 & 0 \\
1 - S(\dot{q}_1) & 0 & 0 \\
0 & S(\dot{q}_2) & 0 \\
0 & 1 - S(\dot{q}_2) & \cdots & 0 \\
\vdots & \vdots & \\
0 & 0 & S(\dot{q}_n) \\
0 & 0 & 1 - S(\dot{q}_n)
\end{bmatrix} .
$$

If the tendons are considered inelastic, then only the first term on the right-hand side of (6.8) represents the transmission, *i.e.*, $\boldsymbol{\Theta} = \boldsymbol{BQ}$, which is the conventional form of coupling matrix used in the literature [1, 17].

## 6.3 Case Study: The da Vinci® Surgical Instrument

In this study, we choose an EndoWrist® instrument, a Cadiere Forceps [18], as a test bed for validation of the proposed multi-DOF motion transmission model (6.8). The choice of a da Vinci instrument for the model validation is made due to the fact that it is a commercially available tendon-pulley mechanism which, due to the fine production, is likely to demonstrate similar behavior from instrument to instrument. As shown in Figure 6.1, four input pulleys are located at the proximal/actuator side of the instrument. Three of these pulleys are connected via tendons to the three DOF wrist mechanism at the distal end of the instrument, while the fourth pulley is used for rolling the instrument's shaft. The roll DOF is not addressed in this study as its coupling effect is negligible. The wrist mechanism, shown in Figure 6.1(b), has one pitch DOF and two independent grasping DOFs. There is a strong mechanical coupling between the pitch and grasping motions, specifically, the rotation of the former DOF induces a motion of the latter. In order to track the motion of the instrument's tip, a MicronTracker™ camera is used (Figure 6.3). The camera is designed to detect and track specific markers by utilizing stereoscopic vision in real time. The update rate of the camera is approximately 30 Hz. The Root-Mean-Square (RMS) of the calibration error is 0.25mm for a single target point, while lighting conditions (*e.g.*
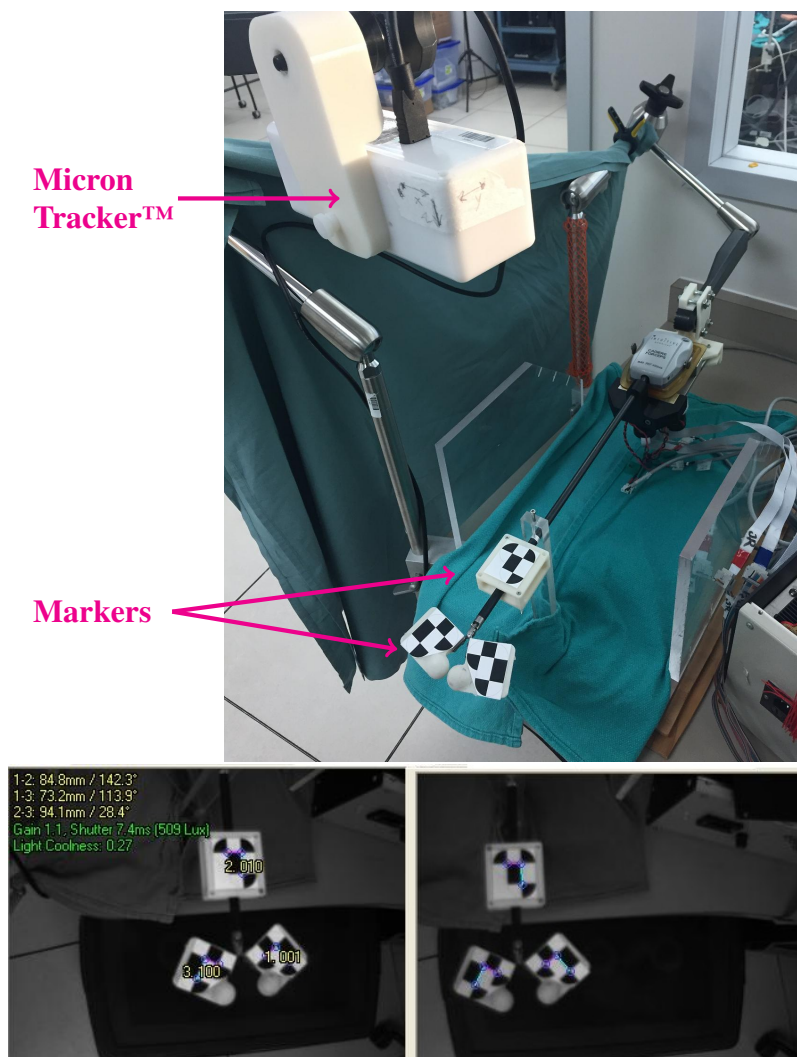
Figure 6.3:  Experimental setup, An EndoWrist® instrument with markers and a Micron Tracker Camera (top), left and right camera view (bottom)

light coolness) may contribute $0.1\%$ to $0.25\%$ of measurement error in Z direction. Error due to measurement jitter is 0.22 mm (RMS) for a moving target [19]. The camera assigns a coordinate frame to each marker on the instrument and returns the origin and the rotation matrix of that frame relative to the camera's fixed frame. The instrument's jaws are equipped with specially designed 3D-printed holders for placement of the markers. Each holder has a finger-like knob to allow the instrument to be used in pick-and-place tasks.

### 6.3.1 Forward and Inverse Kinematics

In order to study the motion transmission characteristics of the da Vinci instrument, the coordinate frames and parameters are assigned to the wrist mechanism as shown in Figure 6.1(d). Parameters and frames related to the right jaw are omitted in the figure, due to their similarity with the left jaw. Frame $\{0\}$ is the global frame representing the fixed shaft. Frame $\{1\}$ is attached to the pitch link of the wrist with $z_1$ aligned with the pitch rotation axis. Frames $\{2l\}$ and $\{l\}$ are attached to the left jaw and are parallel, where the former is placed on the left jaw rotation axis and the latter on the origin of the left marker.

The rotational angles $\theta_p$, $\theta_{gr}$, $\theta_{gl}$ represent the wrist's pitch, the right grasp, and the left grasp angles, respectively. In a similar fashion, $q_p$, $q_{gr}$ and $q_{gl}$ represent the displacements of the corresponding motors at the actuator side. The orientation of $\{l\}$ relative to the base frame can be described by a matrix ${}^0R_l(\boldsymbol{\Theta})$ as follows,

$$
{}^0R_l(\boldsymbol{\Theta}) =
\begin{bmatrix}
\cos\theta_p \cos\theta_{gl} & -\cos\theta_p \sin\theta_{gl} & -\sin\theta_p \\
\sin\theta_p \cos\theta_{gl} & -\sin\theta_p \sin\theta_{gl} & \cos\theta_p \\
-\sin\theta_{gl} & -\cos\theta_{gl} & 0
\end{bmatrix},
\tag{6.11}
$$

and the position of the marker's origin relative to the base frame is given by ${}^0P_l(\boldsymbol{\Theta})$,

$$
{}^0P_l(\boldsymbol{\Theta}) =
\begin{bmatrix}
l_1 \cos\theta_p - d_l \sin\theta_p + l_{2l} \cos\theta_p \cos\theta_{gl} \\
l_1 \sin\theta_p + d_l \cos\theta_p + l_{2l} \sin\theta_p \cos\theta_{gl} \\
-l_{2l} \sin\theta_{gl}
\end{bmatrix},
\tag{6.12}
$$

where $l_1$ is the length of the common normal between $z_1$ and $z_2$, $l_{2l}$ is the distance of frame

$\{l\}$ from the rotation axis of the left and right jaws and $d_l$ is the line offset along $z_{2l}$ from plane $xy$ of frame $\{l\}$.

The inverse kinematics equation of the wrist mechanism is solved for $\theta_p$ and $\theta_{gl}$ as follows. MicronTracker™ firmware returns the rotation matrices $^{Cam}R_{Ml}$ and $^{Cam}R_{Ms}$ as for orientation of the markers on the left jaw and shaft of the instrument. The numerical equivalent of $^0R_l$ in equation (6.11) then can be found using the following formula,

$$^0R_l =\, ^0R_{Ms}\, ^{Ms}R_{Cam}\, ^{Cam}R_{Ml}\, ^{Ml}R_l, \tag{6.13}$$

where $^0R_{Ms}$ and $^lR_{Ml}$ are the orientations of the markers' frame relative to the base and the left jaw's frames, respectively. The parameters are calculated for given known angles. From $^0R_l$, the values of $\theta_{gl}$ and $\theta_p$ can be uniquely calculated by utilizing some basic trigonometric formulas, *i.e.*, $\theta = \arctan2\left(\sin(\theta), \cos(\theta)\right)$. The resulting $\theta_p$ is noisier than $\theta_{gr}$ and $\theta_{gl}$ as can be seen in Figure 6.4. This happens for two reasons. First, no dedicated marker is placed on the pitch link due to the size limitations; instead, its position is indirectly calculated based on the other two markers. Second, the motion of the pitch link is toward and away from the camera. As a result, the measurements of the pitch depend on the camera depth measurement accuracy. The camera used in this study has lower accuracy in depth measurements in comparison with that of the planar measurements.

### 6.3.2 Motion Transmission Model for the da Vinci® instrument

In the da Vinci instrument, due to its unique design, a one-way coupling is observed between its pitch and grasp DOFs. Upon rotation of the pitch link around its axis $z_1$, the grasp's tendon wraps around the intermediate pulleys as shown in Figures 6.1(b) and (d), resulting in a secondary rotation in the jaws. The reverse coupling is however negligible, i.e., moving the jaws does not induce a pitch motion in the wrist. As an illustration of this phenomenon, Figure 6.4 shows the case when a 0.01 Hz sinusoidal pitch rotation is commanded while the grasp DOFs are set free.

Let $\Theta = [\Delta\theta_p, \Delta\theta_{gr}, \Delta\theta_{gl}]^T$ be the vector of output angular displacements. The following

(a) Marker's motion in Cartesian space



(b) Pitch and induced grasping rotations vs. time



(c) Output rotations vs. input pitch
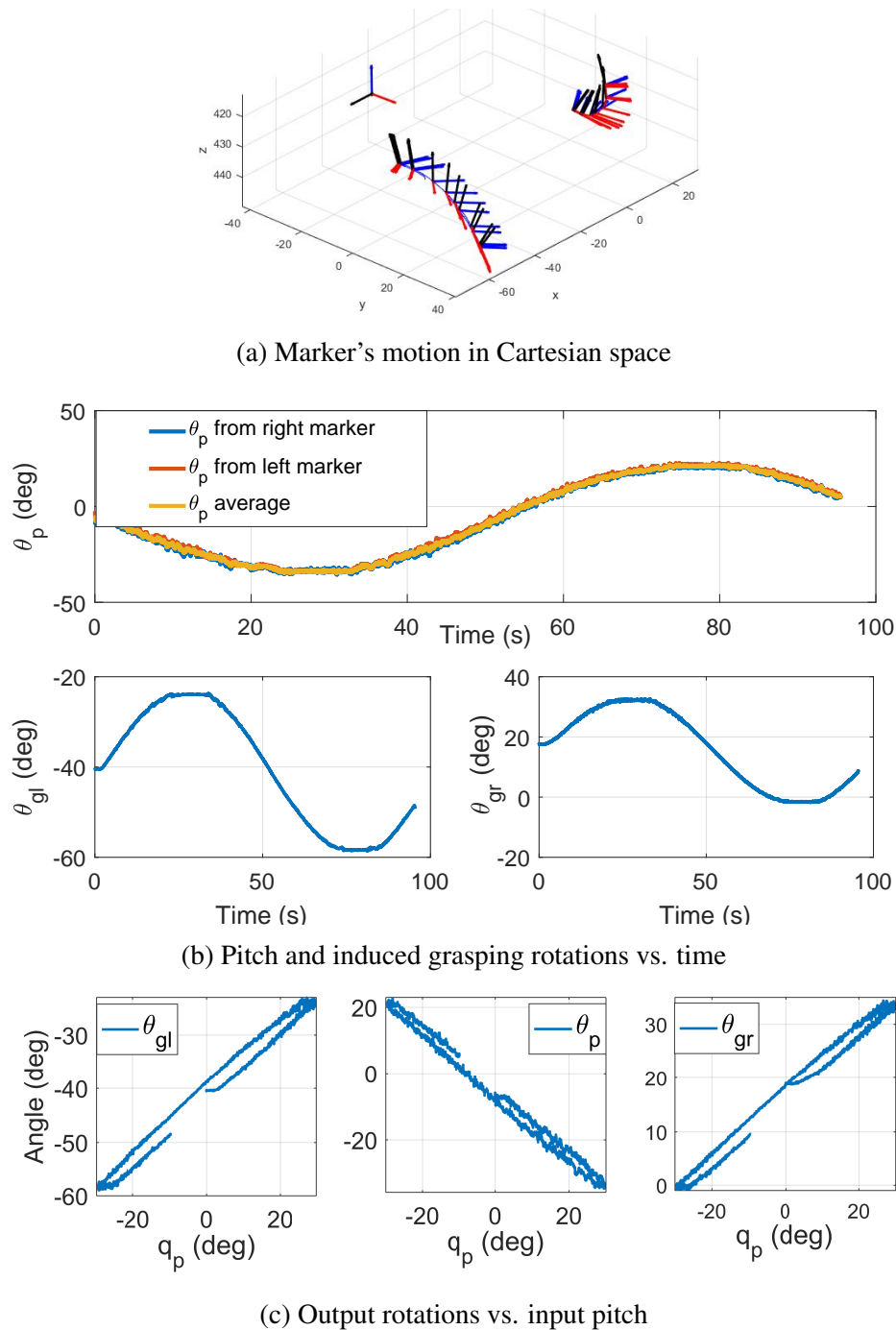
Figure 6.4: A sinusoidal command to the pitch DOF ($q_p$) of the instrument while grasping DOFs ($q_{gr}$ and $q_{gl}$) are set free. A coupling effect with hysteretic behavior can be observed in the right and left grasps ($\theta_{gl}$ and $\theta_{gr}$). Here the frequency of command is $0.01$ Hz and the amplitude is $30$ degrees.
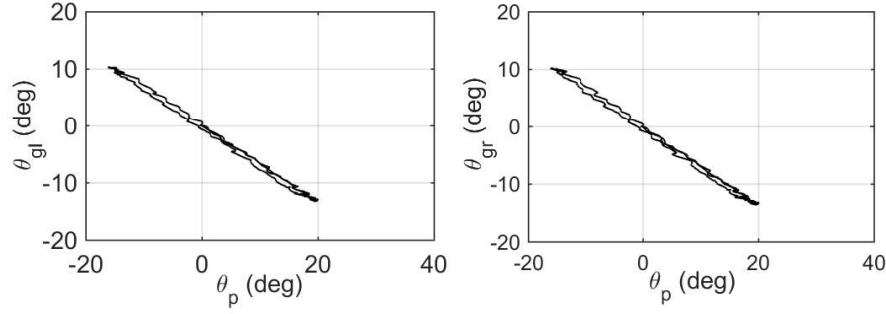
Figure 6.5: Response of $\theta_{gr}$ (left) and $\theta_{gl}$ (right) to a sinusoidal signal $\theta_p(t) = 20 \cos{(0.01t)}$ deg. The hysteresis effect is negligible.

matrix describes the rigid transmission,

$$
\boldsymbol{B} = \begin{bmatrix} \beta_p & 0 & 0 \\ \beta_{cgr} & \beta_{gr} & 0 \\ \beta_{cgl} & 0 & \beta_{gl} \end{bmatrix} = \begin{bmatrix} \frac{r_{mp}}{r_p} & 0 & 0 \\ K_r \frac{r_{mp}}{r_p} & \frac{r_{mgr}}{r_{gr}} & 0 \\ K_l \frac{r_{mp}}{r_p} & 0 & \frac{r_{mgl}}{r_{gl}} \end{bmatrix}, \tag{6.14}
$$

where $K_r = r_{int}/r_{gr}$, $K_l = r_{int}/r_{gl}$, and $r_{mi}$ are the radii of the input (motor) pulleys, $i \in \{p, gr, gl\}$. Also, $r_p$ is the radius of pulley-like groove on the pitch link, $r_{int}$ is the radius of the intermediate pulley, which shares the same joint axis with the pitch link, and $r_{gr}$ and $r_{gl}$ are the radii of the pulley-like grooves on the right and left jaws, respectively. The specific parameters of the matrix $\boldsymbol{B}$, given on the right-hand side of (6.14), can be found from the geometry of the pulleys assuming inelastic tendons, as reported in [17].

The induced grasping motion also exhibit hysteresis due to the coupling (see for example Figure 6.4(c)). The elongation compensation matrix $\boldsymbol{A}$ describes the hysteresis effect in the coupling, as given below,

$$
\boldsymbol{A} = \begin{bmatrix} \alpha_{tp} & \alpha_{bp} & 0 & 0 & 0 & 0 \\ \alpha_{tcyr} & \alpha_{bcyr} & \alpha_{tyr} & \alpha_{byl} & 0 & 0 \\ \alpha_{tcyl} & \alpha_{bcyl} & 0 & 0 & \alpha_{tyl} & \alpha_{byl} \end{bmatrix}. \tag{6.15}
$$

According to (6.14), the induced grasp motion is proportional to the wrist pitch with co-efficients $K_r$ and $K_l$ for the left and right grasps, respectively. Therefore, one possibility is to observe the same relation between the corresponding elements in the elongation matrix. That is, no significant hysteresis effect is expected between the output angles. This

is confirmed through experiments, as shown in Figure 6.5. Specifically, the relationship between $\theta_p$ and $\theta_{gl}$ is shown in Figure 6.5 (left), and the relationship between $\theta_p$ and $\theta_{gr}$ in Figure 6.5 (right), where $\theta_p$ is a sinusoidal command with frequency of $0.1\ Hz$ and an amplitude of 20 degrees. In both cases, the hysteresis effects are negligible. Therefore, the following relationships is considered between the elements of (6.15),

$$
\begin{aligned}
(\alpha_{tcyr}, \alpha_{bcyr}) &= K_r \cdot (\alpha_{tp}, \alpha_{bp}), \\
(\alpha_{tcyl}, \alpha_{bcyl}) &= K_l \cdot (\alpha_{tp}, \alpha_{bp}).
\end{aligned}
\tag{6.16}
$$

## 6.4 Experimental Results and Model Validation

To perform experimental validations, the EndoWrist® instrument was actuated using three Faulhaber 2642W024CR DC motor-encoders to drive the instrument's input pulleys. The motors were driven using Maxon 4-Q-DC servo amplifiers set to current mode. The closed-loop control for the motors and the camera's coordinate recording were implemented in C++, and the post-processing analysis was performed in MATLAB. To identify the model parameters, 12 experiments were conducted for each DOF using a set of sinusoidal commands with amplitudes of 20, 15, 10, and 7 degrees and frequency of 0.1 Hz. Each experiment was repeated three times for each amplitude value to account for possible non-repeatabilities. For the purpose of parameter optimization, the following cost function was defined,

$$
\text{Maximize: } \sum_{i=1}^{N} \text{GoF}_i,
$$

where $N$ is the number of experiments, and $\text{GoF}_i$ is the goodness-of-fit associated with the i-th experiment, defined as follows,

$$
\text{GoF}_i := 1 - \frac{\|\theta_i - \hat{\theta}_i\|}{\|\hat{\theta}_i - \Sigma_{k=1}^{k=M_i}\hat{\theta}_i(k)/M_i\|},
$$

where $\theta_i$ is the joint angle measured by the camera during the i-th experiment, $\hat{\theta}_i$ is the angle estimate obtained using the proposed model, and $M_i$ is the total number of samples for the i-th experiment. GoF of 1 (100%) corresponds to a perfect fit. To optimize the cost function, a hybrid pattern identification method consisting of the Latin hypercube sam-

(a) Right grasp
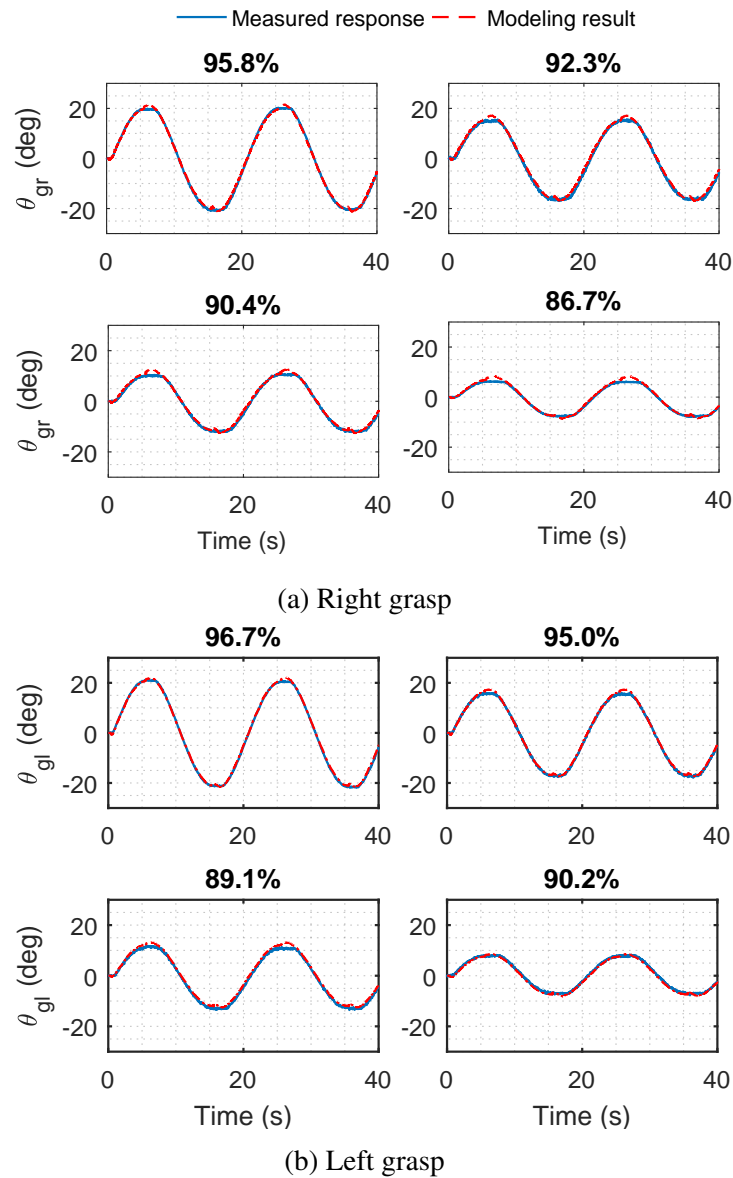
(b) Left grasp

Figure 6.6: Model identification results for the right and left grasp. Four experiments with the desired input amplitudes of 20, 15, 10, and 7 degrees. The percentages show the Goodness-of-Fit associated with the modeling result of each separate experiment.

Table 6.1: Parameter identification results

| Joint | Parameters | GoF |
|---|---|---|
| Yaw (Right) | $\alpha_{1gr} = -1.907, \alpha_{2gr} = -1.054,$ $\beta_{gr} = 1.109$ | Mean = 91.3% Std = 3.78% |
| Yaw (Left) | $\alpha_{1gl} = -1.047, \alpha_{2gl} = -0.541,$ $\beta_{gl} = 1.138$ | Mean = 92.8% Std = 3.68% |
| Pitch | $\alpha_{1p} = -0.424, \alpha_{2p} = -2.828,$ $\beta_p = 0.996$ | Mean = 82.0% Std = 9.64% |
| P-RG | $K_r = 0.674$ | Mean = 76.8% Std = 9.37% |
| P-LG | $K_l = 0.664$ | Mean = 76.9% Std = 11.99% |

pling (LHS) algorithm [20] followed by the nonlinear least squares (NLS) method were used. The LHS was used to generate a set of initial points for NLS, where Levenberg-Marquardt algorithm [21] was used for fine tuning of the parameters. The identified values of the parameters are given in Table 6.1 along with the average GoFs for each joint, where the accuracy of the proposed model is compared with that of the rigid transmission. The angle estimates obtained using the proposed model are also shown in Figure 6.6 for the right and left grasp, and the corresponding hysteresis loops are shown in Figure 6.7. As observed, the angle estimates closely match the rotations measured by the camera. The result also confirms the capability of the proposed model in estimating the hysteresis behavior between the input pulley and the output pulley of the instrument joints. Moreover, Figure 6.8 shows the estimated angle for the pitch and its coupling effect on the right and left grasp. As can be seen from the figure, the coupling is accurately characterized by the proposed model. The minor error observed in this part is mainly due to the camera inaccuracy in depth measurements, as discussed earlier in the previous section. The observed jump at the trajectory extrema is due to the assumption of immediate tension propagation after a direction change. The optimal values of $\beta_i, i = \{gr, gl, p\}$ closely match the actual ratios of the pulleys in the da Vinci® instrument. For instance, as measured for the right jaw, $r_{mgr} = 2.6$ mm and $r_{gr} = 2.4$ mm, resulting in $(r_{mgr}/r_{gr}) = 1.08$ in the da Vinci® instrument versus optimal $\beta_{gr}$ value of 1.109.

(a) Right grasp



(b) Left grasp
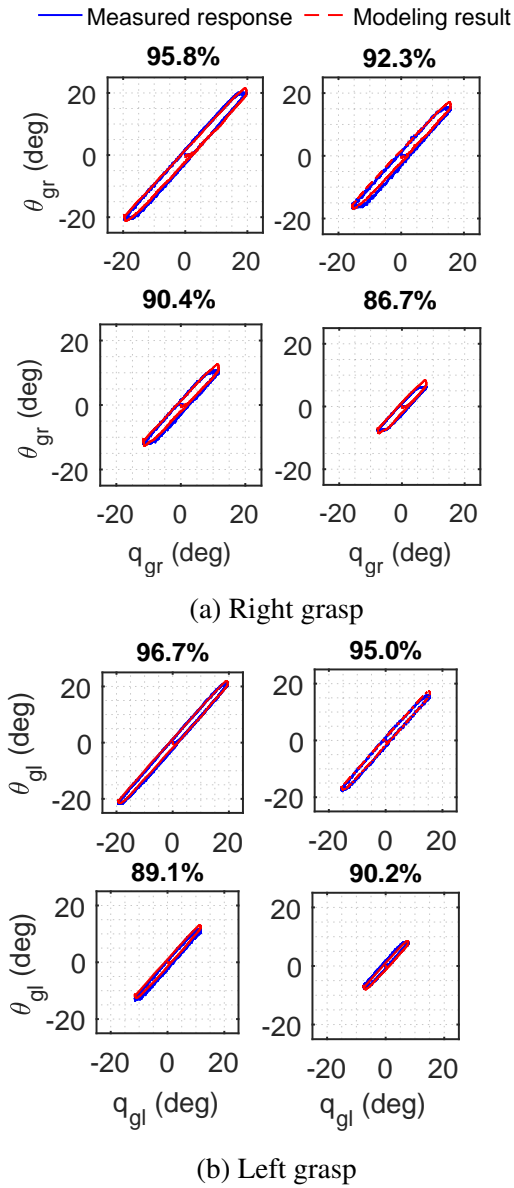
Figure 6.7: Model identified hysteresis in comparison with the system actual hysteresis for four sinusoidal commands with desired input amplitudes of 20, 15, 10, and 7 degrees. The percentages show the Goodness-of-Fit.
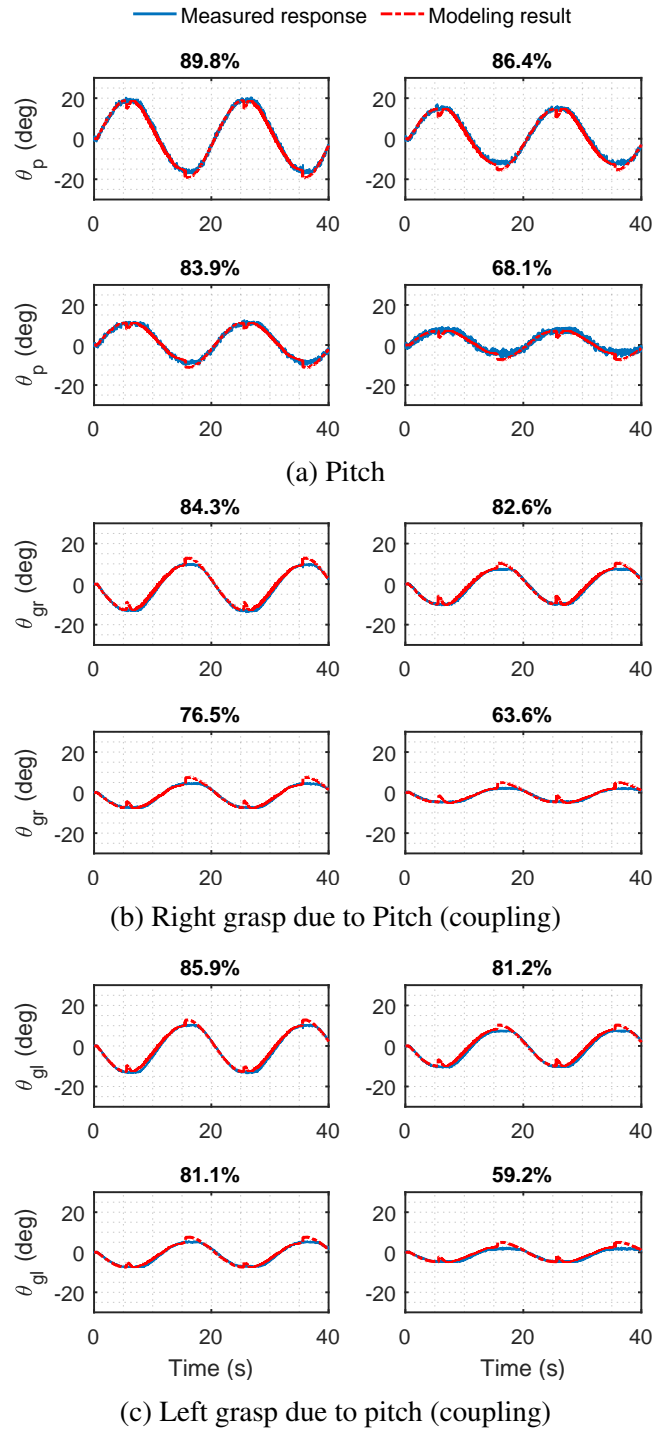
Figure 6.8: Pitch identification results along with the right and left grasp couplings for four sinusoidal commands with desired input amplitude of 20, 15, 10, and 7 degrees. The percentages show the Goodness-Of-Fit associated with the modeling results for each separate experiment.

## 6.5 Dynamic Effects in Motion Transmission - Preliminary Analysis

Figure 6.9 represents an instrument's response to a swept-sine signal to pitch DOF of the instrument with constant amplitude of 10 deg and varying frequencies 0.01, 0.05, 0.1, 0.3, 0.5, 1, 2 and 3 Hz commanded to pitch rotation while the grasp DOFs were set free. As can be seen, the general behavior converges to a fixed loop, as the signal goes from high to low frequencies. The lag in the response however increases for higher frequencies. To discuss the dynamic effects in the transmission, in this section we focus only on the grasp motion. Given the low inertia property of the jaws, the dynamic effect of transmission is dominant in comparison with the inertia contribution. As such, the inertia contribution to the dynamic effects is neglected in this study.

The discrepancy introduced by the increase in frequency can be explained by adding a viscous friction term to (6.8). To discuss the dynamic effect, we first consider the single tendon discussed in Section 6.2. Assuming that the tendons and pulleys are mass-less, the new tension change formula, in the slip zone, can be written as follows

$$dT = -\frac{\mu T}{R}\operatorname{sgn}(v(x))dx - bv(x)dx \tag{6.17}$$

where the term $bv(x)$ equals to the segment's viscous friction per unit length and $b$ is the coefficient of viscous friction. Assuming the velocity of the tendon $v(x) = v$ is similar for all material points of the tendon in the slip zone at any instance of time, one can integrate (6.17) and find the following tension distribution formula,

$$\ln\frac{\frac{\mu\operatorname{sgn}(v)}{R}T(x) + bv}{\frac{\mu\operatorname{sgn}(v)}{R}F + bv} = -\frac{\mu\operatorname{sgn}(v)}{R}x, \tag{6.18}$$

which can be solved to obtain

$$T(x) = e^{-\frac{\mu x}{R}\operatorname{sgn}(v)}F + \frac{b}{\frac{\mu\operatorname{sgn}(v)}{R}}(e^{-\frac{\mu x}{R}\operatorname{sgn}(v)} - 1)v. \tag{6.19}$$

The first and the second term to the right hand side of (6.19) represent the effect of dry friction and the viscous friction on the tension distribution, respectively. The elongation

of the tendon can then be derived according to (6.3), with a similar assumption of zero
pretension and immediate propagation,

$$\Delta = \frac{\text{sgn}(v)}{\eta K_n}(1 - e^{-\eta\,\text{sgn}(v)})F + \frac{bL\,\text{sgn}(v)}{\eta K_n}(\frac{1 - e^{-\eta\,\text{sgn}(v)}}{\eta\,\text{sgn}(v)} - 1)v. \tag{6.20}$$

For the case of dual tendon-surface model shown in Figure 6.2(b), the new elongation
term is added to Eq. (6.6) and results in the following dynamic formula for a one DOF
mechanism,

$$\Delta\theta = S(\dot{q})(\alpha_t\tau_{in} + \gamma_t v) + (1 - S(\dot{q}))(\alpha_b\tau_{in} + \gamma_b v) + \beta\Delta q, \tag{6.21}$$

Formula (6.21) is achieved by assuming the same velocity for the entire length of tendon.
Since we have $r_1\dot{q}$ and $r_2\dot{\theta}$ as the velocity of input and output sides of our the model, we
consider an average of this two as the velocity of the tendon, *i.e.*, $v = \frac{1}{2}(r_1\dot{q} + r_2\dot{\theta})$.

As a preliminary validation, the model was experimentally evaluated by applying a multi-
sinusoidal command signal using the Schroeder-phased method[2]. Five different multi-sine
signals were used to identify and validate the model, as detailed in Table 6.2. The frequency
range in each experiment were chosen so as to cover medium-to-high (I,II), low-to-medium
(III,IV), and low (V) frequency range. The same identification methodology was used to
identify the model parameters given in (6.21), where the signal I was used to identify the
parameters and signals II to V were used as validation inputs. The results are listed in
Table 6.2 for the right and left jaws, and the simulated results are depicted in Figure 6.10
for the right jaw in comparison with the rigid kinematic model. Figure 6.11 also shows the
Box-Whisker plot of error, in which the range of error is shown along with the median and
25th and 75th percentiles. The outliers are marked based on the 99.3% coverage of the error
values for each experiment. As observed, the estimation results were improved between
35.3 to 73.3 per cent in terms of the RMSE by using the proposed model in comparison
with the kinematic model. The improvement becomes more significant for the validation
signals containing higher frequency components, where the dynamic effect is dominant.

---

[2]$q(t) = \sum_{k=1}^{N} A_m\,cos(\omega_k t + \phi_k)$, where $\phi_k$ is chosen to minimize the crest factor [22], $\phi_k = \phi_1 - \frac{-k\pi(k-1)}{N}$.
In our experiment, $\phi_1 = \pi/2$.
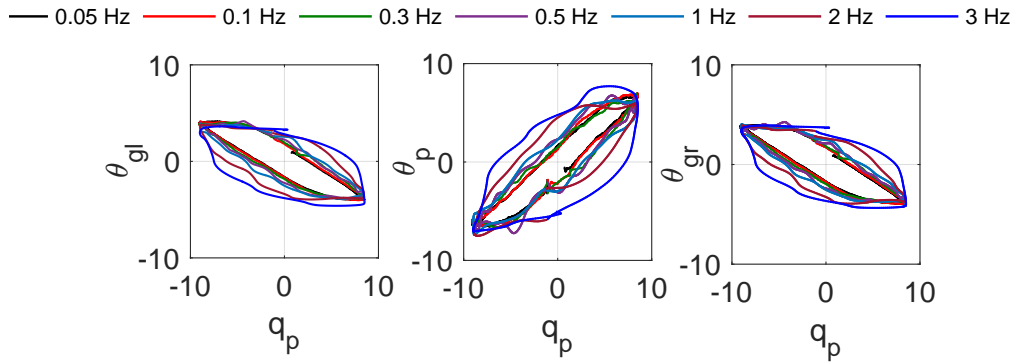
Figure 6.9: System hysteretic response to a swept-sine signal with constant amplitude of 10 deg and varying frequencies from 0.05 Hz to 3 Hz.

Table 6.2: Identification results of the dynamic model

| Exp. | Freq. Set [Hz] | Joint | PM RMSEs [deg] | KM RMSEs [deg] | PM GoF [%] | KM GoF [%] |
|------|----------------|-------|----------------|----------------|------------|------------|
| I | 0.2, 0.5, 0.8, 1.1, 1.4, 1.7, 2, 2.3 | Right | 1.1175 | 4.0539 | 88.8 | 59.4 |
| | | Left | 1.7892 | 3.6706 | 79.6 | 58.1 |
| II | 0.4, 0.7, 1.0, 1.3, 1.6, 1.9, 2.2 | Right | 1.083 | 4.060 | 88.4 | 56.5 |
| | | Left | 1.3599 | 3.9115 | 86.8 | 62.0 |
| III | 0.05, 0.1, 1.0 | Right | 1.2733 | 3.1377 | 88.7 | 72.1 |
| | | Left | 1.3295 | 2.5800 | 87.6 | 76.0 |
| IV | 0.05, 0.25, 0.45, 0.65 | Right | 1.5760 | 2.7831 | 77.6 | 60.5 |
| | | Left | 1.3704 | 2.1206 | 79.4 | 68.2 |
| V | 0.05, 0.07, 0.09 | Right | 0.8222 | 2.012 | 92.2 | 80.9 |
| | | Left | 0.6593 | 1.6037 | 93.9 | 85.2 |

*PM and KM refer to as the proposed model and kinematic model, respectively.

## 6.6 Conclusion

In this study, a new motion transmission model was introduced for multi-DOF tendon-driven mechanisms. The model included both the conventional rigid coupling effect and the hysteresis within the coupling. The model was adopted for a three-DOF surgical instrument to estimate the output rotational displacements of the joints using only the motor encoder and motor torque measurements. A preliminary model was also derived to describe the dynamics of the transmission. Both the quasi-static model and dynamic model were validated through extensive experiments. It was demonstrated that the proposed model improves the
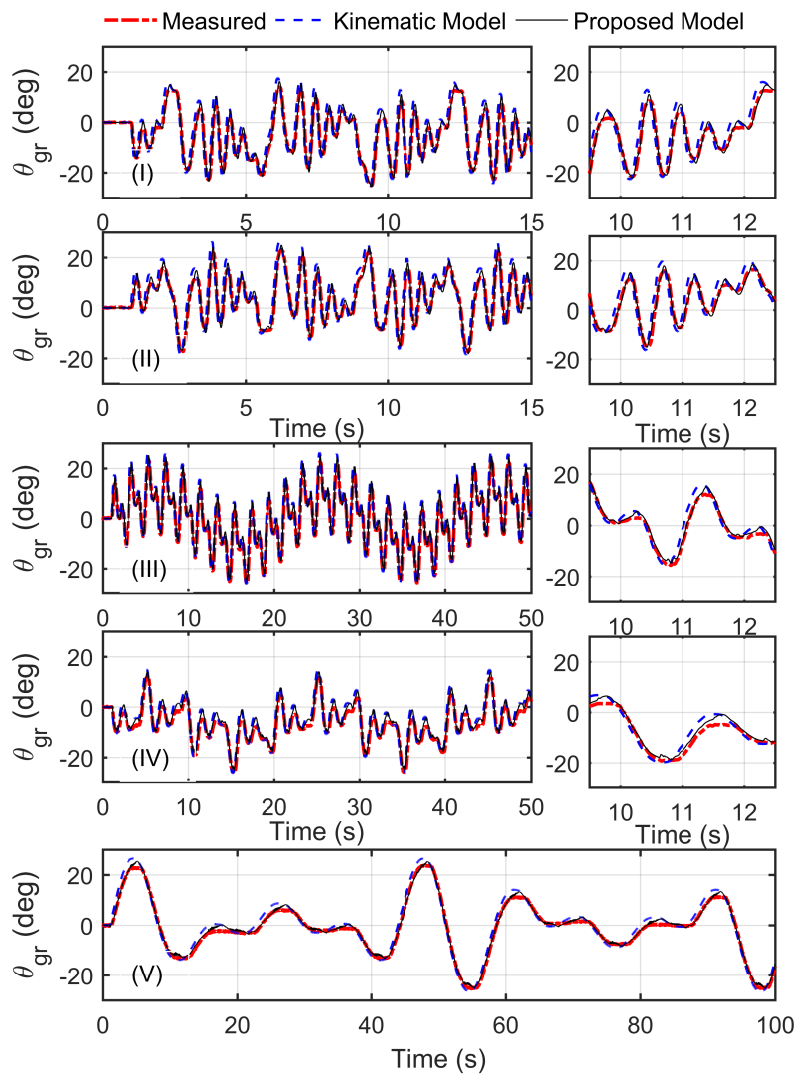
Figure 6.10: Dynamic identification results for the right jaw for multi-sine signals including (I) the training signal and (II)-(V) validation signals. The multi-sine parameters are given in Table 6.2.

(a) Right grasp



(b) Left grasp
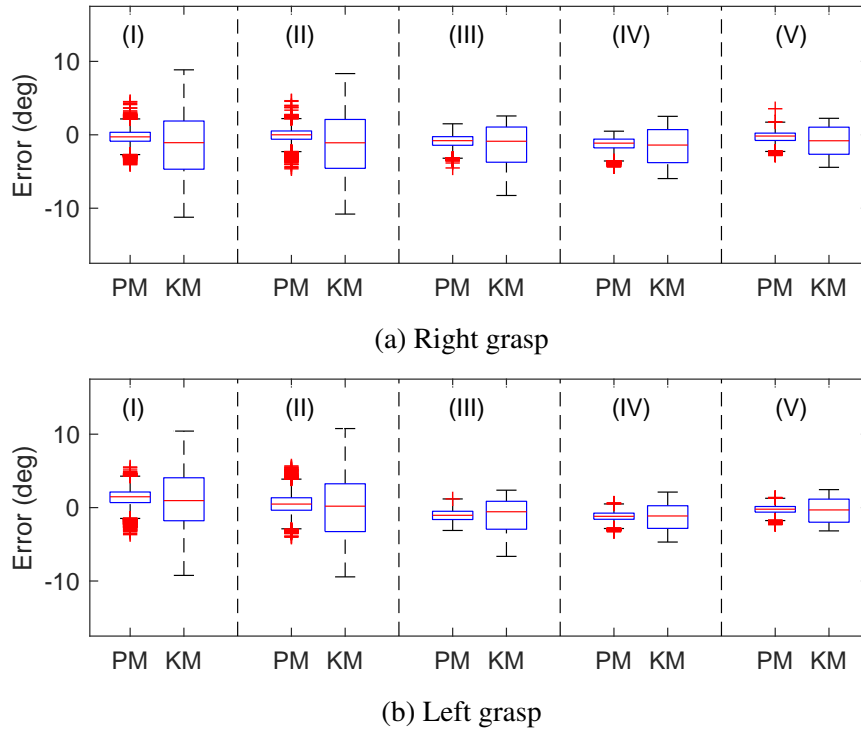
Figure 6.11: Dynamic identification results for multi-sine signals including (I) the training signal and (II)-(V) validation signals. The multi-sine parameters are given in Table 6.2. PM and KM refer to as the proposed model and the kinematics-based estimation, respectively.

accuracy of the position estimates by 35.3 to 73.3 per cent. Future work includes further experimental validation using multi-DOF surgical robotic systems as well as incorporating inertia and other dynamical terms in the dynamic model. Additionally, further results related to the use of the proposed modeling approach for hybrid force-position control will be obtained as part of our ongoing research.

# References

[1] M. Haghighipanah, Y. Li, M. Miyasaka, and B. Hannaford, "Improving position precision of a servo-controlled elastic cable driven surgical robot using unscented Kalman filter," in *International Conference on Intelligent Robots and Systems (IROS)*, pp. 2030–2036, IEEE, 2015.

[2] V. Hayward and J. M. Cruz-Hernández, "Parameter sensitivity analysis for design and control of tendon transmissions," in *Experimental Robotics IV*, pp. 239–252, Springer, 1997.

[3] G. Prisco and M. Bergamasco, "Dynamic modelling of a class of tendon driven manipulators," in *International Conference on Advanced Robotics (ICAR)*, pp. 893–899, IEEE, 1997.

[4] H. Kobayashi, K. Hyodo, and D. Ogane, "On tendon-driven robotic mechanisms with redundant tendons," *The International Journal of Robotics Research*, vol. 17, no. 5, pp. 561–571, 1998.

[5] R. M. Murray, Z. Li, and S. S. Sastry, *A mathematical introduction to robotic manipulation*. CRC press, 1994.

[6] E. Naerum, H. H. King, and B. Hannaford, "Robustness of the Unscented Kalman filter for state and parameter estimation in an elastic transmission," in *Proceedings of Robotics: Science and Systems*, (Seattle, USA), June 2009.

[7] M. Haghighipanah, M. Miyasaka, Y. Li, and B. Hannaford, "Unscented Kalman filter and 3D vision to improve cable driven surgical robot joint angle estimation," in *IEEE International Conference on Robotics and Automation (ICRA)*, pp. 4135–4142, IEEE, 2016.

[8] Y. Li, M. Miyasaka, M. Haghighipanah, and L. C. B. Hannaford, "Dynamic modeling of cable driven elongated surgical instruments for sensorless grip force estimation," in *2016 IEEE International Conference on Robotics and Automation (ICRA)*, pp. 4128–4134, IEEE, 2016.

[9] L. Kong and R. G. Parker, "Microslip friction in flat belt drives," *Proceedings of the Institution of Mechanical Engineers, Part C: Journal of Mechanical Engineering Science*, vol. 219, no. 10, pp. 1097–1106, 2005.

[10] D. Kim, "Dynamic modeling of belt drives using the elastic/perfectly-plastic friction law," Master's thesis, Georgia Institute of Technology, 2009.

[11] D. G. Alciatore and A. E. Traver, "Multipulley belt drive mechanics: creep theory vs shear theory," *Journal of Mechanical Design*, vol. 117, no. 4, pp. 506–511, 1995.

[12] S. E. Bechtel, S. Vohra, K. I. Jacob, and C. D. Carlson, "The stretching and slipping of belts and fibers on pulleys," *Journal of Applied Mechanics*, vol. 67, no. 1, pp. 197–206, 2000.

[13] J. Werkmeister and A. Slocum, "Theoretical and experimental determination of capstan drive stiffness," *Precision Engineering*, vol. 31, no. 1, pp. 55–67, 2007.

[14] O. Baser and E. I. Konukseven, "Theoretical and experimental determination of capstan drive slip error," *Mechanism and Machine Theory*, vol. 45, no. 6, pp. 815–827, 2010.

[15] F. Anooshahpour, I. G. Polushin, and R. V. Patel, "Quasi-static modeling of the da Vinci instrument," in *IEEE/RSJ International Conference on Intelligent Robots and Systems (IROS)*, pp. 1308–1313, IEEE, 2014.

[16] F. Anooshahpour, I. G. Polushin, and R. V. Patel, "Tissue compliance determination using da Vinci instrument," in *IEEE International Conference on Robotics and Automation (ICRA)*, pp. 5344–5349, IEEE, 2015.

[17] A. Talasaz, A. L. Trejos, S. P. H. Bassan, and R. V. Patel, "A dual-arm 7-degrees-of-freedom haptics-enabled teleoperation test bed for minimally invasive surgery," *ASME Journal of Medical Devices*, vol. 8, no. 4, p. 041004, 2014.

[18] Intuitive Surgical, Inc., *EndoWrist: Instrument and Accessory Catalog*, July 2011.

[19] Claron Technology Inc, *MicronTracker Developerś Manual,*.

[20] K. I. McKinnon, "Convergence of the Nelder-Mead simplex method to a nonstationary point," *SIAM Journal on Optimization*, vol. 9, no. 1, pp. 148–158, 1998.

[21] D. W. Marquardt, "An algorithm for least-squares estimation of nonlinear parameters," *Journal of the Society for Industrial and Applied Mathematics*, vol. 11, no. 2, pp. 431–441, 1963.

[22] P. Guillaume, J. Schoukens, R. Pintelon, and I. Kollar, "Crest-factor minimization using nonlinear Chebyshev approximation methods," *IEEE Transactions on Instrumentation and Measurement*, vol. 40, no. 6, pp. 982–989, 1991.

# Chapter 7

# The Application of Motion Transmission Model of Tendon-Pulley Transmission to Surgical Robots: A Preliminary Experimental Validation

**T**he tendon-pulley transmission modeling scheme was, previously, developed in Chapters 5 based on the concepts from the creep theory and extended in Chapter 6 to describe the coupled-hysteresis effect. This chapter focuses on the experimental validation of the model in tendon-driven robots. Motion transmission of the first three joints of the RAVEN II® surgical robot is analyzed, and backlash-like hysteresis within the transmission systems is modeled using the proposed scheme. The modeling accuracy is experimentally evaluated, showing more than 42% improvement in terms of RMSE, in comparison with the conventional friction/compliance-free models.

## 7.1 Introduction

In Robot Assisted Minimally Invasive Surgery (RAMIS), due to inherent size restrictions imposed on the surgical instruments, tendon-based mechanisms have become a common
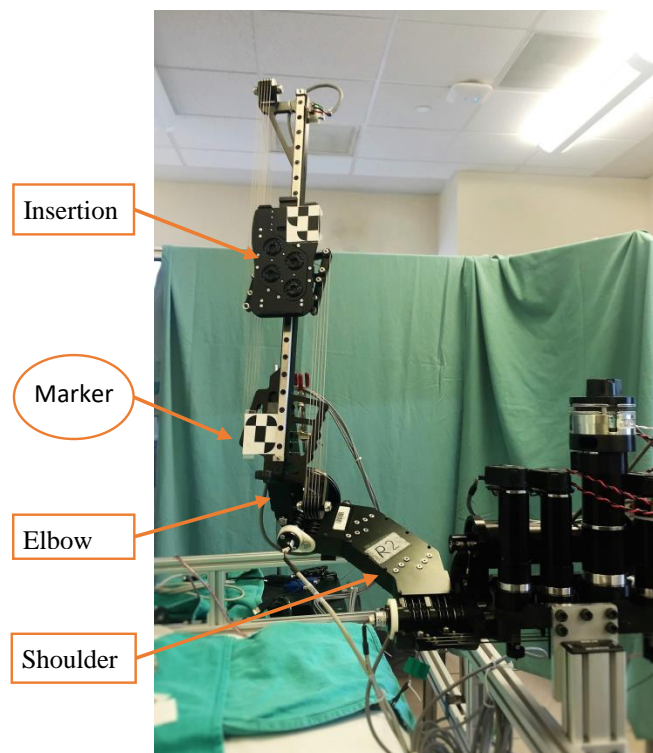
---

Figure 7.1: The right arm of the RAVEN II® surgical robotic system installed at CSTAR, London, ON, Canada

solution for power transmission. The da Vinci® Surgical System [1] and the RAVEN II® surgical robot [2] are the two most well-known tendon-based surgical platforms (Figure 7.1). Despite the human-in-the-loop nature of the current robotic surgical systems, there is a growing interest for supervised automation in execution of surgical tasks [3]. To this end, an accurate model of the force/motion transmission is required in order to compensate for nonlinearities within the transmission mechanism and/or to design high performance control algorithms[1].

In the literature, tendon-pulley drives were often treated as systems with rigid linkage leading to conventional linear kinematics [4] without considering the compliance of the tendons as well as tendon-pulley friction. In [5], a classical Preisach model was introduced to capture force transmission hysteresis in a tendon-pulley based RAMIS instrument. In [6], a formulation was suggested for robots with tendon-pulley and tendon-sheath power transmission based on tendon elongation; tendon-pulley friction, however, was not addressed. In [7], an unscented Kalman filter (UKF) algorithm was designed to estimate the motion transmission parameters of a one degree-of-freedom (DOF) tendon-pulley mechanism. The same algorithm was used in [8] for position control of three DOFs of the RAVEN II surgical system along with compensation for joint coupling effects. In both these studies, exponential springs along with *point-contact friction* were considered to model the nonlinearity of the system

Tendon-pulley mechanisms, particularly in the form of belt drives, have a long history of applications in the industrial systems for the purpose of power transmission. More than a century ago, Reynolds for the first time noticed that the friction on the pulleys surface results in tendon elongation and, consequently, slip on the pulley surfaces [9]. This phenomenon is known as elastic creep. The tendon creep theory, in particular, explains the formation of the slip and stick zones on the pulleys in a tendon-pulley power train, as shown in Figure 7.2(a). For a review on the theory, refer to [10] and [11]. A motion transmission model for tendon-pulley mechanisms was recently suggested by the authors based on tendon creep theory [13]. Unlike the above-mentioned studies, *distributed friction* was considered instead of point-contact friction to entail the true behavior of tendon-pulley interaction. This motion transmission model is dual to the force transmission models studied

---

[1]In non-RAMIS applications, the driven pulleys (*i.e.* robot's joints) can be sensorized, thus the nonlinearity due to transmission is compensated by the controller.
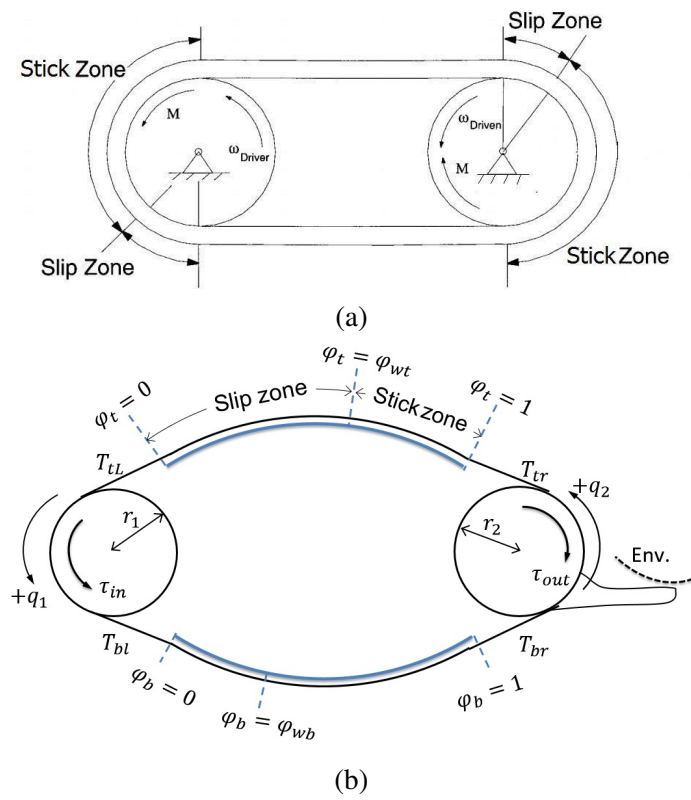
Figure 7.2: (a) Slip and stick zones on the input and output pulleys of a belt drive (adopted from [12]); (b) the tendon-surface interaction model of a one DOF tendon-pulley system.

in our earlier works [14, 15]. The model developed in [13] is of pseudo-kinematic type, where the output displacement is a function of both the input displacements and the input torque. The developed model is invertible, which allows for its use in real-time control applications.

An application of the proposed model to tendon-driven surgical robots is presented, where RAVEN II surgical robot is used as a test bed for experimental validation. The behavior of the first three joints of the robot is thoroughly analyzed along with the effect of pretension on the response of the system.

The chapter is organized as follows. In Section 7.2, a brief review of the proposed pseudo-kinematic motion transmission model is presented. In Section 7.3, the model is applied to describe the motion transmission characteristics of the first three DOFs of the RAVEN II surgical robot. Specifically, phenomenological analysis of the motion transmission behavior of the RAVEN II surgical robot is performed, the parameters of the motion transmission model are identified, and performance of the model is experimentally evaluated. Section 7.4 concludes the chapter.

## 7.2   Motion Transmission Model

The modeling approach used in this study accounts for tendon elastic creep in the system's pulleys. Specifically, the tendon elastic creep arises in the slip zone of the pulleys; the arc of the slip zone increases as the force applied to the tendon increases. In our modeling approach, in order to replicate the effect of multiple slip and stick zones in the tendon-pulley transmission (*i.e.* the idler pulley effect), two fixed curved surfaces are introduced along the tendon's forward and return paths, as illustrated in Figure 7.2(b). The slip and stick zones appear on the top and the bottom surfaces as a result of application of the input torque $\tau_{in}$. The geometric constraints imposed by the mechanism shown in Figure 7.2(b) require the elongation of the top tendon $\Delta_t$ to be related to the rotation of the input pulley $\Delta q_1$ and the output pulley $\Delta q_2$, as follows:

$$\Delta_t = \Delta q_1 r_1 - \Delta q_2 r_2, \tag{7.1}$$

where $r_1$ and $r_2$ are the radii of the input and the output pulleys, respectively. In the above equation, $\Delta q_2 \neq 0$ only if the wave of tension (or equivalently the slip zone) has reached the output pulley, otherwise $\Delta q_1$ does not affect $\Delta q_2$. Applying the same line of reasoning to the bottom tendon, equation (7.1) can be extended to a more general formula

$$\Delta q_2 = \begin{cases} \frac{r_1}{r_2}\Delta q_1 - \frac{1}{r_2}\Delta_t & \text{if } \varphi_{wt} = 1, \\ \frac{r_1}{r_2}\Delta q_1 + \frac{1}{r_2}\Delta_b & \text{if } \varphi_{wb} = 1, \\ 0 & \text{otherwise,} \end{cases} \tag{7.2}$$

where $\Delta_b$ is the elongation of the bottom tendon, and $\varphi_{wt} \in [0,1]$ and $\varphi_{wb} \in [0,1]$ are dimensionless parameters describing the length of the slip zones and subsequently the transition state of each tendon. Equation (7.2) will be referred as the pseudo-kinematic model hereafter in this chapter. Equation (7.2) also explains the hysteresis in the system. Specifically, the first and the second cases of (7.2) represent the ascending and the descending branches of the hysteresis loop, while the third case is the transition between the two.

The value of $\Delta q_2$ can in principle be found from (7.2), provided that the elongation variables $\Delta_t$ and $\Delta_b$ and the transition variables $\varphi_{wt}$ and $\varphi_{wb}$ are known. The pseudo-kinematic model can be simplified to become the following equation[2]:

$$\Delta q_2 = S(\dot{q}_1)\alpha_t \tau_{in} + (1 - S(\dot{q}_1))\alpha_b \tau_{in} + \beta \Delta q_1, \tag{7.3}$$

where $\alpha_t$, $\alpha_b$ and $\beta$ are constant parameters and $S(\dot{q}_1)$ is a switching function as defined below,

$$S(\dot{q}_1) := \begin{cases} 1 & \dot{q}_1 > 0, \\ 0 & \dot{q}_1 < 0. \end{cases} \tag{7.4}$$

In the derivation of (7.3), the following assumptions were considered:

- The transient response of the system is neglected, that is the tension propagates immediately, *i.e.* $\varphi_{wt} = \varphi_{wb} = 1$.

- The tension is zero in the loosened tendon, *i.e.*, the tension in the bottom tendon is zero if $\dot{q} > 0$, and the tension in the top tendon is zero if $\dot{q} < 0$.

---

[2]As shown in Chapter 5.

Equation (7.3) can be used to estimate $q_2$ for given $q_1$ and $\tau_{in}$. The first and the second terms in (7.3) describe the effect of tendon elongation on the motion transmission, while the third term represents the geometrical relationship between $q_1$ and $q_2$ similar to the kinematics of a rigid transmission.

**Remark 7.1.** *Equation* (7.3) *is only valid if the pretension is negligible. In a more general case where the pretension is constant and sufficiently large for both the top and the bottom tendons, it can be shown that* (7.3) *should be replaced with the following formula[3]:*

$$\Delta q_2 \approx S(\dot{q}_1)(\alpha_t \tau_{in} + \gamma_t \Lambda) \\ + (1 - S(\dot{q}_1))(\alpha_b \tau_{in} + \gamma_b \Lambda) + \beta \Delta q_1, \tag{7.5}$$

*where constant* $\Lambda \geq 0$ *is the sum of the area under the tension distribution of the top and the bottom tendons [14], and* $\gamma_t$, $\gamma_b \geq 0$ *are constant parameters. A more general pseudo-kinematic model for any arbitrary pretension in the tendons is given in Appendix A.*

## 7.3   Case Study: Experimental Results Using The RAVEN II Surgical Robot

This section first provides a phenomenological analysis of the motion transmission behavior in the first three links of the RAVEN II surgical robot (Figure 7.1). Next, the parameters of the proposed model described by (7.3) are identified. Finally, experimental validation of the model is presented. The RAVEN II surgical robot is a tendon-pulley driven surgical robotic system similar to its commercial counterpart, the da Vinci® robotic system. It was designed as an open platform to boost research on surgical robots, and to provide a testbed for preoperative and intra-operative data integration. The robot has seven DOFs: three DOFs for positioning of the remote center of motion and insertion, and four remaining DOFs to drive the instrument. All the DOFs are actuated by DC motors placed at the base. The servo layer of the RAVEN II control system is updated at 1 kHz frequency. The middle layer software environment is Robotics Operating System (ROS) which runs on

---

[3]According to the derivation given in Chapter 5, Appendix.

Figure 7.3: Shoulder DOF responses to sinusoidal inputs with fixed amplitude of $q_1 = 10$ degrees and frequencies of $0.1$, $0.2$ and $0.4$ Hz (left); hysteretic behavior of the shoulder DOF (right)

Linux. Further details can be found in [2].

In this study, the motion characteristics of the first three DOFs of the robot *i.e.*, the shoulder, the elbow, and the insertion, are investigated. In RAVEN II, only the angles of rotation of the motors are measured; in this study, however, additional 12-bit US digital MAE3-P12 absolute encoders were placed at the shoulder and the elbow joints for validation purposes. An Arduino Uno microprocessor was assigned to read the encoders and send the data to the main computer through ROS communication. For the insertion link, a 3D vision MicronTracker™ camera was used to measure the distance traveled by the sliding joint. The update rate of the camera was set to 30 Hz. The Root-Mean-Square (RMS) of the calibration error is 0.25mm for a single target point [16].
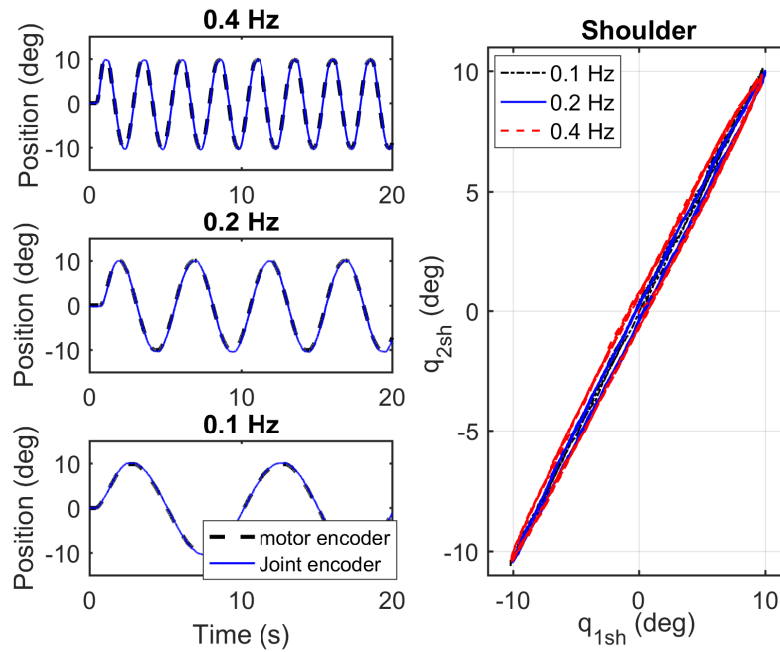
Figure 7.4: Elbow DOF responses to sinusoidal inputs with fixed amplitude of $q_1 = 10$ degrees and frequencies of $0.1$, $0.2$ and $0.4$ Hz (left); hysteretic behavior of the elbow DOF (right).

### 7.3.1 Motion Transmission Analysis

In this subsection, the motion transmission behavior of RAVEN II is experimentally investigated and analyzed. Figures 7.3 and 7.4 illustrate sample responses to $0.1$, $0.2$ and $0.4$ Hz sinusoidal commands with the amplitude of $10$ degrees sent to the shoulder and the elbow DOFs of the robot, respectively. Similarly, Figure 7.5 shows responses to sinusoidal commands with the same frequencies and amplitude of $25$ mm for the insertion DOF. As can be seen in Figure 7.4, significant backlash-like hysteresis is present in the response of the elbow DOF. The hysteretic behavior in the shoulder and the insertion DOFs, however, is negligible as compared to that of the elbow DOF, as shown in Figures 7.3 and 7.5. Both the shoulder and the insertion DOFs have large preset pretensions which resulted in a narrow backlash. The shoulder also is a capstan drive with a short tendon run forming a very stiff transmission as reported in [8]. In order to study the effect of pretension in the motion transmission, a sinusoidal input signal with frequency of $0.1$ Hz and peak-to-peak amplitude of $20$ degrees was commanded to the elbow DOF under different pretensions.
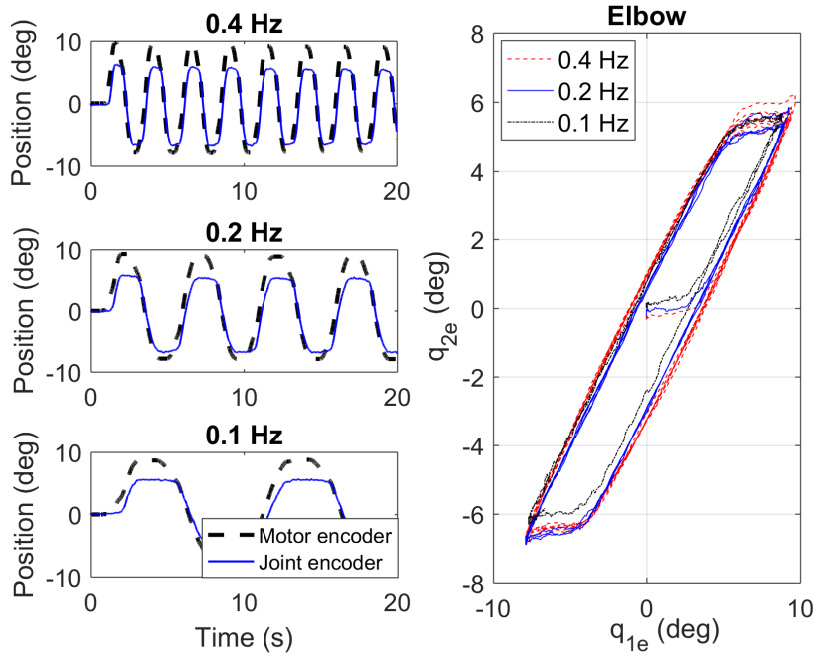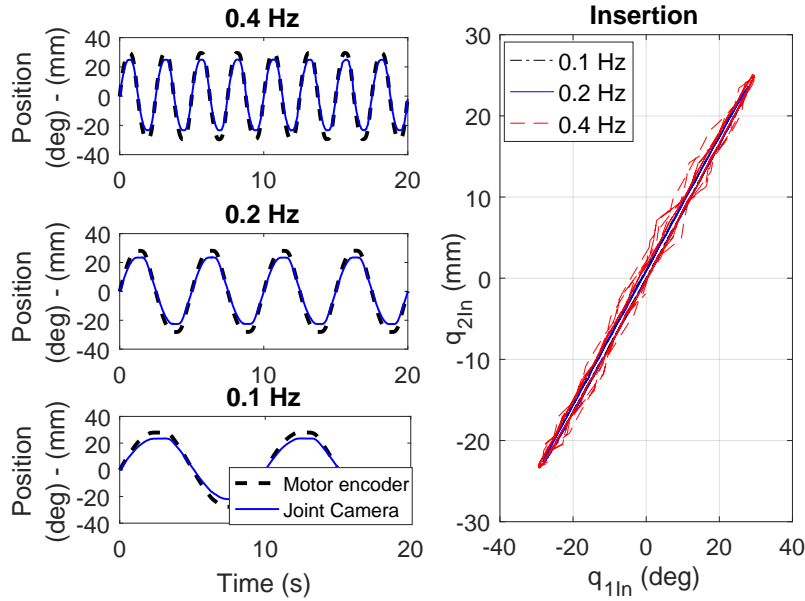
Figure 7.5: Insertion DOF responses to sinusoidal inputs with fixed amplitude of $q_1 = 25$ mm and frequencies of $0.1$, $0.2$ and $0.4$ Hz (left); hysteretic behavior of the insertion DOF(right).

Pretension in tendons can be altered through a set of tensioning screws in Raven. In this set of experiment, the tension was gradually adjusted from small to large pretension levels by tightening the screws. As shown in Figure 7.6, the width of the hysteresis loop becomes smaller as pretension increases. This is a direct consequence of the large pretension as discussed in Remark 7.1. This study is focused on the tendon-pulley transmission with low (close to zero) pretension which results in a significant backlash-like hysteresis as demonstrated above for the elbow DOF. Hysteresis, by definition, is the presence of a non-degenerate input-output closed curve as the frequency of the excitation signal approaches zero [17]. A common approach to validate the presence of hysteresis is to apply a series of sinusoidal signals with decreasing frequency. As the frequency approaches zero, the static behavior of the system dominates the dynamic response. In the presence of hysteresis, the input-output behavior converges to a fixed loop. This approach was applied to study the elbow response. To this end, a series of reference sinusoidal trajectories with frequencies starting from 1 Hz and decreasing to $0.1$ Hz with 10 degrees of amplitude was commanded to the elbow joint. Figure 7.8 shows the resulting input-output behavior. As observed, the behavior of the system converges to a fixed loop as the frequency of the command signal
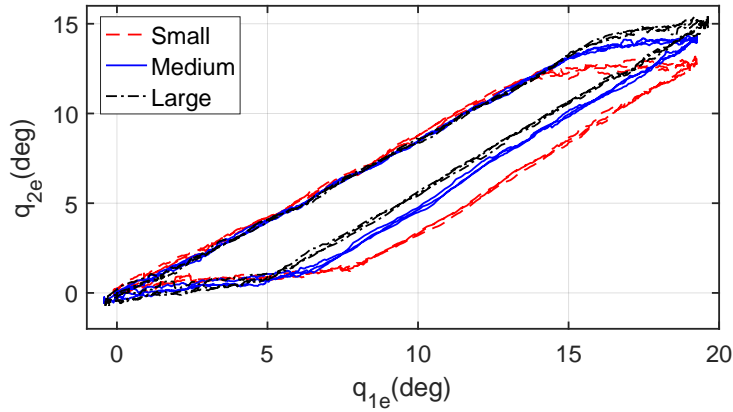
Figure 7.6: Elbow DOF responses to sinusoidal inputs with peak-to-peak amplitude of $20$ degrees and frequency of $0.1$ Hz, for different levels of pretension (small, medium, and large).
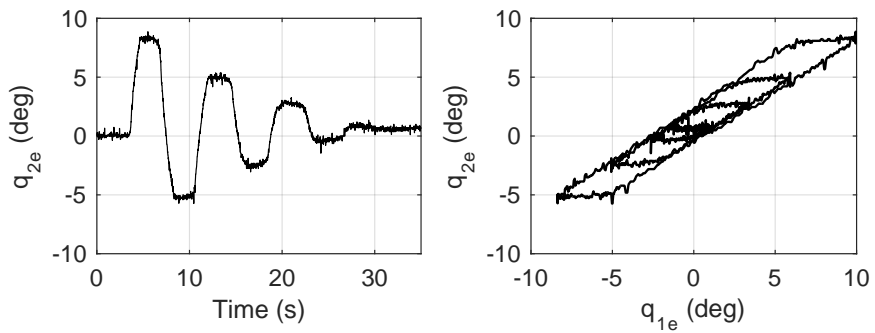


Figure 7.7: Response of the elbow DOF to an exponentially decaying command signal.
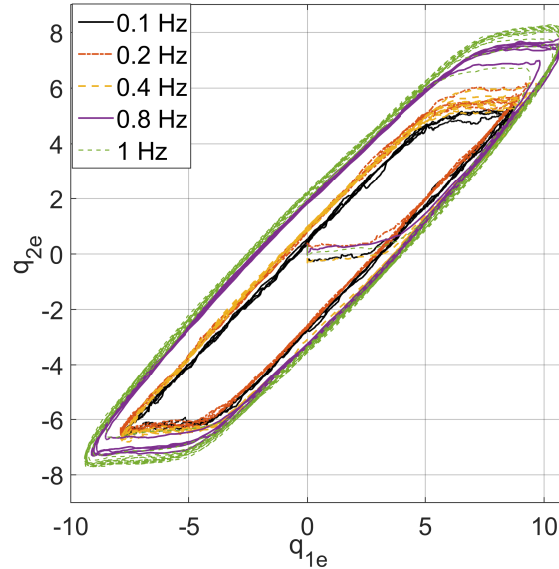
Figure 7.8: System response to sinusoidal inputs with fixed amplitude and various frequencies.

tends to zero, which validates the existence of hysteresis. Furthermore, an exponential decay command $q_{1ed} = 10e^{(-0.1t)} \sin(0.8t)$ was applied to elbow DOF with the purpose to study the minor loops. The result, which is illustrated in Figure 7.7, indicates the existence of a backlash-like hysteresis which is close to a pure backlash.

## 7.3.2 Model Identification

To identify the parameters of the proposed model (7.3) for elbow joint, a multi-sine Schroeder-phased command signal with frequencies of 0.05, 0.07, and 0.09 Hz was used[4]. Parameters $\alpha_t$, $\alpha_b$ and $\beta$ were adjusted to minimize the root mean square error (RMSE). The resulting parameters for the elbow DOF are given in Table 7.1. Due to the low frequency nature of the experiments, the dynamic effects were ignored and the gravity effect was compensated

---

[4]
$$q_1(t) = \sum_{k=1}^{N} A_m \, cos(\omega_k t + \phi_k)$$

where $N$ is the number of frequencies, $\omega_k$ is the k-th angular frequency, and $\phi_k$ is chosen to minimize the crest factor [18], *i.e.*, $\phi_k = \phi_1 - \frac{-k\pi(k-1)}{N}$.

Table 7.1: The identified values of model parameters

| $\alpha_t$ | $\alpha_b$ | $\beta$ |
|---|---|---|
| -5.302 | -1.002 | 0.839 |

Table 7.2: Identification results

| Exp. | Traj. type | Freq. Set [Hz] | PM RMSE [deg] | KM RMSE [deg] | PM GOF [%] | KM GOF [%] |
|---|---|---|---|---|---|---|
| I | Sine | 0.1 | 0.5073 | 1.2546 | 89.1 | 73.1 |
| II | Sine | 0.2 | 0.7749 | 1.5927 | 84.3 | 67.6 |
| III | Multi-Sine | 0.05, 0.07, 0.09 | 0.7830 | 1.4977 | 92.0 | 84.7 |
| IV | Multi-Sine | 0.05, 0.075, 0.1, 0.125, 0.15, 0.16 | 0.9106 | 1.5680 | 77.5 | 61.2 |
| V | Multi-Sine | 0.08, 0.1, 0.12, 0.14 | 0.6239 | 1.2557 | 88.0 | 75.9 |

*PM and KM refer to as the proposed model and kinematic model, respectively.

for in the torque signals. The optimal value of $\beta$ also closely matches the actual ratio of the pulleys and the motor gear ratio in the RAVEN II as reported in [8]; the transmission ratio was calculated to be $0.8098$ based on the gear ratio of the motor, and the motor shaft and the capstan radii[5].

To validate the model, four other commands including two sinusoidal and two multi-sine commands were applied. Figures 7.9 and 7.10 show the identification and validation results. Table 7.2 also lists the resulting error in terms of RMSE and goodness-of-fit (GOF). for the proposed model in comparison with those of the purely kinematics-based estimation (*i.e.* $\Delta q_2 = \beta \Delta q_1$); in fact, RMSE values of the proposed model show 42% to 60% decrease as compared to those of the kinematics-based model. It can be seen that the proposed model significantly improves estimation accuracy in comparison with that of the kinematics-based estimation.

Figure 7.11(a) shows the Box-Whisker plot of error, in which the range of error is shown along with the median and the 25th and 75th percentiles. The outliers are marked based on

---

[5]The gear ratio is 12.25, and motor shaft and joint capstan radii are 56.298 mm and 5.675 mm, respectively.

the 99.3% coverage of the error values for each experiment. As observed, implementation of the proposed model has significantly reduced the range of errors in comparison with that of the purely kinematics-based estimation. The probability distribution of the errors is shown in Figure 7.11(b). This figure indicates that, for the proposed model, the majority of the error values lie within $\pm 2.0°$, and are concentrated in the vicinity of zero, while the kinematics-based estimation resulted in higher probability of larger error values.

Finally, Figure 7.12 shows the resulting hysteresis model in comparison with the actual hysteresis between the motor rotation and the joint angle. As can be seen from the figure, the model closely follows the actual hysteretic behavior of the transmission system.

## 7.4 Conclusion

In this chapter, a recently proposed motion estimation model for tendon-pulley transmission mechanisms was evaluated for the RAVEN II surgical robot. The model was derived using tendon elastic creep analysis, where the distributed friction along the tendons and the compliance/elongation of the tendons were taken into account. The results clearly demonstrated the effectiveness of the proposed model in reducing the estimation error in terms of RMSE by more than 42% as compared to the purely kinematics-based estimation. Future work will focus on reducing the robot positioning error by implementing the proposed model for all joints of the robot and by compensating for the dynamics of the robot. A more general pseudo-kinematic model will be developed by relaxing the two assumptions of zero tension in the loosened tendon and immediate tension propagation. Additionally, further results on the use of the proposed modeling approach in a hybrid force-position control scheme will be obtained as part of our ongoing research.
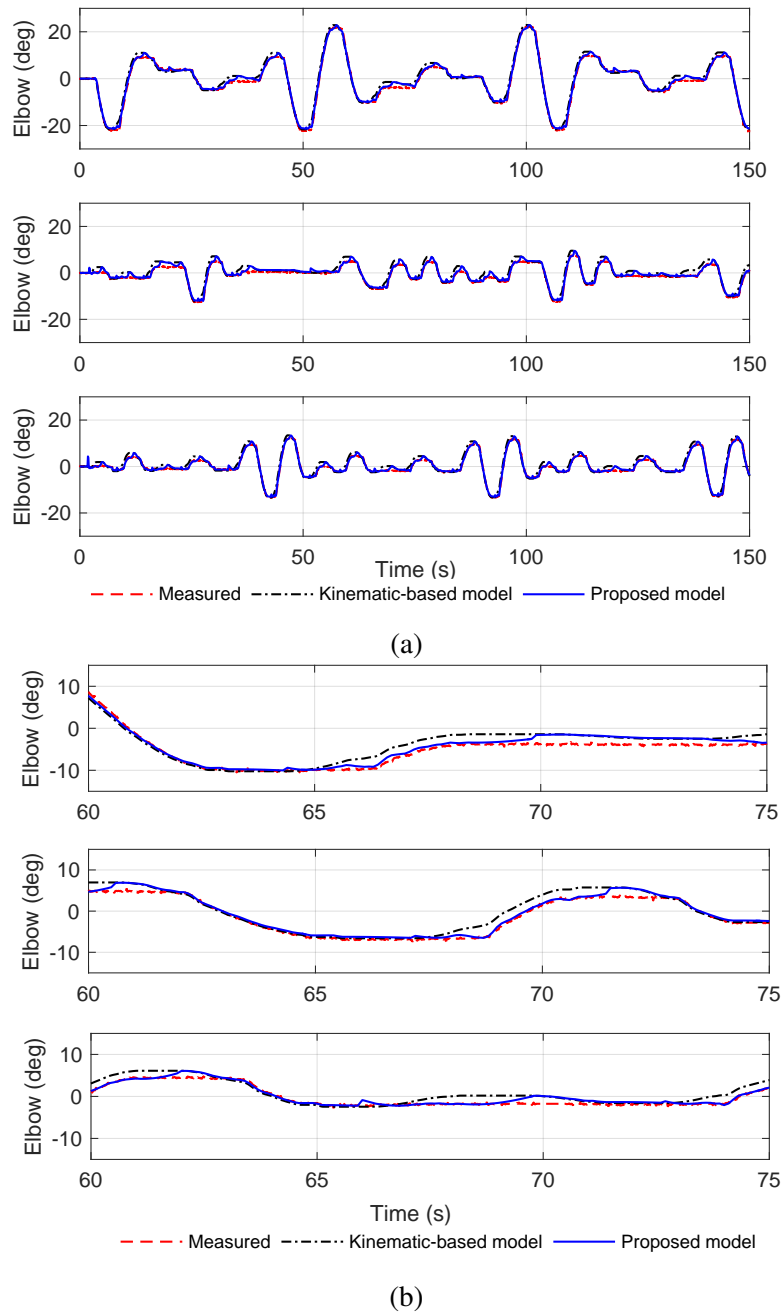
Figure 7.9: (a) The system's response to the multi-sine commands shown in Table 7.2 vs. the responses of the proposed model and the kinematics-based estimation; (b) scaled up version of the plots in part a).
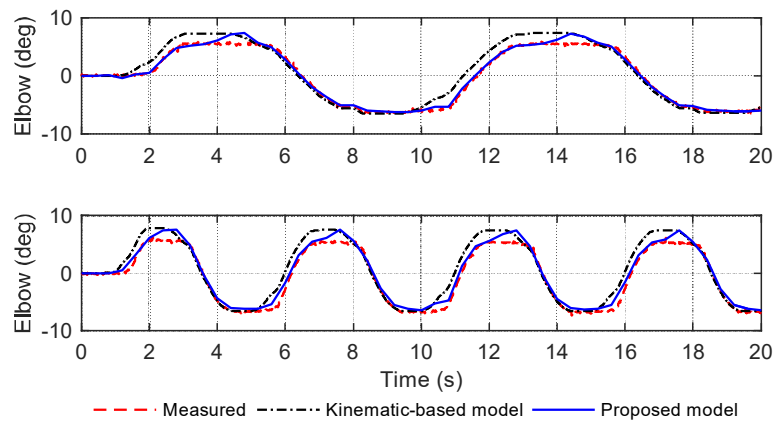
Figure 7.10: The proposed model estimation results for sinusoidal commands with frequencies of 0.1 and 0.2 Hz. The dash (red) line is the measured elbow position by joint encoder, the dash-dot (black) line is the response of the kinematics-based model, and the solid (blue) line is the response of the proposed model.
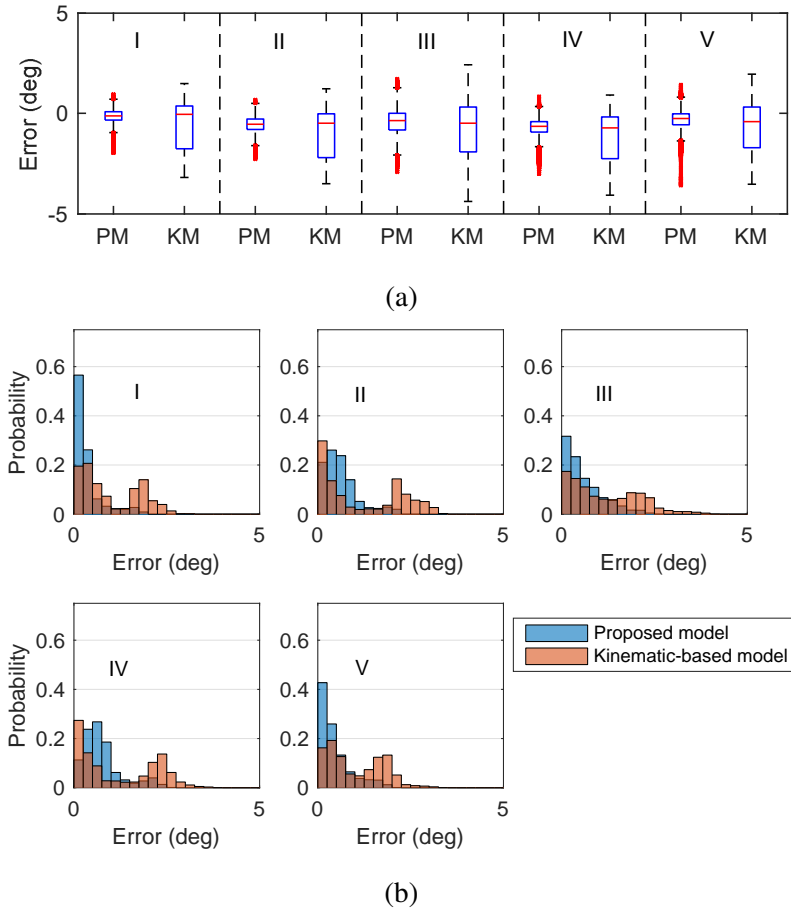
Figure 7.11: (a) Error distributions of the proposed model in comparison with those of the kinematics-based estimation for training and validation commands given in Table 7.2; (b) absolute error probabilities. PM and KM refer to as the proposed model and kinematics-based estimation, respectively.
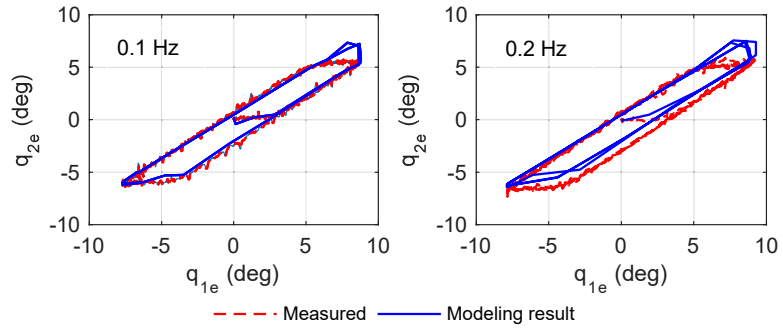


Figure 7.12: The hysteretic behavior of the proposed model vs. the actual hysteretic behavior of the elbow DOF, for sinusoidal commands with frequencies of 0.1 Hz (left plot) and 0.2 Hz (right plot).

# References

[1] G. Guthart and J. K. Salisbury, "The Intuitive™ telesurgery system: overview and application," in *IEEE International Conference on Robotics and Automation*, pp. 618–621, IEEE, 2000.

[2] B. Hannaford, J. Rosen, D. W. Friedman, H. King, P. Roan, L. Cheng, D. Glozman, J. Ma, S. N. Kosari, and L. White, "Raven-II: an open platform for surgical robotics research," *IEEE Transactions on Biomedical Engineering*, vol. 60, no. 4, pp. 954–959, 2013.

[3] S. Sen, A. Garg, D. Gealy, S. McKinley, Y. Jen, and K. Goldberg, "Automating multi-throw multilateral surgical suturing with a mechanical needle guide and sequential convex optimization," in *IEEE International Conference on Robotics and Automation(ICRA)*, 2016.

[4] A. Talasaz, A. L. Trejos, S. Perreault, H. Bassan, and R. V. Patel, "A dual-arm 7-degrees-of-freedom haptics-enabled teleoperation test bed for minimally invasive surgery," *ASME Journal of Medical Devices*, vol. 8, no. 4, pp. 041004–041004–15, 2014.

[5] F. Anooshahpour, I. G. Polushin, and R. V. Patel, "Classical preisach model of hysteretic behavior in a da Vinci instrument," in *IEEE International Conference on Advanced Intelligent Mechatronics (AIM)*, pp. 1392–1397, IEEE, 2016.

[6] R. M. Murray, Z. Li, and S. S. Sastry, *A mathematical introduction to robotic manipulation*. CRC press, 1994.

[7] E. Naerum, H. H. King, and B. Hannaford, "Robustness of the Unscented Kalman filter for state and parameter estimation in an elastic transmission," in *Proceedings of Robotics: Science and Systems*, (Seattle, USA), June 2009.

[8] M. Haghighipanah, Y. Li, M. Miyasaka, and B. Hannaford, "Improving position precision of a servo-controlled elastic cable driven surgical robot using unscented Kalman filter," in *International Conference on Intelligent Robots and Systems (IROS)*, pp. 2030–2036, IEEE, 2015.

[9] O. Reynolds, "On the efficiency of belts or straps as communicators of work," *Journal of the Franklin Institute*, vol. 99, no. 2, pp. 142–145, 1875.

[10] K. L. Johnson, *Contact Mechanics*. Cambridge University Press, 1987.

[11] D. G. Alciatore and A. E. Traver, "Multipulley belt drive mechanics: creep theory vs shear theory," *Journal of Mechanical Design*, vol. 117, no. 4, pp. 506–511, 1995.

[12] M. J. Leamy and T. M. Wasfy, "Analysis of belt-driven mechanics using a creep-rate-dependent friction law," *Journal of Applied Mechanics*, vol. 69, no. 6, pp. 763–771, 2002.

[13] F. Anooshahpour, P. Yadmellat, I. G. Polushin, and R. V. Patel, "A motion transmission model for tendon-based mechanisms with application to position tracking of the da Vinci instrument." Submitted to IEEE/ASME Transactions on Mechatronics, 2016.

[14] F. Anooshahpour, I. G. Polushin, and R. V. Patel, "Quasi-static modeling of the da Vinci instrument," in *IEEE/RSJ International Conference on Intelligent Robots and Systems (IROS)*, pp. 1308–1313, IEEE, 2014.

[15] F. Anooshahpour, I. G. Polushin, and R. V. Patel, "Tissue compliance determination using da Vinci instrument," in *IEEE International Conference on Robotics and Automation (ICRA)*, pp. 5344–5349, IEEE, 2015.

[16] Claron Technology Inc, *MicronTracker Developerś Manual*,.

[17] J. Oh, B. Drincic, and D. S. Bernstein, "Nonlinear feedback models of hysteresis," *IEEE Control Systems*, vol. 29, no. 1, pp. 100–119, 2009.

[18] P. Guillaume, J. Schoukens, R. Pintelon, and I. Kollar, "Crest-factor minimization using nonlinear Chebyshev approximation methods," *IEEE Transactions on Instrumentation and Measurement*, vol. 40, no. 6, pp. 982–989, 1991.

# Chapter 8

# Conclusion and Future Work

## 8.1 Conclusion

In this thesis, a novel approach for modeling transmission nonlinearities in tendon-pulley systems is developed. The approach is largely based on the idea of incorporating the distributed frictions between the tendon and the pulleys into the analysis.

First, it is shown that a close similarity can be observed between the hysteretic force transmission in tendon-pulley based da Vinci® instrument and that of tendon-sheath mechanisms. Consequently, a dual tendon-surface structure was suggested to represent the nonlinearities of the system. Tendon slip analysis was then used to develop a novel force estimation algorithm for tendon-pulley based laparoscopic instruments.

Second, as an application of the above modelling approach, a method for determination of the environmental stiffness by using only the instrument's actuation data is introduced. The feasibility of this method for determination of the compliance distribution in sample tissues when palpated by a sensorless tendon-driven instrument was experimentally demonstrated.

Third, in order to describe the hysteresis in force transmission behavior of tendon-pulley mechanisms, a phenomenological study was conducted on a da Vinci® instrument for the case where the tip was rigidly fixed in a force sensor. Having the two main properties of the congruency and wipe-out, it was shown that a classic Preisach hysteresis model could accurately replicate the force transmission behavior.

Forth, a comprehensive motion transmission analysis and a set of models is developed in this thesis for tendon-multipulley mechanisms. It was shown that the suggested dual tendon-surface structure could also be used to deriving a pseudo-kinematic model that can fully capture the backlash-like hysteresis of tendon-pulley mechanisms. The validity of the dual tendon-surface model was analytically proved by adopting the creep theory from belt mechanics to account for the idler pulleys. An application of the novel pseudo-kinematic model was successfully implemented and tested in a one-DOF motion tracking experiment. A general form of the pseudo-kinematic model of motion transmission was developed in this thesis to tackle the coupling effect in multi-DOF mechanisms. Consequently, the coupled-hysteresis effect which cannot be explained using conventional methods is described using the proposed approach.

Some preliminary studies were also conducted which form a foundation for future developments. These include analysis of the effect of pretension on the motion and force transmission; dynamic modelling of the motion transmission that describe the system's response to high-frequency inputs; and incorporating the transmission models into the robot dynamic equations.

## 8.2 Future Work

### 8.2.1 Hybrid Force/Motion Transmission

In this thesis, force transmission was modelled for the case of a fixed tip, and motion transmission was modelled assuming no interaction forces are present (*i.e.*, the case of a freely moving tip). The fixed tip and the freely moving tip represent two limiting cases which are somewhat similar to the open-circuit and short-circuit tests in electrical circuits. In particular, these two cases allowed us to determine the *nominal* behavior of the tendon-pulley transmission, which is not affected by the dynamics of the environment. When the tip is allowed to move while at the same time interacting with a soft environment, the dynamics of the environment would result in deviations from the nominal behavior of the mechanism. By analyzing such a deviation in real time, it will be possible to make the necessary adjustments to the force and motion estimates. The apparent stiffness of the

da Vinci® instrument studied in this thesis can be considered as the first step in studying such a deviation. Further studies of interactive motions will provide solid understanding of the hybrid force/motion transmission as is in a real surgery.

## 8.2.2 Advanced Theories for Tendon-Pulley Interaction

The classical creep theory, which results in one stick and one slip zones on each pulley, is not the only method for describing the interaction between the pulley and the tendon. Indeed, the creep theory is based on a simplified friction model, which assumes zero friction in the absence of relative motion; in particular, it completely ignores the pre-sliding friction. Consequently, the tension is considered unvarying in the stick zone (of a pulley or a surface), regardless of the loading conditions. A more accurate definition of friction forces would be helpful in deriving a better description of the tendon-pulley interaction. One solution could be an adaptation of the *shear theory* in contact mechanics to tendon-pulley problem, similarly to the approach taken in [1] where the shear theory is adopted for a dual-pulley belt-drive.

The other limitation of the creep theory and other similar theories from belt mechanics is that they assume steady-state working condition, *i.e.*, each pulley is assumed rotating with a constant speed. Although this assumption seems quite reasonable for belt drives in industrial applications, it is not always acceptable for tendon-pulley drives in robotics. In fact, the transmission in a surgical robot often demonstrates stop-and-go motion which also frequently switches between forward and backward rotations. In this thesis, such a transition is neglected for the sake of simplicity, however tendon-pulley transitional effect will be an important subject in future studies.

## 8.2.3 Mechanical Studies

This thesis, in general, took a phenomenological approach to modelling the tendon-pulley transmission in surgical robots. The observations were later explained using first physical principles. Although this approach is helpful and needed for robotic applications, a true understanding of the tendon-pulley transmission requires studying the mechanics of the

components. A comprehensive set of experiments for one- and two-pulleys configurations would greatly help in development of a more accurate understanding of multi-pulley transmissions in surgical robots. A simulation study which is easy to implement for such simple settings would also be very helpful for establishing the validity of new proposed models.

# References

[1] L. Kong and R. G. Parker, "Microslip friction in flat belt drives," *Proceedings of the Institution of Mechanical Engineers, Part C: Journal of Mechanical Engineering Science*, vol. 219, no. 10, pp. 1097–1106, 2005.

# Appendix A

# Relaxing The Zero-Pretension Assumption for the Pseudo-Kinematic Formula of Dual Tendon-Surface Systems

According to the development presented in Chapter 5, if an input torque $\tau_{in}$ is applied to a dual tendon-surface system shown in Figure A.1, the following formulas can be written for tension distributions and tendon elongations, respectively:

$$T_t(\varphi_t) = \begin{cases} T_{tl} \, e^{-\eta_t \varphi_t \, \mathrm{sgn}(\dot{q}_1)} & \varphi_i < \varphi_{wt}, \\ T_t^0(\varphi_t) & \varphi_t \geq \varphi_{wt}, \end{cases} \tag{A.1}$$

$$T_b(\varphi_b) = \begin{cases} T_{bl} \, e^{\eta_b \varphi_b \, \mathrm{sgn}(\dot{q}_1)} & \varphi_b < \varphi_{wb}, \\ T_b^0(\varphi_b) & \varphi_b \geq \varphi_{wb}, \end{cases} \tag{A.2}$$

$$\Delta_i = \frac{1}{K_{ni}} \int_0^1 (T_i(\varphi_i) - T_i^0(\varphi_i)) d\varphi_i, \tag{A.3}$$

where the subscript $i \in \{t, b\}$ denotes the top and bottom tendons in Figure A.1, and $T_{tl}$, $T_{bl}$, are the tensions in the left-end side of the top and bottom tendons, respectively. $\eta = \mu L/R$, $\varphi = x/L$, and $\varphi_w$ are a dimensionless friction parameter, the normalized position of a material particle along the length of the tendon, and the transition point, respectively. $T^0(\varphi)$ is the tension distribution from previous loadings prior to the application of $\tau_{in}$.
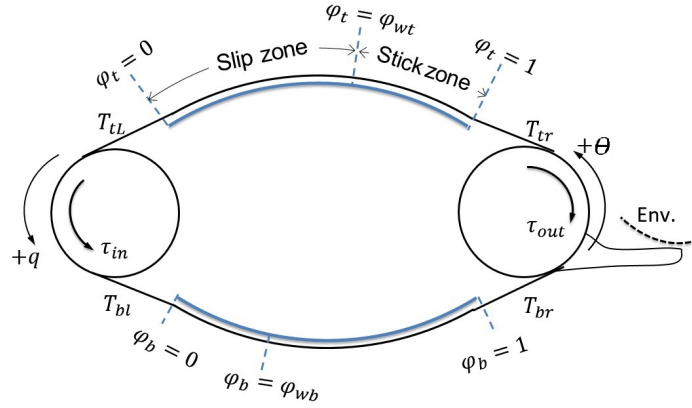
Figure A.1: The tendon-surface based model to represent a one-DOF tendon-multipulley system.

Furthermore, the following two equations are held for the input and the output pulleys, respectively:

$$\begin{aligned} \tau_{in} &= (T_{tl} - T_{bl})r_1, \\ \tau_{out} &= (T_{tr} - T_{br})r_2, \end{aligned} \tag{A.4}$$

Assuming

- (a) tension propagates immediately, *i.e.* $\varphi_t = \varphi_b = 1$ at all times, and

- (b) pretension is large enough such that tendons never go slack,

The tension and pretension can be uniquely defined. That is, if the change of direction of rotation of the input pulley has happened at time $t = t_0$, the current distributions (for $t > t_0$) are

$$\begin{cases} T_t = T_{tl} \, e^{- \operatorname{sgn}(\dot{q}_1)\eta_t \varphi_t}, \\ T_b = T_{bl} \, e^{\operatorname{sgn}(\dot{q}_1)\eta_b \varphi_b}, \end{cases} \tag{A.5}$$

Similarly, One can find the following tension distributions for $T_t^0(\varphi_t)$ and $T_b^0(\varphi_b)$, at $t = t_0^-$ which is the last instance before the change in direction happens,

$$\begin{cases} T_t^0(\varphi_t) = T_{tl}^0 \, e^{\operatorname{sgn}(\dot{q}_1)\eta_t \varphi_t}, \\ T_b^0(\varphi_b) = T_{bl}^0 \, e^{- \operatorname{sgn}(\dot{q}_1)\eta_b \varphi_b}. \end{cases} \tag{A.6}$$

where from (A.4), $T_t^0$ and $T_b^0$ are related to $\tau_{in}^0$,

$$\tau_{in}^0 = (T_{tl}^0 - T_{bl}^0)r_1. \tag{A.7}$$

Also, from the geometric constraint introduced in Chapter 5, the general from of the Pseudo-kinematic formula is defined as

$$\Delta q_2 = \begin{cases} \frac{r_1}{r_2}\Delta q_1 - \frac{1}{r_2}\Delta_t & \text{if } \varphi_{wt} = 1, \\ \frac{r_1}{r_2}\Delta q_1 + \frac{1}{r_2}\Delta_b & \text{if } \varphi_{wb} = 1, \\ 0 & \text{otherwise,} \end{cases} \tag{A.8}$$

From the first and second case of (A.8) we have the following constraint on the elongation in the top and bottom tendon (the compatibility condition),

$$\Delta_t + \Delta_b = 0, \tag{A.9}$$

which implies the amount of elongation in one side is equal to the amount of the shrinkage of the other. From (A.3), equation (A.9) can be solved to the following formula,

$$\frac{1}{K_{nt}} \int_0^1 (T_t d\varphi_t - T_t^0 d\varphi_t) + \frac{1}{K_{nb}} \int_0^1 (T_b d\varphi_b - T_b^0 d\varphi_b) = 0, \tag{A.10}$$

or,

$$\int_0^1 \frac{T_t(\varphi_t)}{K_{nt}} d\varphi_t + \int_0^1 \frac{T_b(\varphi_b)}{K_{nb}} d\varphi_b = \int_0^1 \frac{T_t^0(\varphi_t)}{K_{nt}} d\varphi_t + \int_0^1 \frac{T_b^0(\varphi_b)}{K_{nb}} d\varphi_b = \Lambda. \tag{A.11}$$

where $\Lambda$ is a constant. Equation (A.11) implies that a weighted sum of the areas under the tension distribution of the top and the bottom tendons always remains unchanged regardless of loading conditions. That can be interpreted as the contribution of the initial pretension set by the manufacturer.

Taking into account (A.5) and (A.6), one can solve equation (A.11) to obtain the following formula,

$$aT_{tl} + bT_{bl} = cT_{tl}^0 + dT_{bl}^0 = \Lambda, \tag{A.12}$$

where

$$a = \frac{\mathrm{sgn}(\dot{q}_1)}{-\eta_t K_{nt}}(e^{-\eta_t \, \mathrm{sgn}(\dot{q}_1)} - 1),$$

$$b = \frac{\mathrm{sgn}(\dot{q}_1)}{\eta_b K_{nb}}(e^{\eta_b \, \mathrm{sgn}(\dot{q}_1)} - 1),$$

$$c = \frac{\mathrm{sgn}(\dot{q}_1)}{\eta_t K_{nt}}(e^{\eta_t \, \mathrm{sgn}(\dot{q}_1)} - 1),$$

$$d = \frac{\mathrm{sgn}(\dot{q}_1)}{-\eta_b K_{nb}}(e^{-\eta_b \, \mathrm{sgn}(\dot{q}_1)} - 1).$$

Considering (A.12) and (A.4) we have:

$$T_{tl} = \frac{r_1 \Lambda + b\tau_{in}}{r_1(a+b)}, \quad T_{bl} = \frac{r_1 \Lambda - a\tau_{in}}{r_1(a+b)}, \tag{A.13}$$

and considering (A.12) and (A.7) we have

$$T_{tl}^0 = \frac{r_1 \Lambda + d\tau_{in}^0}{r_1(c+d)}, \quad T_{bl}^0 = \frac{r_1 \Lambda - c\tau_{in}^0}{r_1(c+d)}. \tag{A.14}$$

Therefore, $\Delta_t$ can be found as follows,

$$\Delta_t = \left(\frac{a}{a+b} - \frac{c}{c+d}\right)\Lambda + \frac{ab}{r_1(a+b)}\tau_{in} - \frac{cd}{r_1(c+d)}\tau_{in}^0. \tag{A.15}$$

Equation (A.15) can be substituted in (A.8) to find the pseudo-kinematic formula for motion transmission:

$$\Delta q_2 = \beta \Delta q_1 + \alpha(\mathrm{sgn}(\dot{q}_1))\tau_{in} + \alpha'(\mathrm{sgn}(\dot{q}_1))\tau_{in}^0 + \gamma(\mathrm{sgn}(\dot{q}_1))\Lambda. \tag{A.16}$$

where $\beta$ is a constant and $\alpha$, $\alpha'$ and $\Lambda$ each equals to two different constants based the direction of oration of the input pulley. The corresponding value of these parameters can in principal be calculated from (A.15) and (A.8).

In formula (A.15), if pretension is zero (i.e. from (A.12) we have $\Lambda = 0$ and from (A.4) we have $\tau_{in} = 0$), the elongation of the top tendon would be $\Delta_t \approx \alpha \tau_{in}$, which corresponds to the pseudo-kinematic equation given in Chapter 5 and 6.

IEEE
Requesting permission to reuse content from an IEEE publication

| | |
|---|---|
| **Title:** | Modeling of tendon-pulley transmission systems with application to surgical robots: A preliminary experimental validation |
| **Conference Proceedings:** | Advanced Intelligent Mechatronics (AIM), 2017 IEEE International Conference on |
| **Author:** | Farshad Anooshahpour |
| **Publisher:** | IEEE |
| **Date:** | July 2017 |

Copyright © 2017, IEEE

Logged in as:
Farshad Anooshahpour
Western University

LOGOUT

## Thesis / Dissertation Reuse

**The IEEE does not require individuals working on a thesis to obtain a formal reuse license, however, you may print out this statement to be used as a permission grant:**

*Requirements to be followed when using any portion (e.g., figure, graph, table, or textual material) of an IEEE copyrighted paper in a thesis:*

1) In the case of textual material (e.g., using short quotes or referring to the work within these papers) users must give full credit to the original source (author, paper, publication) followed by the IEEE copyright line © 2011 IEEE.
2) In the case of illustrations or tabular material, we require that the copyright line © [Year of original publication] IEEE appear prominently with each reprinted figure and/or table.
3) If a substantial portion of the original paper is to be used, and if you are not the senior author, also obtain the senior author's approval.

*Requirements to be followed when using an entire IEEE copyrighted paper in a thesis:*

1) The following IEEE copyright/ credit notice should be placed prominently in the references: © [year of original publication] IEEE. Reprinted, with permission, from [author names, paper title, IEEE publication title, and month/year of publication]
2) Only the accepted version of an IEEE copyrighted paper can be used when posting the paper or your thesis on-line.
3) In placing the thesis on the author's university website, please display the following message in a prominent place on the website: In reference to IEEE copyrighted material which is used with permission in this thesis, the IEEE does not endorse any of [university/educational entity's name goes here]'s products or services. Internal or personal use of this material is permitted. If interested in reprinting/republishing IEEE copyrighted material for advertising or promotional purposes or for creating new collective works for resale or redistribution, please go to http://www.ieee.org/publications_standards/publications/rights/rights_link.html to learn how to obtain a License from RightsLink.

If applicable, University Microfilms and/or ProQuest Library, or the Archives of Canada may supply single copies of the dissertation.

BACK | CLOSE WINDOW

# Curriculum Vitae

**Name:**  Farshad Anooshahpour

**Education:**

Ph.D.  The University of Western Ontario,
Electrical Engineering, Robotics and Control,
London, Canada. 2011–2017,
Thesis: *Modeling of Force and Motion Transmission in Tendon-Driven Surgical Robots.*

M.Sc.  K. N. Toosi University of Technology,
Mechatronic Engineering,
Tehran, Iran. 2006–2009,
Thesis: *Design and Implementation of a Motion Cueing Algorithm for ASARun Three-Degree-of-Freedom Driving Simulator.*

B.Sc.  K. N. Toosi University of Technology,
Mechancial Engineering, Mechanics, Dynamics and Design,
Tehran, Iran. 2000–2005,
Thesis: *Dynamic Simulation of a Virtual Hang-Glider in Planar Motion.*

**Recent Publications:**

- *F. Anooshahpour*, P. Yadmellat, I. G. Polushin, R. V. Patel, "A Motion Transmission Model for a Class of Tendon-Based Mechanisms with Application to Position Tracking of the da Vinci® Instrument," IEEE Transaction of Mechatronics, (accepted subject to minor revisions).

- *F. Anooshahpour*, P. Yadmellat, I. Polushin, R. V. Patel, "A Motion Transmission Model for Multi-DOF Tendon-Driven Mechanisms with Hysteresis and Coupling: Application to a da Vinci Instrument," IEEE/RSJ International Conference on Intelligent Robots and Systems, Vancouver, BC, 2017.

- *F. Anooshahpour*, P. Yadmellat, I. G. Polushin, R. V. Patel, "Modeling of Tendon-Pulley Transmission Systems with Application to Surgical Robots: A Preliminary Experimental Validation," in IEEE International Conference on Advanced Intelligent Mechatronics (AIM), Munich, Germany, IEEE, pp. 761-766, 2017.

- *F. Anooshahpour*, I. Polushin, R. V. Patel, "Classical Preisach Model of Hysteretic Behavior in a da Vinci Instrument," in IEEE International Conference on Advanced Intelligent Mechatronics (AIM), Banff, AB, pp. 1392-1397, IEEE, 2016.

- *F. Anooshahpour*, I. Polushin, R. V. Patel, "Tissue Compliance Determination Using a da Vinci Instrument," in IEEE International Conference on Robotics and Automation (ICRA), Seattle, WA, pp. 5344-5349, IEEE, 2015.

- *F. Anooshahpour*, I. Polushin, R. V. Patel, "A Quasi-Static Modelling of the da Vinci Laparoscopic Instrument," in IEEE/RSJ International Conference on Intelligent Robots and Systems (IROS), Chicago, IL, pp. 1308-1313, IEEE, 2014.

- *F. Anooshahpour*, A. Nahvi, N. Mehrabi, A. H. Haghighi, R. Kazemi, S. Samiee, "Design and Implementation of a Modified Classical Washout Filter Algorithm for ASARun Driving Simulator," Vol. 1, pp. 1-7, ISME, 2010.

- N. Mehrabi, *F. Anooshahpour*, "Design and Implementation Of an Optimal Active Roll Control System with Real-time Identification of Vehicle Parameters in Semi-Virtual Environment Using a Driving Simulator," Tehran, Iran, ISME, 2010.

- *F. Anooshahpour*, A. Nahvi, S. Azadi, "The Strategy for Conceptual Design of Motion Platforms for Vehicle Simulators, Considering Dynamics of the Vehicle and Human Motion-Perception Factors", in Proceedings of the First National Conference on Flight Simulators, Tehran,Iran, 2009.